12-2015

Solar Modulation of the Cosmic Ray Intensity and the Measurement of the Cerenkov Reemission in NOvA's Liquid Scintillator

Philip James Mason
University of Tennessee - Knoxville, pmason3@vols.utk.edu

To the Graduate Council:

I am submitting herewith a dissertation written by Philip James Mason entitled "Solar Modulation of the Cosmic Ray Intensity and the Measurement of the Cerenkov Reemission in NOvA's Liquid Scintillator." I have examined the final electronic copy of this dissertation for form and content and recommend that it be accepted in partial fulfillment of the requirements for the degree of Doctor of Philosophy, with a major in Physics.

Tom Handler, Major Professor

We have read this dissertation and recommend its acceptance:

Yuri Kamyshkov, Yuri Efremenko, Larry Townsend

Accepted for the Council:
Carolyn R. Hodges

Vice Provost and Dean of the Graduate School

(Original signatures are on file with official student records.)

Solar Modulation of the Cosmic Ray Intensity and the Measurement of the Cerenkov Reemission in NOvA's Liquid Scintillator

A Dissertation Presented for the
Doctor of Philosophy
Degree
The University of Tennessee, Knoxville

Philip James Mason
December 2015

ACKNOWLEDGEMENTS

Thanks to Tom Handler for his guidance and supervision over the duration of this research, and to Yuri Kamyshkov for his assistance with various problems pertaining to the study of the liquid scintillator. This work would not have been possible without the resources at Fermilab or the efforts of the NOvA collaboration.

ABSTRACT

The NOνA (NuMI Off-axis electron neutrino Appearance) experiment is a long baseline neutrino oscillation experiment at Fermi National Accelerator Laboratory. Its purpose is to observe the oscillation of ν_μ (muon neutrino) to ν_e (electron neutrino) and to investigate the neutrino mass hierarchy and CP violation in the neutrino sector. Two detectors have been built for this purpose, a Near Detector 300 feet underground at Fermilab, and a Far Detector, on the surface at Ash River, Minnesota.

The completion of NOνA's Far Detector in October 2014 enabled not only the recent measurement of neutrino oscillations, but an array of other physics studies. Coronal mass ejections cause an observable effect on the cosmic ray intensity measured at and around Earth, through the enhancement of the interplanetary magnetic field. Studying this phenomenon generally entails the measurement of the change in intensity of secondary neutrons from air showers, but it is of equal interest to observe the effects on secondary muons. Presented here is the study of the intensity modulation as measured in cosmic muon data from NOνA's Far Detector in Ash River, MN. In addition, this thesis details the study of the non-linear energy response of NOνA's liquid scintillator through the measurement of Cerenkov reemission, providing a needed correction to NOνA's energy calibration.

TABLE OF CONTENTS

LIST OF TABLES

LIST OF FIGURES

CHAPTER 1. INTRODUCTION

Neutrinos are weakly interacting spin ½ particles with no charge and currently undetermined masses. They come in three flavors associated with their partner leptons: electron neutrino, muon neutrino, and tau neutrino. In addition, each flavor has an associated antineutrino. For decades neutrinos were thought to be massless particles. The Standard Model does not accommodate massive neutrinos. But evidence of neutrino flavor oscillations, first predicted by Bruno Pontecorvo, and observed in solar neutrinos, suggest at least two neutrino flavors must have nonzero mass. Flavor oscillation is a function of mass difference squared, and would not be possible without massive neutrinos. Neutrino oscillation is described by the Pontecorvo–Maki–Nakagawa–Sakata (PMNS) matrix, which is defined by four parameters: the three mixing angles θ_{13}, θ_{23}, θ_{12}, and a CP-violating phase δ. In addition to these parameters, the mass difference squared of the three neutrino mass eigenstates (ν_1, ν_2, ν_3) are required to calculate oscillation probabilities. Presently, measured values exist for all three mixing angles, but the CP-violating phase δ remains to be evaluated, as does the mass hierarchy. Values for the mass differences squared have also been measured, but exact mass measurements do not as of yet exist.

The NuMI Off-Axis νe Appearance (NOvA) experiment based at Fermilab is designed to measure this CP-violating phase, and to determine the mass hierarchy of the neutrino types; $m_1^2 < m_2^2 << m_3^2$ (normal hierarchy), or $m_3^2 << m_1^2 < m_2^2$ (inverted hierarchy). When it is finished, NOvA will consist of three detectors: the prototype Near Detector on the Surface (NDOS) at Fermilab, the underground Near Detector at Fermilab in the NuMI beamline, and the underground Far Detector at Ash River, Minnesota, also in the NuMI beamline.

NOvA's detectors are triggered not only on the NuMI beam, but on cosmic evemts, mostly cosmic ray muons and neutrinos, which contribute a background to the beam signal. But cosmic rays are an interesting realm of physics on their own, and NOvA's design allows for a large area of cosmic ray flux to be studied. This thesis details

the measurement of the Forbush decrease as observed by the NOvA detector, a phenomenon in which the intensity of cosmic rays suddenly decreases due to a coronal mass ejection from the Sun enveloping Earth, or at least partially covering Earth, and deflecting many of the cosmic rays that would normally enter the atmosphere and result in secondary particle showers that are observed in the NOvA detectors.

Accurate energy calibration is vital in all particle physics experiments to allow for the precise reconstruction of interactions within the detectors. NOvA has been calibrated in-situ with cosmic ray muons, but its liquid scintillator exhibits a characteristic nonlinear energy response that causes an excess in the estimation of electromagnetic shower energies. This is observed for high dE/dx, as seen in the tail of an electromagnetic shower. The two factors responsible for this nonlinear energy response are Birk's quenching and UV Cerenkov reemission. This thesis will detail the study of the latter contributor, the UV Cerenkov reemission, and how its effects on the scintillator's energy response were measured and integrated for NOvA's energy calibration.

In addition to the studies of the Forbush decrease and NOvA's scintillator's nonlinear energy response, the author's contributions in the NOvA experiment have included the preparation, construction, and repairing of the NDOS, the development and validation of software for offline physics analysis and reconstruction, the development of tools for monitoring environment variables in the detector's instruments, and creating Monte Carlo simulations for the Production group for offline software validation, plus other service work, including scintillator filling and numerous data taking shifts in the NOvA control rooms.

CHAPTER 2. NEUTRINO PHYSICS AND HISTORY

2.1 Neutrino History

In June of 1998 the Super-Kamiokande experiment in Japan reported evidence of neutrino oscillation in atmospheric neutrinos. Although neutrino oscillation evidence from solar neutrinos was already available, Super-Kamiokanda was the first experiment to show with high statistics that the deficit of expected neutrinos was dependent upon the neutrinos' path length and energy. This was the first sign that neutrino oscillation behaved as theorized. The implications of these findings were contrary to predictions of the Standard Model, which implied zero-mass neutrinos [1]. But the oscillation of flavor types is a phenomenon that is impossible without mass differences, as will be explained later. And differences in mass, of course, cannot exist in massless particles.

The neutrino was proposed by Wolfgang Pauli in 1930 to explain the results of Beta decay experiments. In 1914 James Chadwick had shown that, in beta decay, electrons were emitted in a continuous spectrum, from 0 eV to a maximum energy characteristic of the nuclide. The directions of the emitted electrons were almost never observed to be exactly opposite, a requirement for the conservation of linear momentum. Furthermore, the spins of all known particles involved in beta decay, the neutron, proton, and electron, are ½. As beta decay was understood, spin would not be conserved in the event of a neutron becoming a proton and an electron. Nor would angular momentum. Pauli proposed that a weakly interacting, spin-½, neutral-charged, light particle was responsible for the missing energy of Beta decay, and would also fix the problem of momentum and spin conservation. He suggested this particle's properties ruled out its ever being detected.

Energy conservation in Beta decay was handled by treating it as a three body decay, in which an antineutrino carried away the extra energy. Enrico Fermi developed his theory of the weak interaction in 1934 and was able to set a limit on the neutrino mass based on the idea that the neutrino's mass would affect the shape of the energy spectrum

seen in Beta decay. Hans Bethe and Rudolf Peierls were able to predict an extremely small cross section for the neutrino with matter, from which they asserted neutrinos were not observable.

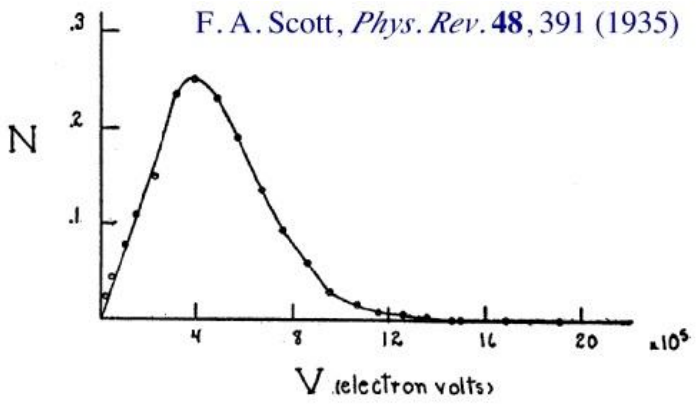

Figure 2.1 Beta decay energy spectrum [2].

The weakly interacting nature of the neutrino meant finding it would be difficult. Its cross section would be smaller than any known particle at the time. A large flux of neutrinos would be necessary if any observation was to be achieved. It wasn't until 1956 when Frederick Reines and Clyde Cowan made the first direct observation of (anti)neutrinos in inverse Beta decay (anti-$\nu_e + p^+ \rightarrow n_0 + e^+$) at the Savannah River nuclear reactor in South Carolina, with a flux of 5E13 neutrinos/s/cm^2 that the elusive neutrino was shown to exist [3]. This work would win Frederick Reines the 1995 Nobel Prize in physics.

The lack of observed decay mode $\mu \rightarrow e + \gamma$ suggested a conservation law for muon and electron type leptons. A second type of neutrino, the muon neutrino, was discovered in 1962 at Brookhaven National Laboratory's Alternating Gradient Synchrotron (AGS) facility by Leon Lederman, Melvin Schwartz, and Jack Steinberger [4]. The AGS fired protons at a beryllium target, which produced a shower of pi mesons that decayed into muons and neutrinos. Only the neutrinos would penetrate the 5,000 ton steel wall of the neon-filled spark chamber, where muon spark trails would be formed by

muon neutrinos and observed by the scientists. For this discovery the team won the 1988 Nobel Prize in physics.

After the discovery of the tau lepton in 1975 the tau neutrino was postulated to exist. The DONUT collaboration at Fermilab detected the first signs of the tau neutrino in 2000, the third flavor of neutrino predicted by the Standard Model. Its neutrino beam was created from 800 GeV protons from Fermilab's Tevatron interacting in a tungsten beam dump. The main source of tau neutrinos was the decay of D_s mesons into tau leptons and tau antineutrinos, and the decay of tau leptons into tau neutrinos. Only four out of 203 observed neutrino events were associated with tau neutrino tracks. But these events were in such excess of the background that there was only a 4E-4 probability these were part of the background [5].

Figure 2.2 Weak interactions of the neutrino. Charged current interaction (left) and neutral current interaction (right).

2.2 The Solar Neutrino Problem

Neutrinos observed on Earth have various sources, two of which are natural. Solar neutrinos are formed in fusion reactions in the sun, either in the proton-proton chain reaction (pp cycle) or the CNO cycle. The pp cycle is the dominant chain in the sun, as a process by which the sun converts hydrogen to helium.

The first stage of the pp cycle, the fusion of two hydrogen atoms into deuterium, releases a positron and an electron neutrino. In the second stage, deuteron and proton combine to make ^{3}He and a photon. During the third stage, the ^{3}He combine to make an

alpha particle and two protons, or a ^{3}He combines with a proton to make an alpha, a positron, and an electron neutrino. A third reaction in this stage is the creation of Berillium and a photon by the reaction of ^{3}He with an alpha particle.

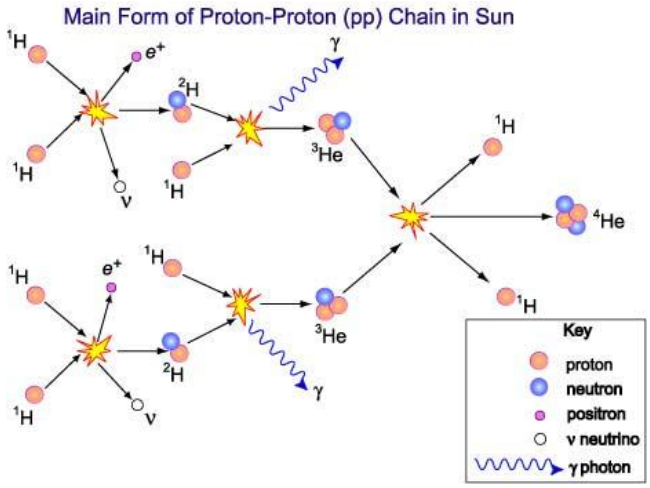

Figure 2.3 Proton-Proton Chain.

PP-chain:

$$p + p \rightarrow D + e^+ + \nu_e$$

$$p + p + e^- \rightarrow D + \nu_e$$

$$D + p \rightarrow {}^3He + \gamma$$

$${}^3He + p \rightarrow \alpha + e^+ + \nu_e$$

$${}^3He + {}^3He \rightarrow \alpha + p + p$$

$${}^3H + \alpha \rightarrow {}^7Be + \gamma$$

Berillium then creates alpha particles and additional neutrinos.

$${}^7Be + e^- \rightarrow {}^7Li + \nu_e$$

$${}^7Li + p \rightarrow \alpha + \alpha$$

$${}^7Be + p \rightarrow {}^8B + \gamma$$

$${}^8B \rightarrow {}^8Be + e^+ + \nu_e$$

$${}^8Be \rightarrow \alpha + \alpha$$

Five different reactions in the pp chain create neutrinos. There is a characteristic energy spectrum for each. The highest flux is from neutrinos created by the initial p + p reaction, accounting for about 60% of the expected flux, though they are also of the lowest energy.

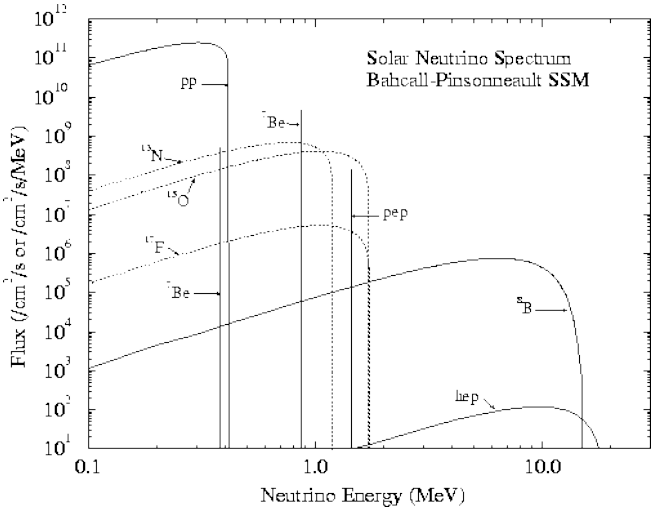

Figure 2.4 Expected energy spectra for solar neutrinos.

Measuring neutrinos from the sun was made possible by Ray Davis, who devised a detector at Homestake mine filled with 100,000 gallons of Chlorine. The experiment was held a mile underground to eliminate cosmic ray backgrounds, and detected neutrinos through the process $\nu_e \rightarrow {}^{37}Cl \rightarrow {}^{37}Ar + e^-$. The reaction has a threshold of 0.8 MeV, and was not sensitive to neutrinos from the initial pp reaction. Argon atoms were produced at a rate of about one every two days, and were collected over a period of several months. By 1968 only one third the predicted number of Argon atoms were found. The predicted number was based on the Standard Solar Model (SSM) of the interior of the sun, and experiments following Davis's confirmed the solar neutrino deficit [6].

This deficit in Davis's experiment was known as the solar neutrino problem, because the cause of the deficit was unknown. No models of the sun or of particle physics

at the time could provide an answer. One possibility was a flaw in either the SSM or the SM, leading to inaccurate predictions for the numbers of neutrinos expected from the sun. But the rationale against this was that flaws in these models would have manifested elsewhere, in the form of questionable results from other experiments. With no existing evidence to suggest a flawed SSM or SM, the only possibility was something unknown happening to the neutrinos on their way from the sun's core to Earth. The assumed zero mass of the neutrino turned out to be the flaw responsible for understanding these missing neutrinos. Bruno Pontecorvo proposed the idea of neutrino oscillation in 1957, the process by which one neutrino flavor transforms into another during flight. This phenomenon would require the neutrino to have mass, contrary to the common belief that the neutrino was a massless particle. Flavor oscillation would explain why detectors were seeing so few neutrinos when so many more were expected: They were seeing only one type of neutrino. In 1968 Pontecorvo suggested that Davis's experiment's shortage in neutrino detection was due to its insensitivity to the other neutrino types: muon and tau.

2.3 Neutrino Oscillations

Although the Kamiokande experiment in Japan measured a similar deficit of solar neutrinos in 1988, it wasn't until 1998 that the first strong evidence for neutrino oscillation was found in the Super-Kamiokande experiment [1]. The experiment was sensitive to muon, tau, and electron neutrinos, and used water in its 22.5 kton fiducial volume detector instead of Chlorine, as in Davis's experiment. The process by which Super-Kamiokande observed neutrinos was elastic neutrino-electron scattering: $\nu + e \rightarrow \nu + e$. The daughter electron was detected via Cerenkov radiation emitted in the water. In 2001, the collaboration's results were presented on the observation of atmospheric neutrinos produced by cosmic ray interactions in the atmosphere, $\pi^{\pm} \rightarrow \mu^{\pm} + \nu_{\mu}(\text{anti } \nu_{\mu})$, $\mu^{\pm} \rightarrow e^{\pm} + \text{anti } \nu_{\mu} (\nu_{\mu}) + \nu_{e}(\text{anti } \nu_{e})$. They found only 45% of the predicted number of neutrinos, showing the data to be consistent with neutrino oscillations. Currently the Super-Kamiokande has provided the best measurement for $\sin^2(2\theta_{23})$.

A solar neutrino experiment at the Sudbury Neutrino Observatory (SNO) in Canada, using 1000 tons of heavy water (D_2O), measured ^8B solar neutrinos through charged-current (CC) and neutral-current (NC) interactions [8]. The CC interaction, $\nu_e + D \rightarrow e + p + p$, is sensitive only to ν_e, while the NC interaction, $\nu_x + D \rightarrow \nu_x + p + n$, is sensitive to all neutrino types. SNO was also sensitive to electron scattering (ES) interactions involving the recoiling of an electron hit by a neutrino, an interaction largely dominated by electron neutrinos. If the solar neutrino problem was due to neutrino oscillation, a difference would be observed between the solar neutrino fluxes from CC and NC interactions. In 2001, SNO published their first results, finding 35% of the predicted flux. When compared to the data of Super-Kamiokande, noting its 6.5 times greater efficiency for electron-neutrinos, it appeared all the neutrinos could be accounted for if oscillation were a reality. Results published by SNO in 2002 confirmed their earlier findings, establishing a limit on θ_{12} at the time ($\theta_{12} \sim \pi/6$) and on Δm^2_{12}, (Δm^2_{12} = 7.59E-5 eV^2), the mixing angle and mass difference squared corresponding to the solar neutrino sector.

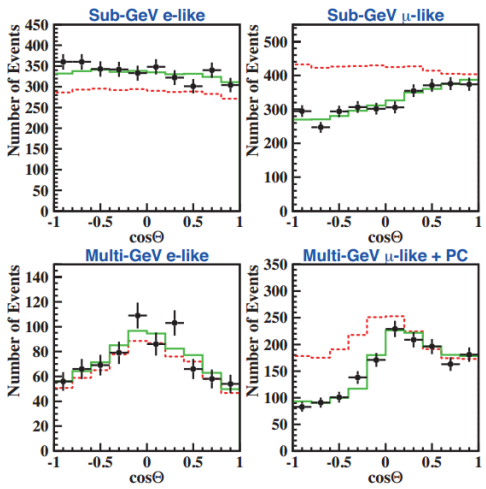

Figure 2.5 Zenith angle distributions for fully contained e-like and μ-like events in Super-Kamiokande. Dotted (red) histograms show non-oscillated Monte Carlo events, and solid (green) histograms show best-fit expectations for $\nu_\mu \leftrightarrow \nu_\tau$ oscillations. Figure taken from the Super Kamiokande Collaboration [7].

$$\frac{\phi(\nu_e)}{\phi(\nu_e) + \phi(\nu_{\mu,\tau})} = 0.340 \pm 0.023(stat)^{+0.029}_{-0.031}(syst)$$

(2.1)

The Kamioka Liquid Scintillator Antineutrino Detector (KamLAND) experiment was the first to observe, in 2002, evidence for reactor (anti)ν_e oscillations. The experiment is an 18 m wide spherical vessel with 1,879 50 cm PMTs. It measures electron antineutrino flux with a 1.8 MeV threshold created through inverse beta decay. 365 $\pm$ 24 events were expected in a non-oscillating case, but only 258 events were observed, suggesting oscillation [9].

These experiments provided the first measurements of the solar oscillation parameters θ_{12} and Δm_{12}^2, allowing for a limit on the parameters $\sin 2\theta = 0.86^{+0.03}_{-0.04}$ and $\Delta m_{12}^2 = 8.0$ +/- 0.3 E-5 eV^2.

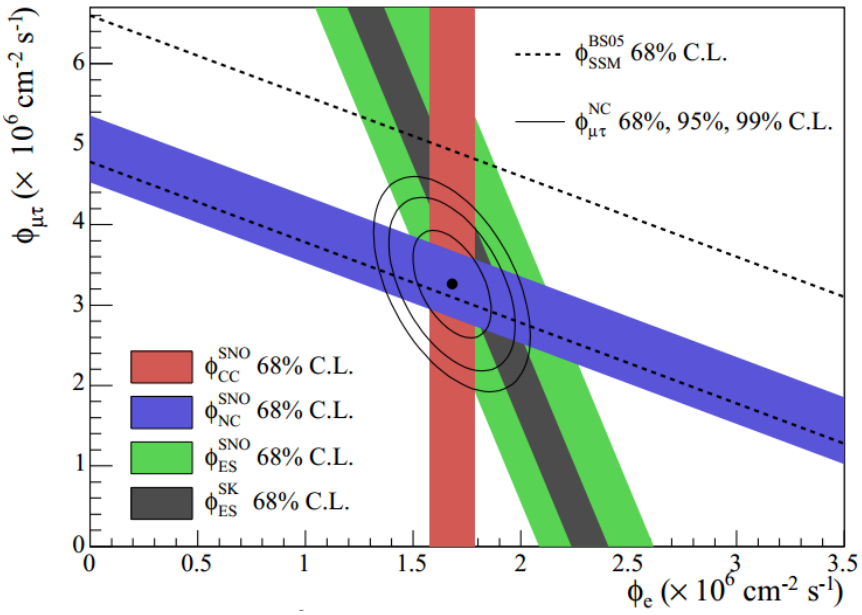

Figure 2.6 The flux of muon and tau neutrinos versus the flux of electron neutrinos in each of the three possible interactions detectable by SNO [8]. Super-K's electron scattering data is included [9].

Pontecorvo's idea of neutrino oscillation proposed that the neutrino flavor states observed in detectors were a linear superposition of mass states, which are what propagate through space [10]. The weakly interacting flavor states ν_e, ν_μ, ν_τ can be expressed as superpositions of mass states ν_1, ν_2, ν_3, each propagating through space with characteristic frequencies due to their masses, m_1, m_2, and m_3. It is this superposition that is seen experimentally, as the changing composition of neutrino flavors through flight, not the individual mass states.

The mathematical representation of the superposition of neutrino mass states is the PMNS matrix, a matrix analogous to the CKM matrix for quark mixing [11],

$$\begin{bmatrix} \nu_e \\ \nu_\mu \\ \nu_\tau \end{bmatrix} = \begin{bmatrix} U_{e1} & U_{e2} & U_{e3} \\ U_{\mu 1} & U_{\mu 2} & U_{\mu 3} \\ U_{\tau 1} & U_{\tau 2} & U_{\tau 3} \end{bmatrix} \begin{bmatrix} \nu_1 \\ \nu_2 \\ \nu_3 \end{bmatrix} \tag{2.2}$$

where U is the PMNS matrix [12],

$$\boldsymbol{U} = \begin{bmatrix} \mathbf{1} & \mathbf{0} & \mathbf{0} \\ \mathbf{0} & \boldsymbol{c_{23}} & \boldsymbol{s_{23}} \\ \mathbf{0} & \boldsymbol{-s_{23}} & \boldsymbol{c_{23}} \end{bmatrix} \times \begin{bmatrix} \boldsymbol{c_{13}} & \mathbf{0} & \boldsymbol{s_{13}e^{-i\delta}} \\ \mathbf{0} & \mathbf{1} & \mathbf{0} \\ \boldsymbol{-s_{13}e^{i\delta}} & \mathbf{0} & \boldsymbol{c_{13}} \end{bmatrix} \times \begin{bmatrix} \boldsymbol{c_{12}} & \boldsymbol{s_{12}} & \mathbf{0} \\ \boldsymbol{-s_{12}} & \boldsymbol{c_{12}} & \mathbf{0} \\ \mathbf{0} & \mathbf{0} & \mathbf{1} \end{bmatrix} \times$$

$$\begin{bmatrix} \boldsymbol{e^{i\alpha_1/2}} & \mathbf{0} & \mathbf{0} \\ \mathbf{0} & \boldsymbol{e^{i\alpha_2/2}} & \mathbf{0} \\ \mathbf{0} & \mathbf{0} & \mathbf{1} \end{bmatrix}$$

$$=$$

$$\begin{bmatrix} \boldsymbol{c_{12}c_{13}} & \boldsymbol{s_{12}c_{13}} & \boldsymbol{s_{13}e^{-i\delta}} \\ \boldsymbol{-s_{12}c_{23} - c_{12}s_{23}s_{13}e^{i\delta}} & \boldsymbol{c_{12}c_{23} - s_{12}s_{23}s_{13}e^{i\delta}} & \boldsymbol{s_{23}c_{13}} \\ \boldsymbol{s_{12}s_{23} - c_{12}c_{23}s_{13}e^{i\delta}} & \boldsymbol{-c_{12}s_{23} - s_{12}c_{23}s_{13}e^{i\delta}} & \boldsymbol{c_{23}c_{13}} \end{bmatrix} \times$$

$$\begin{bmatrix} \boldsymbol{e^{i\alpha_1/2}} & \mathbf{0} & \mathbf{0} \\ \mathbf{0} & \boldsymbol{e^{i\alpha_2/2}} & \mathbf{0} \\ \mathbf{0} & \mathbf{0} & \mathbf{1} \end{bmatrix}$$

(2.3)

The parameters of the PMNS matrix include three mixing angles and the CP-violating phase. In the matrix, c = cos, and s = sin. The subscripts identify the mixing angle. The matrix is typically broken up into three matrices for experimental

convenience, each representing the three experimental regimes. The Dirac CP-violating term, with phase δ_{CP}, appears only in the θ_{13} sector. In the event of the leptonic violation of CP symmetry, this phase will be nonzero. Because this term appears only in the θ_{13} sector, we require θ_{13} to be nonzero as well, which recent experiments have shown to be the case.

The phase factors α_1 and α_2 will be observable only if the neutrino is found to be a Majorana particle, its own antiparticle. These Majorana CP-violating phases are not important for neutrino oscillations.

The θ_{23} sector is identified with atmospheric neutrino mixing and is driven by Δm^2_{23} = 2.43E-3 eV^2. The θ_{12} sector is identified with solar neutrino mixing and is driven by Δm^2_{12} = 7.59E-5 eV^2. The mixing angles determine the amount of mixing among the mass and flavor states.

The mass states propagate through space with a time dependent plane wave representation,

$$\left|\nu_i(t)\right\rangle = e^{-i(E_i t - \vec{p}_i \cdot \vec{L})} \left|\nu_i(0)\right\rangle$$

(2.4)

where E_i is the energy of the mass state i, $E = \sqrt{(P^2 - m_i^2)}$, t is the time from the start of the propagation, p_i is the momentum vector, and L is the position of the neutrino with respect to its starting position. The momentum is expressed by

$$p_i = \sqrt{E^2 - m_i^2} \cong E - \frac{m_i^2}{2E}.$$

(2.5)

Due to the low mass of the neutrinos we can say $m_i^2 << E^2$, and the energy in the phase can be given by

$$E_i t - p_i L \cong E(t - L) + \frac{m_i^2}{2E} L.$$

(2.6)

We may drop the phase factor E(t - L) by approximating that t = L, with L being the distance traveled. This is because the neutrino travels the distance L in the time t, and c = 1 (L = ct = t). Now the wave is represented by

$$\left|\nu_i(L)\right\rangle = \ e^{-im_i^2 L/2E} \ \left|\nu_i(0)\right\rangle.$$

(2.7)

The probability of a neutrino eigenstate (α) oscillating into another eigenstate (β) is given by

$$P_{\alpha\to\beta} = \left|\left\langle\nu_\beta\middle|\nu_\alpha(t)\right\rangle\right|^2 = \left|\sum_i U_{\alpha i}^* U_{\beta i} e^{-im_i^2 L/2E}\right|^2.$$

(2.8)

which can also be expressed as

$$\begin{aligned} P(\nu_\alpha \ \to \ \nu_\beta) &= \left|Amp(\nu_\alpha \ \to \ \nu_\beta)\right|^2 \\ &= \ \delta_{\alpha\beta} - \ 4\sum_{i>j} \Re\left(U_{\alpha i}^* U_{\beta i} U_{\alpha j} U_{\beta j}^*\right) \sin^2\left(\Delta m_{ij}^2 \frac{L}{4E}\right) \\ &+ \ 2\sum_{i>j} \Im(U_{\alpha i}^* U_{\beta i} U_{\alpha j} U_{\beta j}^*) \ \sin\left(\Delta m_{ij}^2 \frac{L}{4E}\right) \end{aligned}$$

(2.9)

This gives the probability that a neutrino starting in the state ν_α will be detected in the state ν_β after traveling a distance L [13][14]. The neutrinos themselves are massive, and a zero mass for neutrinos would eliminate all observed oscillation. The effect of matter on oscillations must be taken into account when neutrinos pass through matter, as in the Sun, or in Earth. The matter effects will allow the mass hierarchy of neutrinos to be determined.

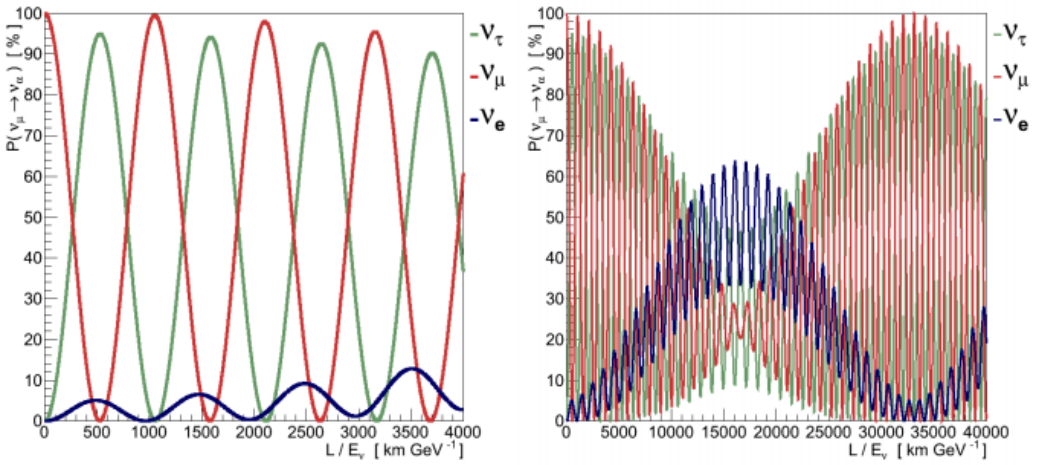

Figure 2.7. The probabilities of detecting neutrinos of different flavors when starting with a beam of ν_μ. Detection probability is a function of L/E, (km/GeV). These oscillations show the same behavior as coupled oscillators over long distances or with lower energies, revealing beat patterns.

2.4 Neutrinos in the Standard Model

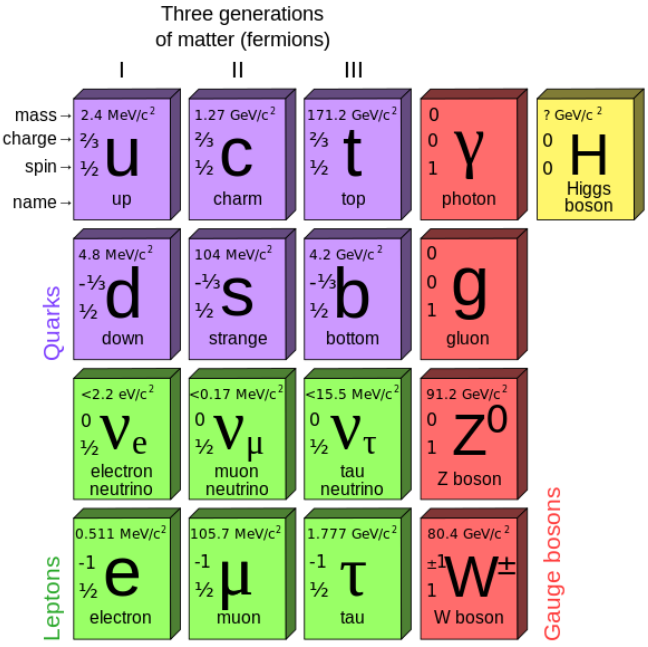

Figure 2.8. The elementary particles of the Standard Model.

The Standard Model is represented by the gauge group G_{SM} = U(1) x SU(2) x SU(3)

where hypercharge U(1) and isospin SU(2) correspond to the electroweak gauge group, and color symmetry SU(3) corresponds to quantum chromodynamics.

All information about three of the four fundamental forces (strong, weak, electromagnetic) and the elementary particles of matter is contained within the Standard Model. Particles are organized by generations and types, and broken up into fundamental classes: quarks, leptons, and force mediating gauge bosons.

Quarks and leptons are fermions, having spin ½. There are six leptons—three generations of two types (charged and neutral)—the charged particle type: the electron, muon, and tau; and neutral particle types corresponding to each generation: the electron neutrino, muon neutrino, and tau neutrino.

$$\begin{pmatrix}\nu_e\\ e\end{pmatrix}\ \begin{pmatrix}\nu_\mu\\ \mu\end{pmatrix}\ \begin{pmatrix}\nu_\tau\\ \tau\end{pmatrix}$$

The charged fermions are Dirac particles, and have associated antiparticles: the positron, the mu minus, and the tau minus. Due to their neutral charge it is currently unknown if neutrinos are Majorana particles, meaning they could be their own antiparticles. If they are not, they are Dirac fermions like the electron, muon, and tau. This matter has yet to be settled in particle physics.

Charged leptons interact via the electromagnetic force while the uncharged neutrinos interact via the weak nuclear force.

The quarks, too, come in three generations of two types (up type and down type): up and down; charm and strange; top and bottom.

$$\begin{pmatrix}u\\ d\end{pmatrix}\ \begin{pmatrix}c\\ s\end{pmatrix}\ \begin{pmatrix}t\\ b\end{pmatrix}$$

Like the leptons, quarks have oppositely charged antiparticles corresponding to each, called antiquarks. Quarks interact with each other via the strong force, due to their color charge, and with other fermions via the weak and electromagnetic forces.

Gauge bosons are force carrying particles, which mediate the forces mentioned above. The W+, W-, and neutral Z bosons mediate the weak interaction among particles with weak isospin, eight gluons mediate the strong force among particles of color charge, and photons mediate the electromagnetic force among particles with electric charge. Recent findings at CERN have confirmed the existence of the Higgs boson, the boson responsible for generating mass in other particles.

It is the electroweak interaction mediated by the W and Z bosons that is relevant for neutrinos and the study of their properties. The electroweak theory, which unified the electromagnetic and weak interactions among elementary particles, was developed by Sheldon Lee Glashow, Abdus Salam, and Steven Weinberg, for which they won the 1979 Nobel Prize in Physics. The W bosons mediate charged current interactions (CC) and the Z boson mediates neutral current (NC) interactions [15].

Studying neutrinos opens up potential doors to physics beyond the Standard Model. In the Standard Model, neutrinos are without mass. In reality, however, experiment suggests the presence of neutrino masses, as implied by neutrino oscillation.

Massive neutrinos are therefore the first piece of evidence for physics beyond the Standard Model.

2.5 Weak Interactions

The neutrino has the unique quality of being the only particle that interacts through weak interactions alone. They possess no color charge and no electric charge, but have a weak hypercharge of -1.

The direct observation of neutrinos in experimental devices is made impossible by both the small cross sections associated with low energy weak interactions and the electrical neutrality of neutrinos. It is through the neutrino's interaction with other particles that we may observe its presence in detectors, and it is through the reconstruction of the resultant events that we are able to piece together information about these incident neutrinos. The weak interaction, therefore, is of utmost importance in neutrino physics.

Electroweak interactions are represented in the Standard Model through the unification of the electromagnetic and weak interactions, by the SU(2) x U(1) gauge group. These forces are mediated by the W gauge bosons of weak isospin from SU(2) and the B^0 boson of weak hypercharge from U(1), which mix to produce the Z boson and the photon. The W bosons mediate charged current (CC) interactions, and the Z boson mediates neutral current (NC) interactions. The photon mediates all electromagnetic interactions.

To develop the electromagnetic portion of the electroweak theory we start with the Lagrangian for a free Dirac fermion [16]

$$\mathcal{L}_0 = i\overline{\psi}(x)\gamma^\mu \partial_\mu \psi(x) - m\overline{\psi}(x)\psi(x) \tag{2.10}$$

where ψ is the field that describes the particle, m is its mass, and γ^μ are the Dirac matrices. This Lagrangian is invariant under a global U(1) gauge transformation

$$\psi(x) \rightarrow e^{i\alpha}\psi(x)$$

(2.11)

where α is an arbitrary real number. However, if the phase transformation depends on the space-time coordinate, the Lagrangian is not invariant. This is a local gauge transformation,

$$\psi(x) \rightarrow e^{i\alpha(x)}\psi(x)$$

(2.12)

and is invariant because

$$\partial_\mu\psi(x) \rightarrow e^{i\alpha}\psi(x)\big(\partial_\mu + i\alpha\partial_\mu x\big)\psi(x)$$

(2.13)

The gauge principle requires that the U(1) phase transformation holds locally, which necessitates one adding an additional term to the Lagrangian. This allows us to cancel the $\delta_\mu x$ term in (2.13). We introduce a new spin-1 field called $A_\mu(x)$ that transforms under local gauge transformation as

$$A_\mu(x) \rightarrow A_\mu(x) - \frac{1}{e}\partial_\mu\alpha(x)$$

(2.14)

We define the covariant derivative

$$D_\mu\psi(x) = \big(\partial_\mu + ie^{i\alpha}A_\mu\big)\psi(x)$$

(2.15)

which transforms like the field,

$$D_\mu\psi(x) \rightarrow e^{i\alpha}D_\mu\psi(x)$$

(2.16)

The gauge field A_μ is added in a term to the Lagrangian,

$$\mathcal{L} = \overline{\psi}\big(i\gamma^\mu\partial_\mu - m\big)\psi - e\overline{\psi}\gamma^\mu\psi A_\mu$$

(2.17)

and we apply the covariant derivative (2.15) to obtain a Lagrangian invariant under local U(1) transformations

$$\mathcal{L} \equiv i\overline{\psi}(x)\gamma^\mu D_\mu\psi(x) - m\overline{\psi}(x)\psi(x) = \mathcal{L}_0 - e\alpha A_\mu(x)\overline{\psi}(x)\gamma^\mu\psi(x). \qquad (2.18)$$

It is the introduction of this gauge field that generates interactions. Here it is an interaction between the Dirac fermion and the gauge field A_μ. To make A_μ a propagating field and to complete the locally invariant Lagrangian, we add a gauge invariant kinetic energy term

$$\mathcal{L}_{kin} \equiv -\frac{1}{4}F_{\mu\nu}(x)F^{\mu\nu}(x), \qquad (2.19)$$

where $F_{\mu\nu} = \partial_\mu A_\nu - \partial_\nu A_\mu$ is the electromagnetic field strength, invariant under (2.14). Local gauge invariance would be lost by the presence of a mass term for the gauge field, $L_m = \frac{1}{2} m^2 A^\mu A_\mu$, because $A^\mu A_\mu$ is not invariant under (2.14). Hence, the gauge field—and by extension, the photon—must be massless.

Having imposed local gauge invariance on our original Lagrangian and adding a massless gauge field, we have a complete locally invariant Lagrangian

$$\mathcal{L} = \overline{\psi}\left(i\gamma^\mu \partial_\mu - m\right)\psi - \frac{1}{4}F^{\mu\nu}F_{\mu\nu} - e\overline{\psi}\gamma^\mu\psi A_\mu$$

(2.20)

The last term in (2.20) represents the coupling of fermion fields ψ and $\bar{\psi}$ to the gauge field A_μ, the photon field that preserves gauge invariance [17]. When using the covariant derivative in (2.15) and defining $Đ = \gamma_\mu D_\mu$ we can simplify the Lagrangian further,

$$\mathcal{L} = \overline{\psi}\left(i\gamma^\mu D_\mu - m\right)\psi - \frac{1}{4}F^{\mu\nu}F_{\mu\nu}$$

$$= \overline{\psi}(iĐ - m)\psi - \frac{1}{4}F^{\mu\nu}F_{\mu\nu}$$

(2.21)

This is the Quantum Electrodynamic (QED) Lagrangian. The Lagrangians in (2.19) and (2.20) lead to the Maxwell Equations:

$$\partial_\mu F^{\mu\nu} = eJ^\nu \equiv e\alpha\overline{\psi}\gamma^\nu\psi$$

(2.22)

where J^ν is the fermion electromagnetic current and α, up until now an arbitrary real constant, is the corresponding electromagnetic charge [18].

We see here how the electromagnetic portion of the electroweak theory takes shape. To unify the electromagnetic and the weak portions of electroweak theory we must now examine the weak interactions, and see how the W and Z bosons obtain their masses

A 1956 experiment by physicist Chien-Shiung Wu showed that neutrinos have a left-handed chirality and anti-neutrinos have a right-handed chirality. Because the left-handed fermion field has a non-trivial representation in the SU(2) we can put the left handed states into the doublet representation of that group,

$$L_e = \begin{pmatrix} \nu_e \\ e^- \end{pmatrix}_L, \qquad L_\mu = \begin{pmatrix} \nu_\mu \\ \mu^- \end{pmatrix}_L, \qquad L_\tau = \begin{pmatrix} \nu_\tau \\ \tau^- \end{pmatrix}_L$$

(2.23)

These will couple to the W+ and W-, but the right-handed states will not. They can be represented as SU(2) singlets.

$$l_e = e_R,\ l_\mu = \mu_R,\ l_\tau = \tau_R.$$

(2.24)

A massless gauge boson acquires mass through spontaneous symmetry breaking, via the Higgs mechanism. This is how the W, Z, and γ connect to the gauge fields, and how the W and Z bosons become massive. Glashow, Weinberg, and Salam based their theory of electroweak forces on a spontaneously broken SU(2) x U(1) gauge group. Four vector fields are required for the position dependent rotation of a field φ in the SU(2) x U(1) space. Three of these fields correspond to the SU(2) group, (W^a_μ), and one comes from the U(1) group, (B_μ) [17] [16].

Gauge boson mass terms are generated through the spontaneous breaking of symmetry, via the interaction with a scalar field H of the group SU(2), which has a vacuum expectation value

$$\langle H \rangle = \frac{1}{\sqrt{2}} \begin{pmatrix} 0 \\ v \end{pmatrix}$$

(2.25)

To get our masses, let us define a new covariant derivative represented by the vector fields required for the rotation of φ discussed above.

$$D_\mu \phi = \left(\partial_\mu - igA^a_\mu \tau_a - \frac{i}{2} g' B_\mu \right) \phi$$

(2.26)

Where $\tau_a = \sigma_a/2$, with σ being the Pauli matrices, and g and g' are the coupling strengths for SU(2) and U(1) gauge groups, respectively.

Squaring (2.26) and evaluating it at the vacuum expectation value (1.24), we begin to build the electroweak Lagrangian that will give us our gauge boson masses.

$$\mathcal{L} = \frac{1}{2}(0\ v)\left(gA_\mu^a\tau^a + \frac{1}{2}g'B_\mu\right)\left(gA^{b\mu}\tau^b + \frac{1}{2}g'B^\mu\right)\begin{pmatrix}0\\ v\end{pmatrix}$$

(2.27)

Using the Pauli matrices and evaluating the matrix product we get,

$$\mathcal{L} = \frac{1}{2}\frac{v^2}{4}\left[g^2\left(A_\mu^1\right)^2 + g'^2\left(A_\mu^2\right)^2 + \left(-gA_\mu^3 + g'B_\mu\right)^2\right]$$

(2.28)

where B_μ are massless U(1) gauge bosons, and the massive vector bosons W_μ and Z_μ can be defined in terms of B_μ and the massless SU(2) gauge field $\bar{A}_\mu = (A_\mu{}^1, A_\mu{}^2, A_\mu{}^3)$.

$$W_\mu^\pm = \frac{1}{\sqrt{2}}\left(A_\mu^1 \mp iA_\mu^2\right)$$

$$Z_\mu^0 = \frac{1}{\sqrt{g^2 + g'^2}}\left(gA_\mu^3 - g'B_\mu\right)$$

$$A_\mu = \frac{1}{\sqrt{g^2 + g'^2}}\left(g'A_\mu^3 + gB_\mu\right)$$

(2.29)

The Lagrangian (2.28) can now be written as

$$\mathcal{L} = \frac{1}{2}\frac{v^2}{4}\left(g^2W_\mu^+W^{-\mu} + (g^2 + g'^2)Z_\mu^0Z^{0\mu}\right)$$

(2.30)

The covariant derivative (2.15) can be written as,

$$D_\mu = \partial_\mu - igT^aA_\mu^a - ig'YB_\mu$$

$$= \partial_\mu - i\frac{g}{\sqrt{2}}\left(W_\mu^+T^+ + W_\mu^-T^-\right) - i\frac{1}{\sqrt{g^2 + g'^2}}Z_\mu^0(g^2T^3 - g'^2Y)$$

$$- i\frac{gg'}{\sqrt{g^2 + g'^2}}A_\mu(T^3 + Y)$$

(2.31)

with,

$$T^{\pm} = (T^1 \pm iT^2) = \frac{1}{2}(\sigma^1 \pm i\sigma^2) = \sigma^{\pm}$$

(2.32)

The electron charge e is represented in the covariant derivative as

$$e = \frac{gg'}{\sqrt{g^2 + g'^2}}$$

(2.33)

and the electric charge quantum number is given by $Q = T^3 + Y$, where T^3 is weak isospin and Y is weak hypercharge.

We introduce the weak mixing angle, θ_W, which describes the rotation of the W^0 and B^0 vector bosons to produce the Z^0 boson and the photon via spontaneous symmetry breaking.

$$\begin{pmatrix} \gamma \\ Z^0 \end{pmatrix} = \begin{pmatrix} \cos\vartheta_W & \sin\vartheta_W \\ -\sin\vartheta_W & \cos\vartheta_W \end{pmatrix} \begin{pmatrix} B^0 \\ W^0 \end{pmatrix}$$

(2.34)

where,

$$\cos\vartheta_W = \frac{g}{\sqrt{g^2 + g'^2}}, \quad \sin\vartheta_W = \frac{g'}{\sqrt{g^2 + g'^2}}$$

(2.35)

We can express the electron charge's magnitude in terms of the weak mixing angle,

$$e = g\sin\vartheta_W = g'\cos\vartheta_W$$

(2.36)

We see that $g = e/\sin\theta_W$. Using this, we can express the covariant derivative that describes the W and Z^0 coupling to fermions, given by

$$D_\mu = \partial_\mu - i\frac{g}{\sqrt{2}}\left(W_\mu^+ T^+ + W_\mu^- T^-\right) - i\frac{g}{\cos\vartheta_W} Z_\mu (T^3 - \sin^2\vartheta_W \alpha) - ieA_\mu \alpha$$

(2.37)

The Lagrangian for the coupling between gauge bosons and leptons is given by

$$\mathcal{L}_{electroweak} = \frac{g}{\sqrt{2}}\left(W_\mu^+ J_W^{\mu+} + W_\mu^- J_W^{\mu-}\right) + \frac{g}{\cos\vartheta_W} Z_\mu^0 J_Z^\mu + eA_\mu J_{EM}^\mu$$

(2.38)

in which,

$$J_W^{\mu+} = \overline{\nu}_L \gamma^\mu e_L + \overline{u}_L \gamma^\mu d_L$$

$$J_W^{\mu-} = \overline{e}_L \gamma^\mu \nu_L + \overline{d}_L \gamma^\mu u_L$$

$$J_Z^\mu = \sum_f \overline{f}\,\gamma^\mu (T^3 - \sin^2\vartheta_W \alpha) f$$

$$= \overline{\nu}_L \gamma^\mu \left(\frac{1}{2}\right)\nu_L + \overline{e}_L \gamma^\mu \left(-\frac{1}{2} + \sin^2\vartheta_W\right) e_L + \overline{e}_R \gamma^\mu (\sin^2\vartheta_W) e_R$$

$$+ \overline{u}_L \gamma^\mu d_L \left(\frac{1}{2} - \frac{2}{3}\sin^2\vartheta_W\right) u_L + \overline{u}_R \gamma^\mu \left(-\frac{2}{3}\sin^2\vartheta_W\right) u_R$$

$$+ \overline{d}_L \gamma^\mu d_L \left(-\frac{1}{2} + \frac{1}{3}\sin^2\vartheta_W\right) d_L + \overline{d}_R \gamma^\mu \left(\frac{1}{3}\sin^2\vartheta_W\right) d_R$$

$$J_{EM}^\mu = \overline{e}\gamma^\mu (-1) e + \overline{u}\gamma^\mu \left(+\frac{2}{3}\right) u + \overline{d}\gamma^\mu \left(-\frac{1}{3}\right) d.$$

(2.39)

The first term in (2.39) handles all charged current interactions mediated by the W^+ and W^- gauge bosons [18]. The second term describes neutral current interactions mediated by the Z^0, while the last term represents electromagnetic interactions mediated by the photon, depicted by the gauge field A_μ.

The $W^\pm$ and Z^0 acquire mass, with the $W^\pm$ mass given by,

$$m_{W\pm} = \frac{gv}{2}$$

(2.40)

and the Z^0 mass is given by,

$$m_{Z^0} = \frac{\sqrt{g^2 + g'^2}}{2} v.$$

(2.41)

The masses are not predicted by the Standard Model, but are measured to be

$M_W = 80.385+/-.015$ GeV/c^2, $M_Z = 91.1867+/-.0021$ GeVc^2

The currents of the W and Z bosons are

$$j_{\mu}^{\pm} = \overline{u}\frac{-ig_W}{2\sqrt{2}}(\gamma^{\mu} - \gamma^{\mu}\gamma^5)u$$

$$j_{\mu}^{0} = \overline{u}\frac{-ig_Z}{2}(g_V\gamma^{\mu} - g_A\gamma^{\mu}\gamma^5)u$$

(2.42)

where γ^{μ} are the Dirac matrices, g_W and g_Z are coupling strengths for the W and Z bosons, u and $\overline{u}$ are Dirac spinors, and $\gamma^5 = i\gamma^1\gamma^2\gamma^3$.

The coupling strengths in these interactions are related through the weak mixing angle.

$$\frac{g_W}{g_Z} = \cos\vartheta_W$$

(2.43)

The value of ϑ_W depends upon the value of Q, the momentum transfer at which it is measured. Experiments at SLAC and Jefferson Labs have measured the mixing angle at low Q^2, via Møller scattering and parity violation electron scattering, respectively. The SLAC experiment measured the quantity $\sin^2\vartheta_W$ at Q = 0.16 GeV/c, obtaining the value $\sin^2\vartheta_W = 0.2397 \pm 0.0013$, and the Jefferson Lab experiment measured the same quantity at Q = 91.2 GeV/c obtaining the value $\sin^2\vartheta_W = 0.23120 \pm 0.00015$. The currently accepted value by NIST is $\sin^2\vartheta_W = 0.2223 \pm 0.0021$. All three values correspond to a mixing angle of approximately 30 degrees [19] [20] [21]. The Weinberg angle's value is not predicted by the Standard Model, nor is the reason for its measured value currently understood.

2.6 Neutrino Mass

Until the discovery of neutrino oscillations in 1998, neutrinos were treated as massless particles in the Standard Model. It is this oscillation of weak flavor states that first suggested that neutrinos, thought to be massless for decades, must have mass. Flavor oscillation is dependent upon mixing angles and the mass difference squared between neutrino states, requiring that $\Delta m^2_{ij} \neq 0$, where $\Delta m^2_{ij} = m_i^2 - m_j^2$, and i and j denote the

mass states. A nonzero mass difference implies that at least one of the neutrino masses must be nonzero.

There are three known neutrino flavors, three neutrino mass states, and three mass splittings associated with the states, given by Δm_{21}, Δm_{32}, and Δm_{31}. Only two are independent, $\Delta m_{31} = \Delta m_{21} + \Delta m_{32}$.

Experiments have shown that the mass differences for all neutrino oscillations are nonzero, meaning at least two of the three neutrino types are massive. Neutrino oscillations are insensitive to the neutrino masses themselves, depending instead only on the differences between masses, and so the direct measurement of neutrino mass is not discernible through oscillation measurements alone. The absolute neutrino mass scale is unknown.

Mass splitting has been observed between all neutrino mass states, but the sign of Δm^2_{31} remains to be determined. It is the sign of this mass difference that will determine the neutrino mass hierarchy. For $\Delta m^2_{31} > 0$ the mass hierarchy is called a "normal" hierarchy, but for $\Delta m^2_{31} < 0$ the mass hierarchy is "inverted".

Normal hierarchy: $m_3 \gg m_2 > m_1$

Inverted hierarchy: $m_2 > m_1 \gg m_3$

A current limit on neutrino mass has been set by the Troitsk experiment, by experimentally measuring an electron antineutrino mass in tritium beta-decay. It provides an experimental estimate for neutrino mass squared $m_\nu^2 = -0.67 \pm 2.53\ eV^2$, giving an upper limit of $m_\nu = 2.05$ eV, 95% CL [22]. This, however, is the measurement of a flavor state, a superposition of the three mass states. This does not reveal the masses of the mass states.

Beyond the three known neutrino flavor states lies the possibility of sterile neutrinos. If such a neutrino exists, other mass states may exist beyond the three already known. This would require an expansion of the neutrino mixing matrix. Sterile neutrinos, if they exist, do not interact via any known interactions except gravity.

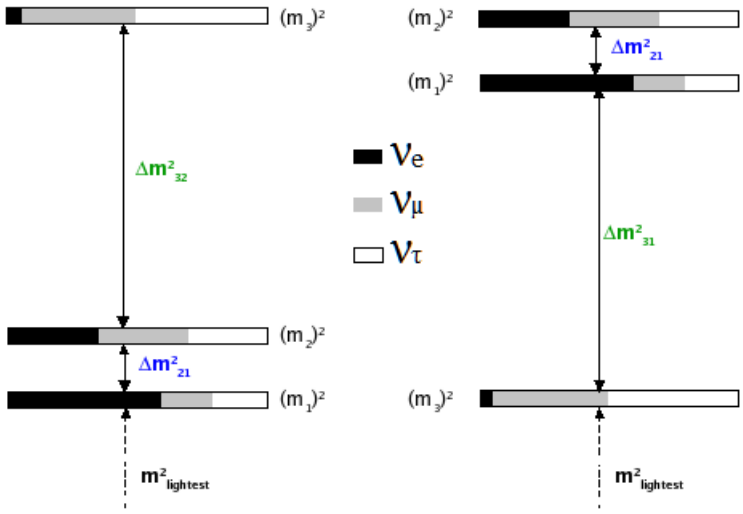

Figure 2.9. The normal (left) and inverted (right) hierarchies for neutrino flavors.

2.7 Neutrino Interactions

Neutrino interactions are mediated by the W and Z bosons, $W^{\pm}$ mediating charged current interactions, and the Z^0 boson mediating neutral current interactions. There are three categories of neutrino interactions, each of which will be discussed in depth [23] [24] [25]:

Charged current quasi-elastic and neutral current elastic interactions: The neutrino strikes a nucleon and the nucleon recoils. Lower energies are dominated by NC elastic scattering in which the nucleus recoils intact:

$$\nu + N \rightarrow \nu + X, \quad \overline{\nu} + N \rightarrow \overline{\nu} + X$$

where N is the nucleon, either n or p, and X is the final state hadron.

Larger energies allow CC quasi-elastic scattering, which leave a charged lepton in the final state:

$$\nu_\mu + N \rightarrow \mu^- + X, \quad \overline{\nu}_\mu + N \rightarrow \mu^+ + X$$

Resonance interactions: For higher energies, the neutrino excites the nucleon into a baryonic resonant state, which decays back to a nucleon, often times to be accompanied

by a single pion. Other final states are possible depending on the energy of the incoming neutrino.

$$\nu_\mu + N \rightarrow \mu^- + \Delta^{++} \rightarrow \mu^- + p + \pi^+$$
$$\nu_\mu + N \rightarrow \mu^- + \Delta^{+} \rightarrow \mu^- + n + \pi^+$$

Deep inelastic scattering: At the highest energies, neutrinos can scatter off the quarks within the nucleons, producing a lepton and a hadron. This mode is dominant for neutrino energies above 10 GeV.

Resonance interactions and deep inelastic scattering may occur in both charged current and neutral current processes.

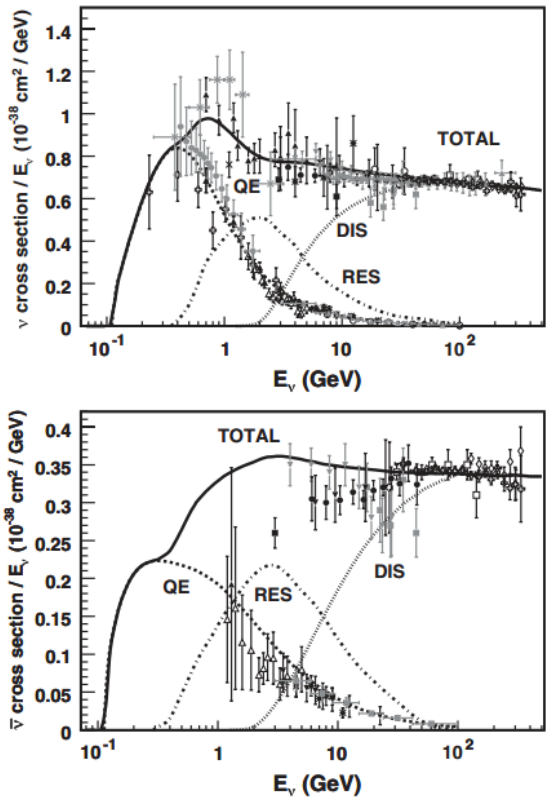

Figure 2.10. Neutrino and antineutrino CC cross sections in the GeV region, shown as σ/E_ν. Deep inelastic scattering, quasi-elastic, and single pion cross sections shown separately. [25]

2.7.1 Quasi-elastic Interactions

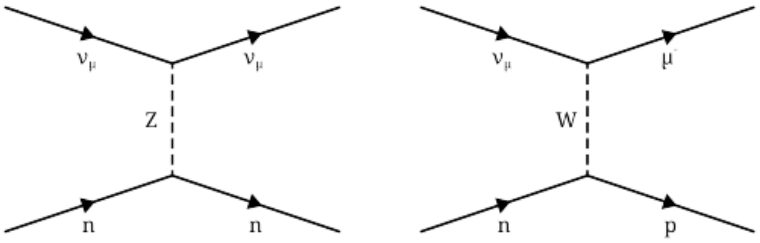

Figure 2.11. Neutral current electron elastic scattering (left) and charged current electron elastic scattering (right).

Neutral current elastic and charged current quasi-elastic interactions are the lowest energy neutrino interactions, occurring around less than 2 GeV. They provide a large source of signal events in neutrino oscillation experiments conducted at this energy. Neutrinos and antineutrinos scatter off of protons and neutrons in the nucleus in neutral current elastic scattering, and the nucleus remains intact. At slightly higher energies charged current interactions may occur, resulting in quasi-elastic scattering which places a massive charged lepton in the final state. This reaction type dominates for muon type neutrinos where $E_\nu < 1$ GeV. The following discussion borrow from [23]and [16].

For a charged current interaction, let us consider the process $\nu_\mu + e^- \rightarrow \mu^- + \nu_e$. It is represented by

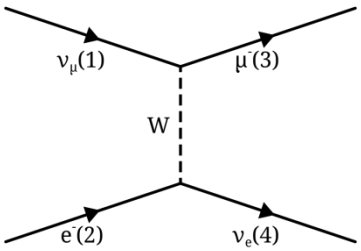

In this process, $q = p_1 - p_3$. The W propagator is given by

$$\frac{-i(g_{\mu\nu} - q_\mu q_\nu / M_W^2 c^2)}{q^2 - M_W^2 c^2}$$

(2.44)

For the condition $q^2 << M_W^2 c^2$ it reduces to

$$\frac{i g_{\mu\nu}}{(M_W c)^2}$$

(2.45)

From this we get the amplitude

$$M = \frac{g_W^2}{8(M_W c)^2} \left[\overline{u}(3)\gamma^\mu(1 - \gamma^5)u(1)\right]\left[\overline{u}(4)\gamma_\mu(c_V - c_A\gamma^5)u(2)\right]$$

(2.46)

There is a shortcut to finding matrix elements, called Casimir's trick, in which one sums over all spins, multiplies the matrices, and takes the trace.

$$\sum_{all\ spins} [\overline{u}(a)\Gamma_1 u(b)][\overline{u}(a)\Gamma_2 u(b)]^* = Tr\left[\Gamma_1(\not{p}_b + m_b c)\overline{\Gamma}_2(\not{p}_a + m_a c)\right]$$

(2.47)

where m_a and m_b are masses, c is the speed of light, and $\not{p} \equiv p^\mu\gamma_\mu$. By assuming negligible neutrino masses and by applying Casimir's trick we get

$$\sum_{spins} |M|^2 = \left(\frac{{g_W}^2}{8\,(M_W c)^2}\right)^2 Tr[\gamma^\mu(1 - \gamma^5)\,(\not{p}_1 + \mathrm{m_e c})\gamma^\nu(1 - \gamma^5)\,\not{p}_3]$$

$$\times Tr\left[\gamma^\mu(1 - \gamma^5)\not{p}_2\gamma^\nu(1 - \gamma^5)\left(\not{p}_4 + \mathrm{m_\mu c}\right)\right]$$

(2.48)

Taking both traces gives

$$8\left[p_1^\mu p_3^\nu + p_1^\nu p_3^\mu - g^{\mu\nu}(p_1 \cdot p_3) - i\varepsilon^{\mu\nu\lambda\sigma}p_{1\lambda}p_{3\sigma}\right]$$

(2.49)

for the first trace, and

$$8\left[p_{2\mu}p_{4\nu} + p_{2\nu}p_{4\mu} - g_{\mu\nu}(p_2 \cdot p_4) - i\varepsilon_{\mu\nu\kappa\tau}p_2^\kappa p_4^\tau\right]$$

(2.50)

for the second. And by the property that $\epsilon^{\mu\nu\lambda\sigma}\epsilon_{\mu\nu\kappa\tau} = -2(\delta_\kappa^\lambda\delta_\tau^\sigma - \delta_\tau^\lambda\delta_\kappa^\sigma)$, we can see that

$$\sum_{spins} |M|^2 = 4\left(\frac{g_W}{M_W c}\right)^4 (p_1 \cdot p_2)(p_3 \cdot p_4)$$

(2.51)

We want the average over initial spins. Although the electron has two spin states the neutrinos have only one. Therefore,

$$\langle |M|^2 \rangle = 2\left(\frac{g_W}{M_W c}\right)^4 (p_1 \cdot p_2)(p_3 \cdot p_4)$$

(2.52)

Moving to the center of mass frame, we can ignore the mass of the electron, and say

$$\langle |M|^2 \rangle = 8\left(\frac{g_Z}{M_Z c}\right)^4 \left\{1 - \left(\frac{m_\mu c^2}{2E}\right)^2\right\},$$

(2.53)

where E is the incident electron or neutrino energy. The general form of differential cross section for a two body reaction is given by

$$d\sigma = \frac{|M|^2}{4[((p1 \cdot p2)^2 - m_1^2 m_2^2]^{1/2}} d\Phi_f,$$

(2.54)

and is integrated to give the total cross section

$$\int d\Phi_f(p_3, p_4) = (2\pi)^4 \delta^4(p_3 + p_4 - p_1 - p_2) \frac{d^3 p_3}{(2\pi)^2 2E_3} \frac{d^3 p_4}{(2\pi)^3 2E_4}.$$

(2.55)

The isotropic differential scattering cross section of the charged current interaction is

$$\frac{d\sigma}{d\Omega} = \frac{1}{2}\left[\frac{\hbar c {g_W}^2 \mathrm{E}}{4\pi (M_W c^2)^2}\right]^2 \left\{1 - \left(\frac{m_\mu c^2}{2E}\right)^2\right\}^2.$$

(2.56)

Integrating over all angles gives us the total cross section

$$\sigma = \frac{1}{8\pi}\left[\left(\frac{{g_W}^2}{(M_W c^2)}\right)^2 \hbar c \mathrm{E}\right]^2 \left\{1 - \left(\frac{m_\mu c^2}{2E}\right)^2\right\}^2.$$

(2.57)

Now we consider an elastic neutral current interaction in which a neutrino scatters off an electron.

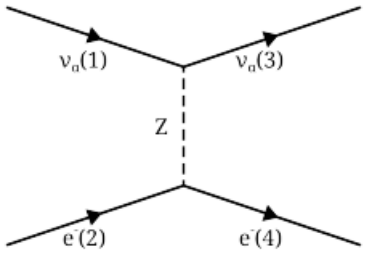

In the reaction $\nu_\mu + e \rightarrow \nu_\mu + e$ the Z^0 propagator is given by

$$\frac{-i(g_{\mu\nu} - q_\mu q_\nu / M_Z^2 c^2)}{q^2 - M_Z^2 c^2}$$

(2.58)

For the condition $q^2 << M_Z^2 c^2$ it reduces to

$$\frac{i g_{\mu\nu}}{(M_Z c)^2}$$

(2.59)

following the same reasoning as in the charged current interaction. Our amplitude is

$$M = \frac{g_z^2}{8(M_Z c)^2} \left[\overline{u}(3)\gamma^\mu(1 - \gamma^5)u(1)\right]\left[\overline{u}(4)\gamma_\mu(c_V - c_A\gamma^5)u(2)\right]$$

(2.60)

Using Casimir's trick we find

$$\begin{aligned}\langle|M|^2\rangle = 2\left(\frac{g_Z}{4\,M_Z c}\right)^4 & Tr[\gamma^\mu(1 - \gamma^5)\,\not{p}_1\gamma^\nu(1 - \gamma^5)\not{p}_3] \\ & \times Tr\left[\gamma_\mu(c_V - c_A\gamma^5)(\not{p}_2 + \text{mc})\,\gamma_\nu(c_V - c_A\gamma^5)(\not{p}_4 + \text{mc})\right] \\ & = \frac{1}{2}\left(\frac{g_Z}{M_Z c}\right)^4 \left[(c_V + c_A)^2(p_1 \cdot p_2)(p_3 \cdot p_4)\right. \\ & \left. + (c_V - c_A)^2(p_1 \cdot p_2)(p_2 \cdot p_3) - (mc)^2(c_V^2 - c_A^2)(p_1 \cdot p_3)\right]\end{aligned}$$

(2.61)

where m is the electron mass, and c_V and c_A are the neutral weak vector and axial couplings for the electron, specified by the GWS model:

Table 2.1. Neutral weak vector and axial couplings.

f	c_V	c_A
ν_ℓ	$+\frac{1}{2}$	$+\frac{1}{2}$
$\ell-$	$-\frac{1}{2}+2\sin^2\theta_w$	$-\frac{1}{2}$
q_u	$+\frac{1}{2}-\frac{4}{3}\sin^2\theta_w$	$+\frac{1}{2}$
q_d	$-\frac{1}{2}+\frac{2}{3}\sin^2\theta_w$	$-\frac{1}{2}$

Switching to the center of mass frame we can once more ignore the electron mass,

$$\langle|M|^2\rangle = 2\left(\frac{g_Z E}{M_Z c}\right)^4\left[(c_V + c_A)^2 + (c_V - c_A)^2\cos^4\frac{\theta}{2}\right] \tag{2.62}$$

where E is the energy of either electron or neutrino, and θ is the scattering angle. We find the differential scattering cross section to be

$$\frac{d\sigma}{d\Omega} = 2\left(\frac{\hbar c}{\pi}\right)^2\left(\frac{g_Z E}{4\,M_Z c}\right)^4 E^2\left[(c_V + c_A)^2 + (c_V - c_A)^2\cos^4\frac{\theta}{2}\right] \tag{2.63}$$

Integrating over all angles of the differential scattering cross section we get the total cross section

$$\sigma = \frac{2}{3\pi}(\hbar c)^2\left(\frac{g_Z}{2M_Z c}\right)^4 E^2(c_V^2 + c_A^2 + c_V c_A) \tag{2.64}$$

When speaking of neutrino or antineutrino quasi-elastic scattering what is meant is the processes $\nu_\mu + n \rightarrow \mu^- + p$ and $\overline{\nu}_\mu + n \rightarrow \mu^+ + p$ in which a charged lepton and single nucleon are ejected by the elastic interaction of a neutrino/antineutrino with a

nucleon. Quasi-elastic scattering is the dominant neutrino interactions at energies below 1 GeV, and provides a large signal sample in neutrino oscillation experiments [27]. Such a quasi-elastic interaction for neutrinos is depicted by the diagram

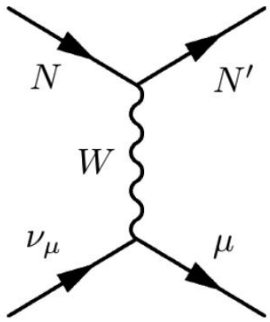

The amplitude of the interaction is

$$M = \frac{G}{\sqrt{2}}\overline{u}_{\mu}(p_3)\gamma_{\lambda}(1 - \gamma_5)u_{\nu}(p_1)\cos\vartheta_c\overline{u}_{p}(p_4)\Gamma_{CC}^{\lambda}(q^2)u_n(p_2)$$

(2.65)

where θ_C is the Cabibbo mixing angle that determines the probability of quark flavor mixing in weak interactions, and Γ_λ provides the weak form factors for the nucleon, which are functions of the four momentum q^2, and act to parameterize the amount of the weak currents present in the interaction

$$\Gamma_{\lambda} = \gamma_{\lambda}F_{v}^{1}(q^2) + \frac{i\sigma_{\lambda\nu}q^{\nu}\xi F_{V}^{2}(q^2)}{2M} + \frac{q_{\lambda}F_{V}^{3}(q^2)}{M} + \gamma_{\lambda}\gamma_5 F_{A}(q^2) + \frac{q_{\lambda}\gamma_5 F_{p}(q^2)}{M} + \frac{\gamma_{5(p1+p2)\lambda}F_{A}^{3}(q^2)}{M}$$

(2.66)

The differential quasi-elastic cross section can be written in the form of these nucleon form factors

$$\frac{d\sigma}{dq^2} = \frac{G_F^2 M^2\cos^2\vartheta_c}{8\pi E_{\nu}^2}\left[A(q^2) \mp B(q^2)\frac{(s-u)}{M^2} + \frac{(s-u)^2}{M^4}C(q^2)\right]$$

(2.67)

where G_F is the Fermi constant, the (-)+ corresponds to (anti)neutrino scattering, and the Lorentz invariant Mandelstam variables are s and u, defined as

$$s = (p_1 + p_2)^2 = (p_3 + p_4)^2 = M^2 + 2ME_\nu$$
$$u = (p_1 - p_4)^2 = (p_2 - p_3)^2 = M^2 + m^2 - 2ME_l$$

(2.68)

where p_1 and p_2 are the four momenta of the incoming particles and p_3 and p_4 are the four momenta of the outgoing particles.

The form factors in equation (2.66) describe the underlying nucleon structure [26]. F_V^1, F_V^2, and F_V^3 are the vector form factors, which have been well determined via electron scattering experiments. F_V^1 is the Dirac electromagnetic isovector form factor, and F_V^2 is the Pauli electromagnetic isovector form factor. The values of $A(q^2)$, $B(q^2)$ and $C(q^2)$ in equation (2.66) are given by

$$A(q^2) = \frac{m^2 - q^2}{4M^2}\left[\left(4 - \frac{q^2}{M^2}\right)|F_A|^2 - \left(4 + \frac{q^2}{M^2}\right)|F_V^1|^2 - \frac{q^2}{M^2}|\xi F_V^2|^2\left(1 + \frac{q^2}{4M^2}\right) - \frac{4q^2 F_V^1 \xi F_V^2}{M^2} - \frac{m^2}{M^2}((F_V^1 + \xi F_V^2)^2 + |F_A|^2)\right],$$

$$B(q^2) = \frac{q^2}{M^2}(F_V^1 + \xi F_V^2)^2 F_A,$$

$$C(q^2) = \frac{1}{4}\left(|F_A|^2 + |F_V^1|^2 - \frac{q^2}{4M^2}|\xi F_V^2|^2\right).$$

(2.69)

The Dirac and Pauli electromagnetic form factors may be expressed as functions of the Sachs form factors, which are known experimentally.

$$F_V^1(q^2) = \frac{1}{1 - \frac{q^2}{4M^2}}\left[G_E^V(q^2) - \frac{q^2}{4M^2}G_M^V(q^2)\right]$$

(2.70)

$$\xi F_V^2(q^2) = \frac{1}{1 - \frac{q^2}{4M^2}}[G_M^V(q^2) - G_E^V(q^2)]$$

(2.71)

The Sachs form factor values have been determined to be

$$G_E^V(q^2) = \frac{1}{\left(1 - \frac{q^2}{0.71GeV}\right)^2}$$

(2.72)

$$G_M^V(q^2) = \frac{1 + \mu_p - \mu_n}{\left(1 - \frac{q^2}{0.71GeV}\right)^2}$$

(2.73)

Due to T invariance, all form factors must be real. Due to charge symmetry $F^3_{V,A} = 0$, because it is the only imaginary form factor. Conserved vector current requires $F^3_V = 0$. The remaining vector form factors have been measured to good precision.

$$F_V(Q^2) \sim \frac{1}{\left(1 + q^2/{M_V}^2\right)^2}$$

(2.74)

Fp is the pseudo-scalar form factor, and ξ is the difference between anomalous magnetic moments of the proton and neutron, $\mu_p - \mu_n$.

F_A is the axial-vector form factor, which is a function of axial mass

$$F_A(Q^2) = \frac{g_A}{\left(1 + q^2/{M_A}^2\right)^2} + nuclear\ effects$$

(2.75)

Nuclear effects can change the cross section and kinematics of the final state. The nuclear effects considered in many neutrino experiments use the relativistic Fermi Gas model, in which the excitation of the nuclear system is accomplished by the transition of a nucleon from a state below the Fermi surface to one above the Fermi surface. These effects include the Fermi motion of the nucleons inside the target nucleus, the nucleon's binding energy within the nucleus, Pauli blocking, and final state interactions like re-scattering of the outgoing particle. The q^2 dependence has been taken from neutrino-nucleon quasi-elastic scattering data. M_A has been measured by a number of experiments, shown in Figure 2.12. The world average is $M_A = 1.026 \pm 0.021$ GeV [27].

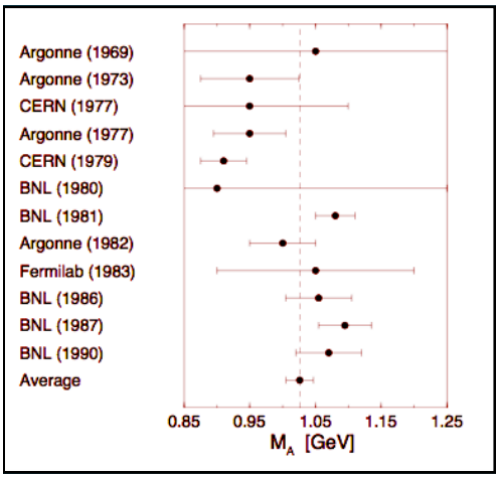

Figure 2.12. Experimental determination of the axial mass.

Figure 2.14 shows the current status of ν_μ and antiν_μ quasi-elastic scattering cross sections as a function of neutrino energy. A theoretical comparator is provided by the NUANCE neutrino event generator.

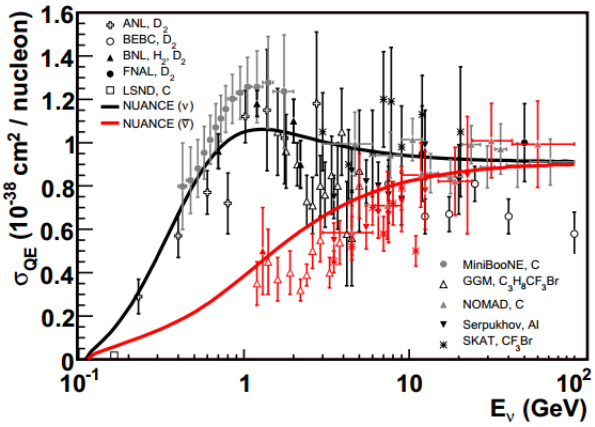

Figure 2.13. Data from numerous nuclear targets are shown, including ANL, BEBC, BNL, FNAL, LSND, Gargamelle, MiniBooNE, NOMAD, SKAT, and Serpukhov. The QE free nucleon scattering prediction assuming M_A = 1.0 GeV is shown as well, although the prediction is altered by nuclear corrections from neutrino-nucleus scattering. [27]

2.7.2 Resonance Interactions

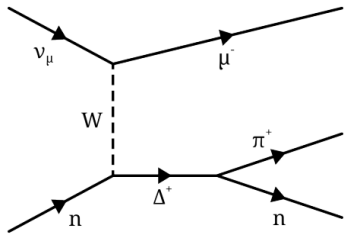

Figure 2.14. A charged current resonance interaction with a Δ^+ in the intermediate state and a single pion in the final state. The interaction is $\nu_\mu + n \rightarrow \mu^- + \Delta^+ \rightarrow \mu^- + n + \pi^+$.

When a higher energy neutrino interacts with a nucleon, the nucleon can be sent into a baryonic resonant state, after which it will quickly decay back to its original state, often emitting a pion in the process. This is an inelastic scattering process, and can occur in both CC and NC interactions. Although the single pion in the final state is most common in baryonic resonances, other final states may include kaons, photons, η and ρ mesons, or even multiple pions. The photon production process in resonance interactions are an important background for $\nu_\mu \rightarrow \nu_e$ appearance searches, because the $\pi^0 \rightarrow 2\gamma$ signal can look identical to the signal produced by an electron. Resonance production is most significant in the region between CC QE dominance and DIS dominance, 0.5 GeV < Eν < 10 GeV.

Neutrino induced single pion production is most commonly simulated with the Rein-Sehgal model, developed by Dieter Rein and Lalit Sehgal in 1981 [29] [30]. The model simulates both CC and NC resonance interactions. To obtain cross sections for particular channels the amplitude for each resonance production is calculated and multiplied by the probability of decay for that resonance into that channel. The model can be used to calculate the cross sections of single photon, kaon, and η productions by changing the decay probability of the resonances. Due to the model's original approximation of the muon mass being zero, the model has known discrepancies with recent pion production data, especially for low Q^2. Recent generators attempt to overcome the weaknesses of the model by using more appropriate form factors, or by

instead relying on electro-production data for the vector contribution and fit bubble chamber data to determine the parameters of the axial contribution.

The differential cross section for a single Δ resonance can be calculated by

$$\frac{\partial\sigma}{\partial \mathrm{q}^2\,\partial \mathrm{E_q}} = \frac{G_F^2\cos(\vartheta_c)^2}{8\pi^2}\frac{q^2}{Q^2}\frac{\Gamma}{(W-M_\Delta)^2+\frac{\Gamma^2}{4}}(u^2\sigma_- + v^2\sigma_+ + 2uv\sigma_0)$$

(2.76)

where $\frac{\Gamma}{(W-M_\Delta)^2+\frac{\Gamma^2}{4}}$ is the Breit-Wigner propagator, Γ is the width of the resonance, W is the resonance invariant mass, where the values for $\sigma_\pm$ and σ_0 are given by

$$\sigma_\pm = \frac{\mathrm{m_\Delta}}{\mathrm{m_N}}\frac{1}{2}\sum_{\mathrm{j_z}} \mathrm{f}^2_{\pm \mathrm{jz}}$$

(2.77)

$$\sigma_0 = -\frac{\mathrm{m_N}}{\mathrm{m_\Delta}}\frac{\mathrm{Q}^2}{\mathrm{q}^2}\sum_{\mathrm{jz}} \mathrm{f}^2_{0,\mathrm{jz}}$$

(2.78)

where $f_{k,jz} = \langle N, j_z + k\,|F_k|\Delta, j_z\rangle$.

2.7.3 Deep Inelastic Scattering Interactions

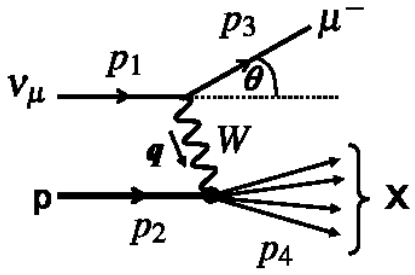

Figure 2.15. A deep inelastic scattering interaction between a muon neutrino and a proton, producing a μ^- and a hadron in the final state. $\nu_\mu + p \rightarrow \mu^- + X$.

For the highest energy neutrino interactions, dominating above 10 GeV, the neutrino can scatter off the quarks within the nucleons to produce a lepton and hadron in

the final state. This hadronization appears as a jet of strongly interacting particles. This can allow the internal structure of the nucleon to be resolved. The quarks "seen" by the neutrino depend upon the four-momentum transfer between neutrino and nucleon, carried by the virtual W boson.

When the nucleus is probed at sufficiently high energies the hadrons may behave as collections of point-like particles, and certain properties, such as scattering angle or momentum transfer, can be determined by dimensionless kinematic quantities. This is referred to as scaling, first proposed by James Bjorken in 1968. It is therefore sometimes referred to as Bjorken scaling. Three dimensionless kinematic invariants can describe DIS, one of which is the Bjorken variable x,

$$x = \frac{Q^2}{2p_2 q} = \frac{Q^2}{2M\nu} = \frac{Q^2}{2ME_\nu y}$$

(2.79)

$$y = \frac{E_{had}}{E_\nu}$$

(2.80)

$$Q^2 = -q^2 = -m_\mu^2 + 2E_\nu(E_\mu - p_3 \cos\vartheta_\mu)$$

(2.81)

where E_ν is the incident neutrino energy, M_N is the nucleon mass, $\nu = E_{had}$ is the energy of the hadronic system, and E_μ, $p_3 = p\mu$, and $\cos\vartheta$ are the energy, momentum and scattering angle of the outgoing muon in the laboratory frame [25].

We can write the inclusive neutrino and antineutrino induced DIS cross section using these variables,

$$\frac{d^2\sigma^{\nu,\beta}}{dxdy} = \frac{G_F^2 M E_\nu}{\pi\left(1 + Q^2/M_{W,Z}^2\right)^2}\left[\frac{y^2}{2}2xF_1(x,Q^2) + \left(1 - y - \frac{Mxy}{2E}\right)F_2(x,Q^2) \pm y\left(1 - \frac{y}{2}\right)xF_3(x,Q^2)\right].$$

(2.82)

where G_F is the Fermi weak coupling constant, $M_{W,Z}$ is the $W^\pm$ (Z^0 boson) mass, for CC (NC) scattering, and the +(-) is for neutrino (antineutrino) interactions. $F_i(x,Q^2)$ are the

dimensionless nucleon structure functions. Two structure functions appear for electron scattering, but a third is introduced for neutrino scattering for the V,A interference term. In the quark parton model of the nucleus the nucleon structure functions $F_i(x,Q^2)$ are expressed in terms of the target's quark composition. Charged lepton and and neutrino DIS experiments have measured these structure functions. Although equation (2.82) describes deep inelastic scattering there are additional effects that modify the scattering kinematics and cross sections, which need to be considered for a realistic description, including nuclear effects, radiative corrections, lepton masses, higher order QCD processes, heavy quark production, target mass effects, and nonperturbative effects.

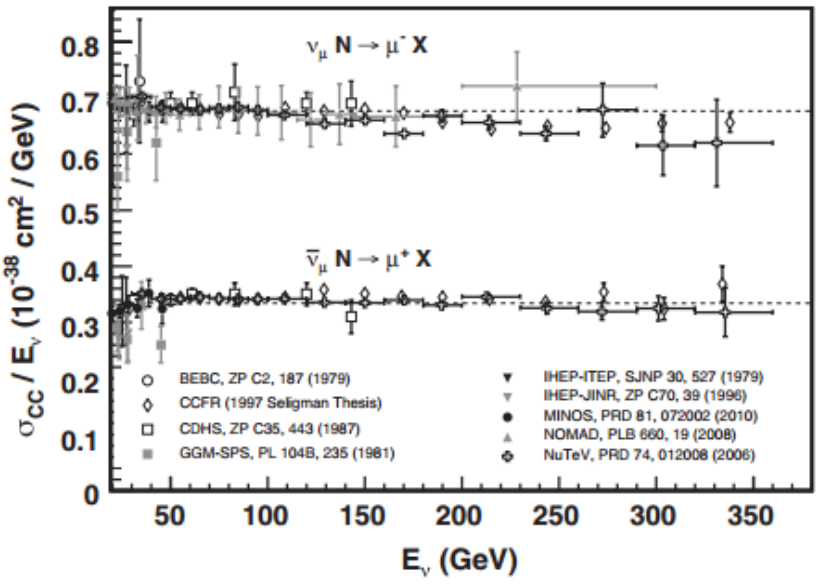

Figure 2.16. Measurements of inclusive neutrino and antineutrino CC cross sections divided by energy [25].

CHAPTER 3. COSMIC RAYS

3.1 Cosmic Ray Fundamentals

Before the advent of man-made particle accelerators, cosmic rays were a primary source of high energy particles for studies in physics. Although they were discovered in 1912 by Victor Hess, who would go on to win the Nobel Prize in physics, they continue to be an important area of study over a hundred years later. Studies of cosmic rays enabled the discovery of the positron and the muon, and currently serve to inform us about the makeup of matter outside the Solar system, as well as motivating the investigation of deep space processes that accelerate the particles to high energies.

Victor Hess's 1912 measurements entailed the use of a balloon carrying three electrometers to 5300 feet in altitude and measuring the change in radiation with altitude to try to explain the origin of radiation that was detectable everywhere on Earth, but which had no known source. His experiment was motivated by a discovery of Theodore Wulf who, in 1909, first noticed that radiation detected by electrometer was higher atop the Eiffel Tower than at its base. Hess discovered a large increase in the ionization rate at higher altitudes. The possibility of the Sun being the source of this radiation was eliminated when Hess sent a balloon up during a solar eclipse, and it was concluded that the source of radiation must be somewhere beyond the atmosphere [31].

Cosmic rays originate in outer space, in supernovae and galactic nuclei. Contrary to what the name implies, they are not rays of electromagnetic radiation, but atomic nuclei covering most of the periodic table, about 89% of which are hydrogen nuclei, or single protons. 9% are alpha particles, and single electrons and heavy nuclei each make up about 1% of the remainder. These account for what are called secondary cosmic rays, particles produced in interactions of interstellar gas with primary cosmic rays. Primaries are the particles initially accelerated by astrohpysical sources [32]. The nomenclature is different when talking about cosmic rays on Earth, in which the secondaries that interact in the atmosphere are referred to as primaries, and the daughter particles are referred to as secondaries. These are the definitions used in this thesis. The heavier nuclei cosmic rays

(composed of oxygen, carbon, magnesium, iron, and silicone) appear in the same relative abundance as these nuclei appear in our solar system, since these are produced in stars. However, there is an overabundance of rare elements like lithium, boron, and beryllium produced when primary heavier nuclei cosmic rays interact with interstellar gas and fragment into secondaries. There is also evidence that nucleosynthesis of cosmic rays differ from that of solar system matter, in the overabundance of ^{22}Ne [33].

The spectra of the components of cosmic radiation can be described in four ways, corresponding to different stages of their propogation and location, or different means of measurement:

1. *Particles per unit rigidity*. The gyroradius multiplied by the magnetic field strength gives the magnetic rigidity, which drives the propagation and acceleration of cosmic rays through interstellar magnetic fields, by the relation:

$$R = \frac{pc}{Ze} = r_g B \tag{3.1}$$

   where p is momentum, c is the speed of light, Z is atomic number, e is the charge of an electron, B is magnetic field strength, and r_g is the gyroradius.
2. *Particles per energy per nucleon*. Energy per nucleon is approximately conserved when a nucleon breaks up after interaction with interstellar gas, thus fragmentation depends on this quantity.
3. *Nucleons per energy per nucleon*. Secondary particles generated in collisions of primary cosmic rays with the atmosphere are dependent upon the intensity of nucleons per energy per nucleon. Whether the primaries are free protons or bound in nuclei does not matter.
4. *Particles per energy per nucleus*. Quantities related to total energy per particle are used in air shower experiments that use the atmosphere as a calorimeter.

These values are associated with the differential intensity of cosmic rays, I, which has units $m^{-2}s^{-1}sr^{-1}\xi^{-1}$, and are individually represented by ξ. Primary nucleon intensity in the energy range of a few GeV to beyond 100 TeV is approximated by

$$I_N(E) \approx 1.8 \times 10^4 \, (E/1\ GeV)^{\alpha} \, \frac{nucleons}{m^2 s\ sr\ GeV}$$

(3.2)

where E is the energy per nucleon, α ($\equiv \gamma + 1$) = 2.7 is the differential spectral index of the cosmic ray flux, and γ is the integral spectral index. Primary nuclei fractions are essentially constant over this range [32]. As charged particles, cosmic rays are affected by magnetic fields, undergoing a randomization in direction that makes the exact origins of Earth-detected cosmic rays impossible to determine. But observations of the electromagnetic radiation produced by cosmic rays outside the solar system make it possible to know where they are coming from, as well as where they are contained.

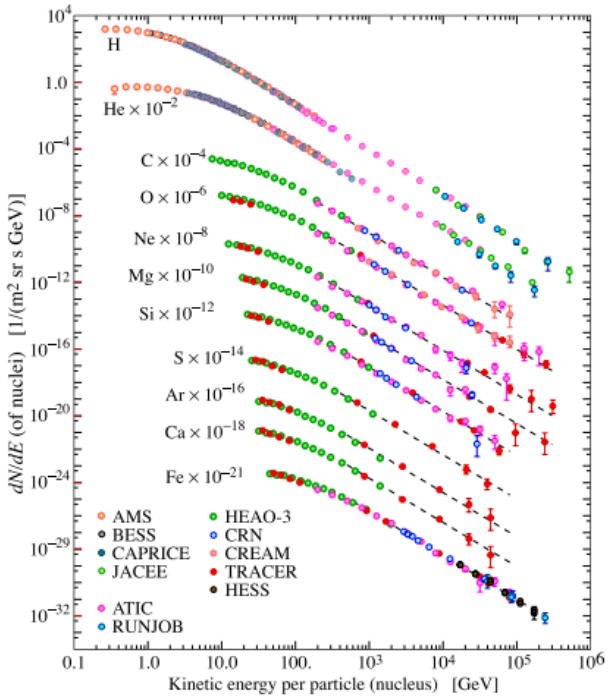

Figure 3.1. The fluxes of nuclei in primary cosmic particles per energy per nucleus plotted against energy per nucleus. These are the most abundant components for energies greater than 2 GeV/nucleon [32].

In 1951, radio synchrotron radiation emitted by cosmic ray electrons spiraling along the magnetic field lines of the Crab Nebula supernova remnant made it the first confirmed cosmic ray source by Y. Sekido, et al [34]. Observations of gamma ray emissions in hydrogen gas clouds near the center of our galaxy obtained with the High Energy Stereoscopic System (HESS) telescope array in Namibia in 2006 showed that the center of the Milky Way is another source of cosmic rays [35]. In 2013 an analysis of data collected by the Fermi Space Telescope confirmed that supernovae are general cosmic ray sources [36], although whether or not they are the most abundant sources remains to be known.

The accleration mechanism of cosmic rays is still undetermined, but supernovae explosions are thought to be the cause, accelerating particles as their shockwaves traverse the interstellar gas. The favored mechanism to explain cosmic ray acceleration is first order Fermi acceleration, also called diffusive shock acceleration, because in this model the particle performs a random walk that is described by diffusion, in which a charged particle moves through a shockwave and is reflected by magnetohydrodynamic (MHD) waves in the opposite direction at a higher velocity, and is repeatedly reflected back and forth across the shockwave by these magnetic mirrors until they are convected away from the shock. This is elaborated upon in the following discussion, from [37] and [38].

In first order Fermi acceleration the average energy of the particle after collision is $E = \beta E_0$where E_0 is the energy before collision and β is v/c. This energy gain per shock crossing being proportional to β gives the "first order" designation to this form of acceleration, differentiating it from second order Fermi acceleration, which is characterized by an energy gain proportional to the square of v/c. After *n* collisions there are $N = N_0 P^n$ particles with energies $E = \beta^n E_0$, where P is the probability that the particle remains inside the acceleration region after one collision. The resulting energy spectrum is

$$N(E)dE = constant \times E^{-1+\frac{lnP}{ln\beta}} dE. \quad (3.3)$$

The particle velocity distribution is isotropic in frames of reference that have the interstellar gas at rest on either side of the shock due to turbulence behind the shock and irregularities in front of it. A symmetry arises from this condition when a high-energy particle crosses the shock from upstream to downstream, or downstream to upstream. The particle gains energy in both types of crossing, with the average energy gained in a round trip given by

$$\langle \Delta E/E \rangle = \frac{4}{3}\,(v/c). \tag{3.4}$$

The probability that the particle escapes from the acceleration region is given by

$$P_{esc} = (1 - P) = \frac{4}{3}\left(\frac{v}{c}\right) \tag{3.5}$$

so that when replacing these two parameters in equation (3.3) we are left with

$$N(E)dE = constant \times E^{-2}\,dE \tag{3.6}$$

This acceleration mechanism is considered the most promising explanation of cosmic ray acceleration for its ability to predict a power law high-energy cosmic ray spectrum, although the observed spectrum has an exponent of 2.7, as shown in equation (3.2), instead of 2, as predicted. Cosmic rays cover a large energy range with an energy dependent flux that obeys the power law differential mentioned above, between 10^9 and 10^{14} eV and between 10^{15} and 10^{19} eV. This relationship is shown in Figure 3.2.

It is thought that the mean lifetime of galactic cosmic rays decreases with energy, as evidenced by the observation that the ratio of secondary to primary nuclei decreases with increasing energy. The knee and ankle features in Figure 3.2 are not well understood, but attempts to explain the knee hinge on the idea that, assuming the galactic cosmic ray portion of the spectrum is below 10^{18} eV, some cosmic accelerators, such as expanding supernova remnants, are incapable of accelerating particles above energies of 10^{15} eV. Multiple plausible explanations exist for the ankle, one being that extragalactic flux begin to dominate over galactic flux, causing a population of higher energy particles overtaking the population of lower energy particles.

It is also thought that the dip structure is due to $\gamma + p \rightarrow e^+ + e^-$ energy losses of extragalactic protons on the 2.7 K cosmic microwave background [32]. The ankle is interpreted as a signature of the extragalactic nature of the highest energy cosmic rays, which, if correct, implies galactic cosmic rays do not contribute to the cosmic spectrum above 10^{18} eV. NOvA's Far Detector is sensitive to the spectrum that includes the knee region, up to about 10^{17} eV, although only about 20 cosmic rays per year are expected to be seen originating from particles of that energy, while 4×10^6 cosmic rays per year will be seen from showers induced by particles of 10^{14} eV.

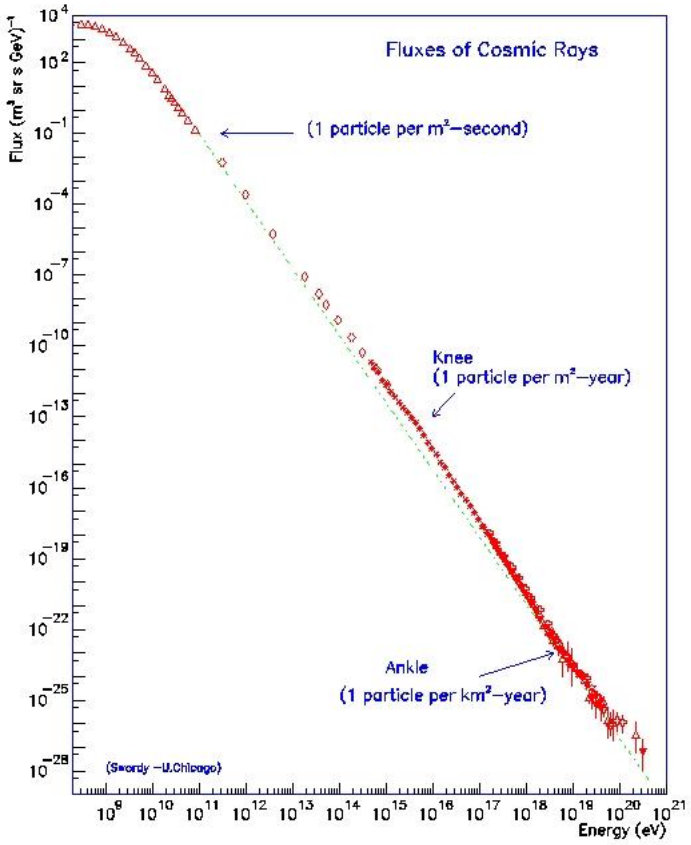

Figure 3.2. Cosmic ray flux as a function of energy. Two breaks in the spectrum's power law behavior occur, at the "knee" and "ankle", corresponding to 10^{15} and 10^{19} eV, respectively. Low energy cosmic particles are modulated by solar wind [39].

In Table 3.1 the relative abundances of cosmic ray nuclei at 10.6 GeV/nucleon are given, normalized to oxygen (= 1). These values do not necessarily extend to fluxes at higher energies because of the differing power law indices corresponding to each element.

Table 3.1. Relative abundances of cosmic ray nuclei at 10.6 GeV/nucleon, normalized to oxygen (= 1) [40], [41].

Z	Element	Relative Abundance
1	H	485
2	He	26
3-5	Li-B	0.40
6-8	C-O	2.20
9-10	F-Ne	0.30
11-12	Na-Mg	0.22
13-14	Al-Si	0.19
15-16	P-S	0.03
17-18	Cl-Ar	0.01
19-10	K-Ca	0.02
21-25	Sc-Mn	0.05
26-28	Fe-Ni	0.12

The heliosphere of the sun extends roughly 200 AU and shields much of the solar system region against galactic cosmic rays below a certain energy. This has been determined by observing the anti-correlation between cosmic ray fluxes at Earth and the 11 year solar cycle. The heliosphere ends at a boundary called the heliopause where the pressure of the interstellar medium is balanced with the pressure of the solar wind. In this region the solar winds slow down from supersonic (an average of 400 km/s) to subsonic speeds, causing compression, heating, and changes in the magnetic field. As the solar wind is slowed a shock is created, called the termination shock. At this barrier, about 90% of cosmic rays below 1 GeV are deflected. The precise amount of cosmic rays deflected depends upon the relative strength of the solar wind, which fluctuates throughout the solar cycle.

3.2 Cosmic Rays at Earth

Due to their diffusive propagation by the galactic magnetic field, and further modulation by the solar wind, cosmic rays reach Earth almost isotropically at most energies. Their collisions with the atmosphere produce air showers, cascades of particles including pions that decay into muons, neutrinos, and gamma rays. Alpha particles, neutrons, and kaons are also produced. Muons and gamma rays can lead to the production of electrons or positrons: muons via their decay into electron or positron, and gamma rays via interactions with atoms in the atmosphere, like oxygen and nitrogen.

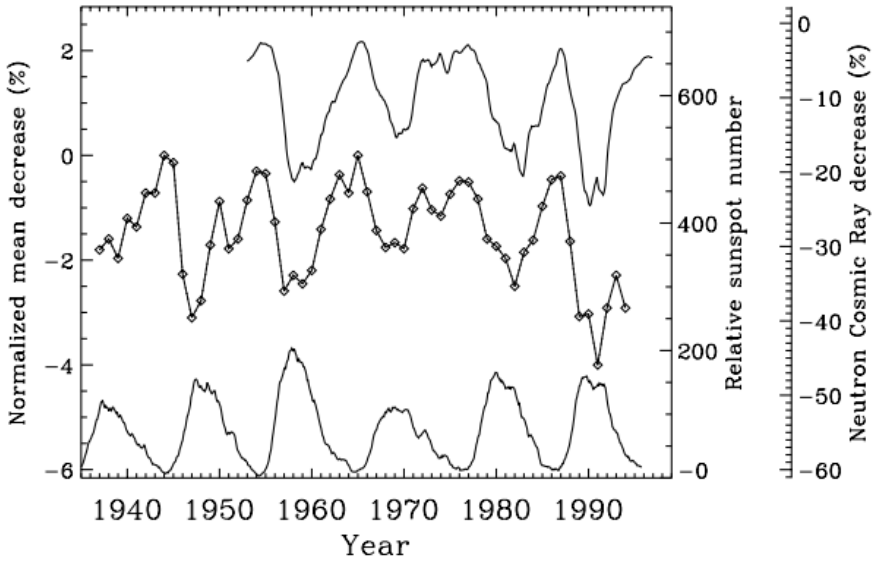

Figure 3.3. The anti correlation between solar activity and cosmic flux. The top curve is the cosmic ray flux measured at the neutron monitor in Climax, Colorado (1953 - 1996). The middle is the annual mean variation in cosmic ray flux as measured by ionization chambers (1937 - 1994). Neutron data has been normalized to May 1965, and ionization chamber data has been normalized to 1965. The bottom curve is the relative sunspot number [42].

The decay of neutral pions into photons creates a chain reaction of more photons, protons, antiprotons, electrons, and positrons. This produces an electromagnetic cascade.

Charged pions decay primarily into muons and neutrinos. Kaons, too, may decay to produce muons, as well as pions, permitting further cascades of electromagnetic radiation and muon and neutrino production. Muons and neutrinos are the most penetrating of the secondary particles, and are therefore the particles most commonly detected by ground based scintillation detectors, like NOvA. The decay chains described above for pions, kaons, muons, and neutrinos are shown below.

$$\pi^+ \rightarrow \mu^+ + \nu_\mu$$
$$\mu^+ \rightarrow e^+ + \nu_e + \bar{\nu}_\mu$$
(3.7)

The vertical flux of the cosmic ray components in the atmosphere for particles greater than 1 GeV are shown in Figure 3.4. These particles, except for electrons and protons, are produced in primary cosmic ray interactions in the atmosphere. Cosmic ray flux through the atmosphere is described by a set of coupled cascade equations that have boundary conditions at the top of the atmosphere in order to match the primary spectrum. This spectrum is then propagated through the atmosphere along with the associated secondaries via numerical or Monte Carlo calculations, and the interactions that produce new particles and cause the primaries to lose energy are taken into account. This method was used to produce Figure 3.4 [32].

Muons dominate the particle spectrum reaching the surface of the Earth, making them a large background in neutrino experiments. This is why many neutrino experiments place detectors underground; it is one of the only ways to shield against large cosmic muon backgrounds.

Muons are produced at an altitude of about 15 km and lose on average 2 GeV in ionization energy by the time they reach Earth's surface. At sea level the mean energy of muons is approximately 4 GeV, and their energy and angular distribution are a result of the convolution of the production spectrum, energy loss in the atmosphere, and decay [33]. The muon energy spectrum is almost flat below 1 GeV and steepens in the 10-100 GeV range, then steepens further at higher energies since pions with $E_\pi > \varepsilon_\pi$ (= 115 GeV) tend to interact with atmospheric matter before they can decay. Pions with energy lower

than this critical energy, however, tend to decay before they can interact with other particles in the atmosphere.

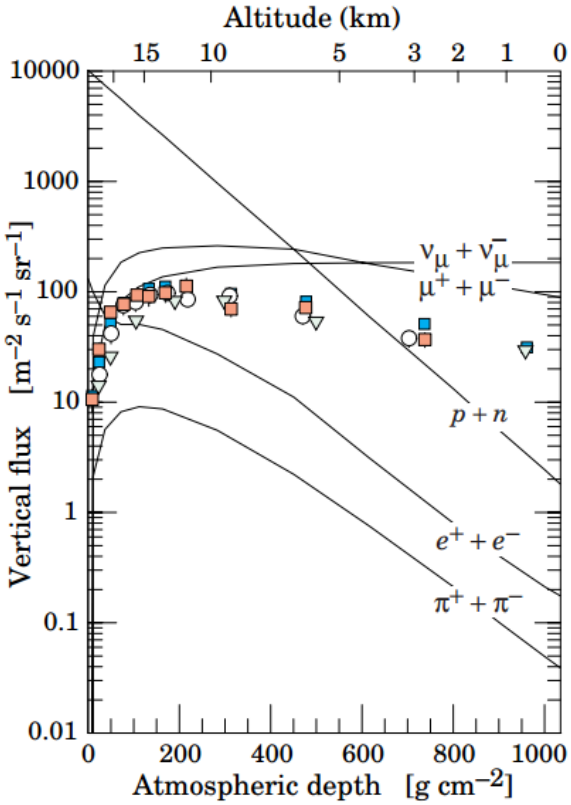

Figure 3.4. Vertical fluxes of cosmic rays above 1 GeV. These estimates were made with the nucleon flux in equation 3.2. Data points show the measurements of negative muons with $E_\mu > 1$ GeV [43] – [47].

The angular distribution of muons at ground level is proportional to $\cos^2\theta$, a characteristic of muons with $E_\mu \sim 3$ GeV. This distribution becomes steeper at lower energies and flattens at higher energies, approaching a $\sec\theta$ distribution at $E_\pi >> \varepsilon_\pi$ and $\theta < 70°$. Average muon energy at ground level increases at higher angles due to the low energy muons decaying before reaching the surface, and high energy pions decaying before they interact. The spectrum can be approximated, if decay is treated as negligible ($E_\pi > 100/\cos\theta$ GeV) and Earth's curvature is neglected ($\theta < 70°$), by the formula

$$\frac{dN_\mu}{dE_\mu d\Omega} = \frac{0.14\, E_\mu^{-2.7}}{cm^2 s\ sr\ GeV}\left\{\frac{1}{1+\frac{1.1\, E_\mu\, cos\theta}{115\ GeV}} + \frac{0.054}{1+\frac{1.1\, E_\mu\, cos\theta}{850\ GeV}}\right\}$$

(3.8)

where the first term in brackets gives the contribution of pions, and the second term gives the contribution of kaons.

Figure 3.5 shows the vertical flux of muons at the Earth's surface, which reveals the hardening of the muon spectrum for muons at higher angle of incidence. At ground level, the approximate total number of muons from an air shower with energies above 1 GeV is computed by [32]

$$N_\mu(>1\ GeV) \approx 0.95\ \times\ 10^5\ \left(\frac{N_e}{10^6}\right)^{3/4}$$

(3.9)

where N_e is the total number of charged particles in the shower. The distribution of muons per square meter, ρ_μ, as a function of lateral distance r from the center of the shower is

$$\rho_\mu = \frac{1.25\, N_\mu}{2\,\pi\,\Gamma(1.25)}\left(\frac{1}{320}\right)^{1.25} r^{-0.75}\left(1+\frac{r}{320}\right)^{-2.5}$$

(3.10)

where Γ is the gamma function. Muon lateral spread depends on transverse momenta of the muons at production, and on multiple scattering. The charged particle number density is given by

$$\rho_e = C_1(s,d,C_2)x^{(s-2)}(1+x)^{(s-4.5)}(1+\ C_2x^d)$$

(3.11)

where x is r/r_1, r_1 is the Moliere radius and is dependent upon the atmospheric density and therefore altitude at which the shower is detected, s, d, and C_2 are parameters that define the overall normalization constant C_1(s, d, C_2),

$$C_1(s,d,C_2) = \frac{N_e}{2\,\pi\, r_1^2}\ [B(s,4.5-2s) + \ C_2\ B(s+d,4.5-d-2s)]^{-1}$$

(3.12)

where B(m, n) is the beta function. Shower size (N_e), atmospheric depth, and primary nucleus determine the values of the parameters [33]. At sea level, $r_1 \approx 78$ m, and increases as air density decreases with higher altitude. Example parameter values given in [55] for $N_e \approx 10^6$ at sea level are s = 1.25, d =1, and $C_2 = 0.088$. Coulomb scattering of low-energy electrons determines the lateral spread of a shower, which is characterized by the Moilere radius.

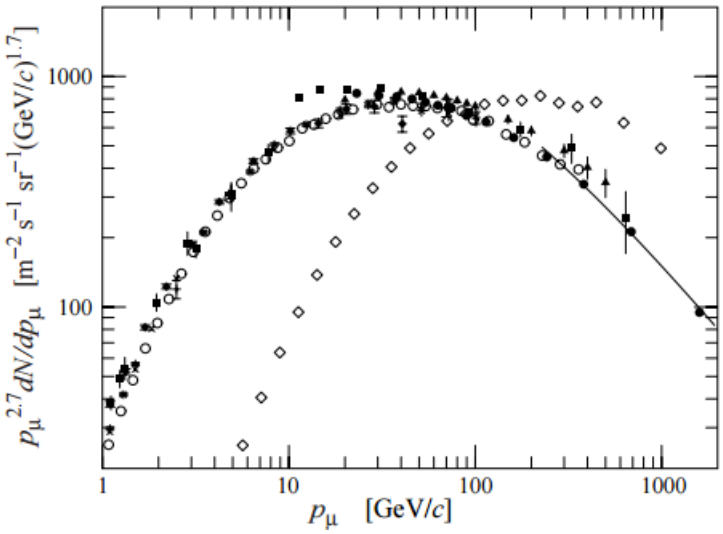

Figure 3.5. Spectrum of muons at θ = 0° and θ = 75°. The line is computed from equation 3.8. ♦[48], ■ [49], ▼[50], ▲[51], × + [52], ○ [53], ● [54], and for 75°, ◊[54]. Figure taken from [32].

3.3 The Forbush Effect

The Forbush effect (FE) is the decrease in the observed galactic cosmic ray intensity/density caused by an interplanetary coronal mass ejection (CME/ICME) passing through Earth's atmosphere and interplanetary magnetic field. This effect is named for Scott Forbush, who in 1937 made observations on the temporal changes in cosmic radiation at Earth. Using seventeen months of continuous ion chamber records from around the world he discovered correlated world-wide changes in cosmic ray intensities

measured at the stations. Forbush noted that the decreases occurred one or two days after large solar flares, and around the same time as geomagnetic storms. The variations were independent of atmospheric phenomena, and Forbush assumed the changes to be produced by perturbations of the geomagnetic field during geomagnetic storms. Observations made in the 1950s by Singer (1954, 1958) and Simpson et al. (1953) at the geomagnetic north pole suggested these variations were not solely due to geomagnetic field variations. Simpson and his colleagues measured a lower energy portion of the cosmic ray primary particle spectrum with neutron monitors and found that meteorlogical effects such as geomagnetic field variations did not seem to produce intensity decreases. They determined the effect was most likely related to solar activity, and not of terrestrial origin [56].

CMEs are massive eruptions of solar gas and the solar magnetic field which, upon leaving the sun, become part of the solar wind. These ejections are associated with solar flares and sunspots, and their effects can be observable on Earth. A halo event CME is an Earth-directed ejection, so called because of how the CME appears in a coronagraph image, as a halo of light around the occulting disk. A CME associated with a halo event may pass Earth, and may be capable of causing a Forbush effect observable on Earth-based particle detectors.

Due to the complex physical nature of the solar interactions and the variety of interplanetary activity, the theoretical framework on Forbush decreases is incomplete. A detailed and predictive modeling of the mechanism by which the CME causes the observed decrease does not currently exist [57]. What is known is that the magnetic field of the plasma solar wind accompanying a CME causes enhancements in the interplanetary magnetic field that sweep away lower energy cosmic rays. The behavior is measurable and well studied, largely by neutron monitors around the world. As of 2008, the NOAA defined the Forbush effect as an abrupt decrease, of at least 10%, of the background galactic cosmic ray intensity as observed by neutron monitors.

This definition, however, has been met with disagreement [57]. Physicists studying the Forbush effect say the decrease is not necessarily abrupt, sometimes occuring gradually. Nor are 10% decreases the norm, with the vast majority being much

smaller. Neutron monitors are not the only detectors used to measure the decrease, as evident in the very first observations made by Forbush, who used ionization chambers. Muon detectors below ground, above ground, and in space are also used to measure these decreases, although neutron monitors tend to be most common. A conventional definition of the Forbush effect is given by A.V. Belov, who says, "[the] Forbush effect is a result of the influence of coronal mass ejections (CMEs and ICMEs) and/or high speed streams of the solar wind from the coronal holes on the background cosmic rays." [57]

The Forbush effect is evident in cosmic ray profiles as a decrease in the cosmic ray intensity with characteristic features that distinguish the effect from daily fluctuations (sharp decrease occurring over hours or days, a recovery rate of 3 – 10 days, possible spike in cosmic flux directly before the decrease). Two physical mechanisms are known to cause the Forbush decrease, the interplanetary shock, if one is generated, and the interplanetary counterpart of the CME, the ejecta. According to Cane [58] there are three distinct cosmic ray responses for Forbush decreases, each generated by the different paths through which the CME passes Earth.

In addition to the two profiles illustrated in Figure 3.6, there is a third, in which only the ejecta hits Earth, in the case that no shock is generated. This causes a short duration, one-step decrease as the ejecta passes Earth. Often times this type of Forbush effect is not large enough to measure in a neutron or muon monitor. The majority of short-term Forbush decreases greater than 4% are of the two-step type, caused by the shock and ejecta. The two-step is visible as a first sudden decrease that temporarily stops, leaving the cosmic ray intensity without fluctuation, which is soon followed by a second decrease (Figure 3.6, path A). The sudden increase observed directly before the sharp decrease in cosmic ray intensity is caused by the arrival of the interplanetary shock, and is referred to as precursory increase. After the passage of the shock and ejecta the cosmic intensity slowly recovers as particles diffuse around the shock [58] over a period of days.

Large Forbush decreases can have magnitudes in the 10-25% range as detected by neutron monitors. Anisotropies in neutron monitor data result in differing magnitudes measured based on the monitor's location. When counting cosmic rates, daily averages give a smaller value than hourly averages. The smaller the interval measured over the

more noticeable the effect. Although the largest Forbush effects can reach 25% magnitude, most FEs are < 10%. According to databases created by IZMIRAN (The Pushkov Institute of Terrestrial Magnetism, Ionosphere and Radio Wave Propagation of the Russian Academy of Sciences), which contains about 5900 Forbush events spanning from July 1957 to December 2006 measured by the world wide neutron monitor network, the majority of FEs are even lower than 2% in magnitude.

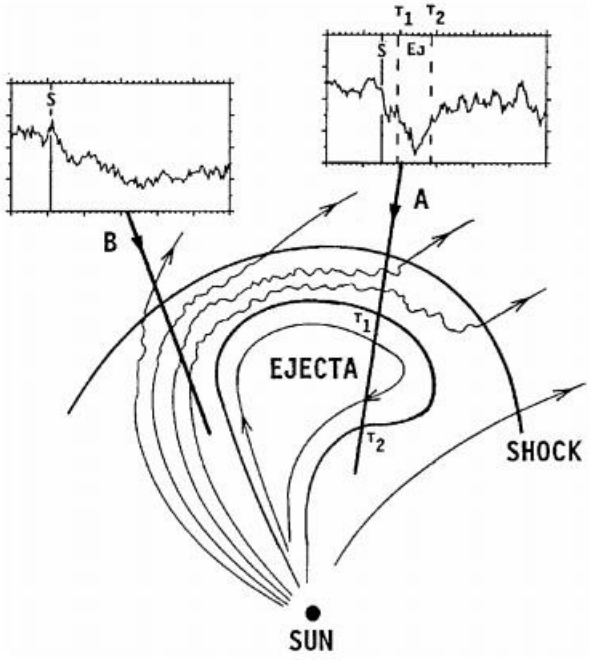

Figure 3.6. The structure of a coronal mass ejection and its associated shock. Solar wind is draped around the ejecta, compressed and heated toward the front. Cosmic ray profiles are modulated in different ways, depending upon the path Earth takes through the CME. In path A the shock and the ejecta contact Earth's magnetic field. S marks the passage of the shock, T1 and T2 mark the start and end time of the ejecta's passage. Path B shows the cosmic ray profile of a shock-only passage [58].

Although neutron monitors are the most commonly used tools in measuring cosmic ray intensity, they do not measure direction and are incapable of robustly

handling the anisotropy of cosmic rays. Muons constitute about 70% of the charged cosmic ray particles at sea level, making muon detectors viable and important instruments for studying the Forbush decrease. Because of the difference in energies of the primary cosmic ray particles that produce muons and neutrons, muon detectors will measure approximately one third of the decrease seen by a neutron monitor, since the higher energy parent particles to muons will not be as strongly affected by magnetic field disturbances [60].

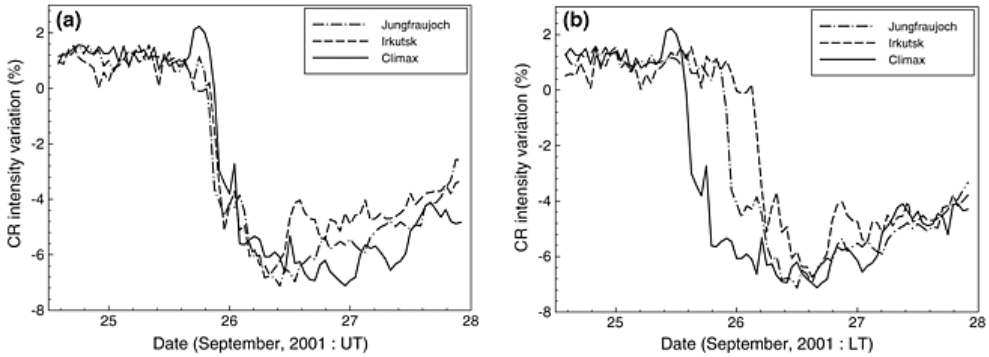

Figure 3.7. Cosmic ray intensity variation profiles of a simultaneous Forbush Decrease event on September 25th 2001 observed at the Jungfraujoch, Irkutsk, and Climax Neutron Monitor stations in (a) universal time and (b) local time. Jungfraujoch is in Switzerland (46.55° N, 7.98° E, Altitude: 3550 m), Irkutsk is in Russia (52.47° N, 104.03° E, Altitude: 433 m), and Climax is in USA (39.37° N, 253.82° E, Altitude: 3400 m) [59].

The ability of Forbush effects to reflect large scale solar processes that are distant from the point of observation make the observations of cosmic ray intensity variations a unique means of studying solar activity and heliospheric processes [57]. The FE's weak correlation to the parameters of interplanetary disturbance and geomagnetic activity indices is valuable, as the FE seems to be affected only by specific features of the solar sources of interplanetary disturbances, providing insight into heliospheric activity in remote space. FE observation has long been important for space weather analyses, and serves as part of the complete picture of heliospheric and solar storms. Old FE data is

valuable when considering the absence of CME and solar wind data from the early periods of FE measurement, allowing us to put together a more complete picture of solar activity when CME and solar wind data is unavailable. The study of FEs can improve our understanding of the sun's behavior over long periods of time, so the accumulation of large amounts of information and data on this effect is important. The NOvA Far Detector is a fully instrumented 14 kiloton scintillation detector with a trigger for cosmic rays. Although designed for the purpose of studying neutrino oscillation (see Chapter 4), it is also a large muon detector. This thesis presents a study of the cosmic ray muon modulation by the Forbush effect as seen in the NOvA data.

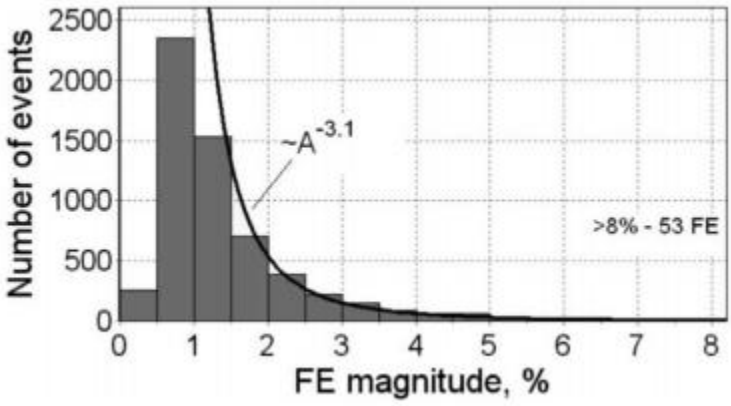

Figure 3.8. The magnitudes of Forbush decreases from 5900 events measured worldwide from July 1957 to December 2006. Ignoring the events with magnitude ≤ 1.5%, the distribution is described by a power law with an index 3.1 ± 0.1, which is larger than the indices of other solar parameters, like the distribution of soft X-ray flare power with an index of 2.19 [57].

CHAPTER 4. THE NOVA EXPERIMENT

4.1 Overview

The NOvA Experiment is a long baseline neutrino experiment designed to make high-precision measurements of the oscillation of muon neutrinos into electron neutrinos in the NuMI (Neutrinos at the Main Injector) beam at Fermilab. It is an appearance experiment, meaning its goal is to find the appearance of electron neutrinos in the near and far detector, and compare the muon neutrino and electron neutrino rates between two detectors. NOvA is the successor to the MINOS experiment, also based at Fermilab, which studies neutrinos with two detectors, a near detector at Fermilab, and a far detector 735 km away in Minnesota. Like Super-Kamiokande before it, MINOS announced data that was consistent with neutrino oscillations in 2006. MINOS's purpose was to see muon neutrinos oscillate into electron neutrinos, to measure the mixing angle θ_{23} and the squared mass differences of neutrinos, $\Delta m^2_{23.}$

NOvA's design is similar to that of MINOS, but with larger detectors and a longer baseline, 810 km compared to 735 km. Its physics goals are to measure the value of the mixing angle θ_{13}, the CP-violating phase δ, and to determine the neutrino mass hierarchy. Recent measurements of θ_{13} by Double Chooz and Daya Bay give nonzero values for the mixing angle. Double Chooz found $\sin^2(2\theta_{13}) = 0.085 \pm 0.051$, and Daya Bay found, at 5.2σ, $\sin^2(2\theta_{13}) = 0.093 \pm 0.016$ (stat) $\pm$ 0.005 (syst). This large value of θ_{13} suggests NOvA will be sensitive to the neutrino mass hierarchy [61].

The oscillation probabilities found for $\nu_\mu \rightarrow \nu_e$ and $\bar{\nu}_\mu \rightarrow \bar{\nu}_e$ will provide a value for the CP violating phase δ. NOvA's sensitivity to the mass hierarchy depends on the value determined for this phase. The mass hierarchy may be determined based on where NOvA's measurements lie, shown in Figure 4.1. Given the experimental values yet to be determined for appearance probabilities of electron neutrinos and antineutrinos, the value of δ_{CP} can be found within experimental error and the hierarchy can be resolved. NOvA's sensitivity to neutrino oscillations depends on the oscillation probability, which is a function of the length traveled by the neutrino, and the energy of the neutrino beam.

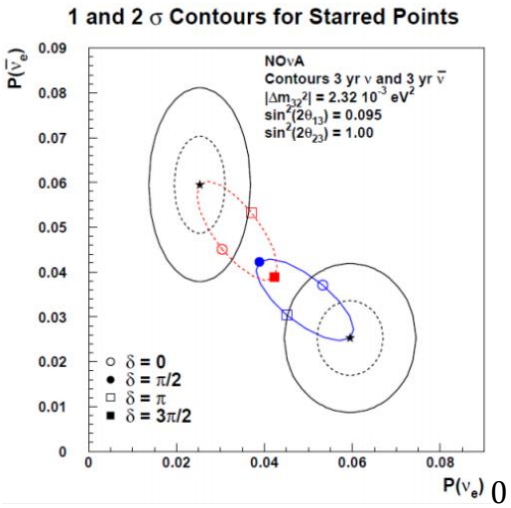

Figure 4.1. Contours surround the starred points where NOvA's measurements will be. The contours in this plot show a case in which δ_{CP}.= 3π/2 (for normal hierarchy, blue line) or π/2. The inner contour is 1σ and the outer contour is 2σ. Knowing the value of θ_{13} from reactor experiments allows NOvA to predict the appearance probabilities that will be seen for a given value of δ_{CP} and the mass hierarchy.

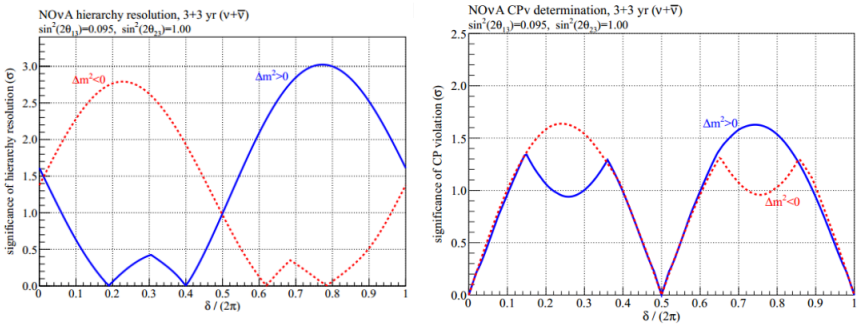

Figure 4.2. NOvA's sensitivity to the mass hierarchy resolution (left), and the significance of the role of CP violation, dependent upon the value of the phase (right).

4.2 The NuMI Beam

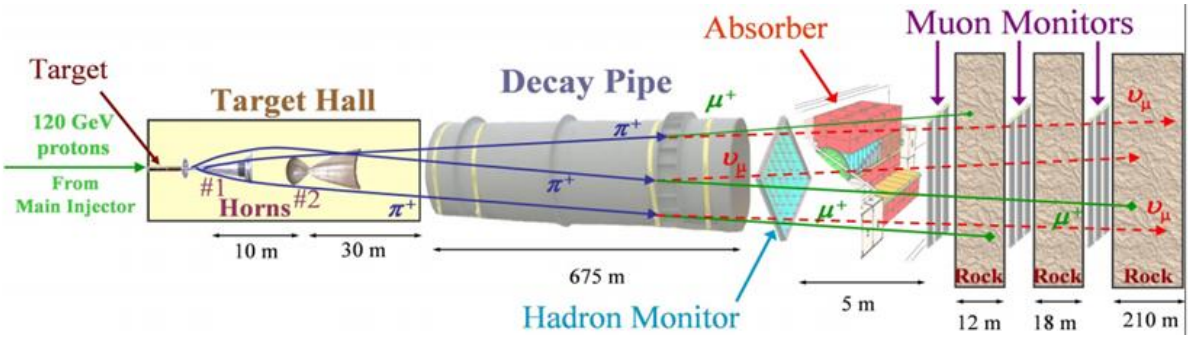

Figure 4.3. The NuMI Beam.

The NuMI beam is the neutrino source for neutrino experiments at Fermilab, including MINOS, MINERvA, ArgoNeuT, and NOvA, and has been in operation since 2005. The beam is created by firing 120 GeV protons from the Main Injector into a carbon target 6.4 mm wide, 15 mm high, and 940 mm long, creating a high flux of pions and kaons that are focused by two magnetic horns along the beam direction, into a 675 m long, 2 m wide decay pipe where the pions and kaons decay into muons and muon neutrinos ($\pi^+ \rightarrow \mu^+ + \nu_\mu$, $K^+ \rightarrow \mu^+ + \nu_\mu$). After the pipe are absorbers and earth that collect undecayed muons, pions, and kaons. Neutrinos or antineutrinos can be selected depending on the horn current (forward horn current for neutrinos, reverse horn current for antineutrinos). The target and horn locations can be reconfigured to provide a neutrino energy spectra from 3 to 15 GeV on axis. Pion decay kinematics provide a relationship between neutrino energy in the lab frame and flux,

$$E_\nu = \frac{0.427\, E_{\pi,K}}{(1 + \gamma^2\theta^2)} \quad (4.1)$$

$$Flux = \left(\frac{2\gamma}{1 + \gamma^2\theta^2}\right)^2 \frac{A}{4\pi r^2} \quad (4.2)$$

where γ is the pion's Lorentz boost and θ is the angle between pion/kaon and neutrino flight direction, or the beam direction and decay axis. The beam initially fired a 10 μs spill every 2.2 seconds, although after the upgrades to the accelerator and NuMI beam the recycle time between spills is 1.67 seconds, and will be ultimately reduced to 1.33 seconds by slip stacking in the recycler, which is a method of merging two sets of a bunched beam into one, which doubles the bunch intensity [62]. The beam delivers 280 – 340 kW of power, but after upgrades will deliver 705 kW for NOvA's purposes.

The NOvA detectors are placed 14 milliradians off-axis of the NuMI beamline, where a narrow band beam exists. Moving off axis the flux decreases but the neutrino energy spectrum tightens. Oscillation probability is maximized at 2.2 GeV at this angle due to increased flux near oscillation maximum. Another benefit of the off-axis design is the reduction of neutral current backgrounds. Figure 4.4 shows the neutrino energies as a function of pion energies for different angles from the beam axis [62].

Almost all pion decays in the NuMI beam yield neutrinos in the 1-3 GeV range. The NDOS is located 6.1 degrees off-axis of the NuMI beam, but is on axis of the Booster neutrino beam, the beam used for the MiniBooNE experiment. Its design is similar to that of the NuMI beam, and its neutrinos have been used in the NDOS for calibration purposes.

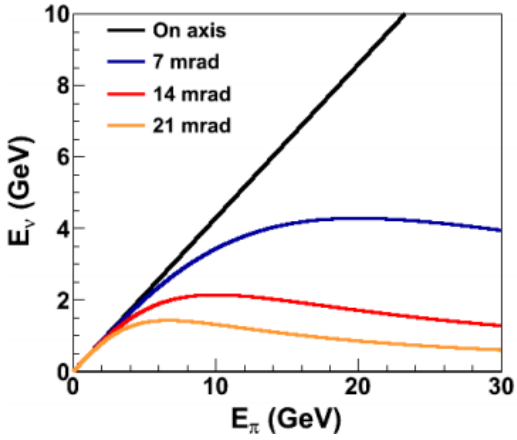

Figure 4.4. Neutrino energy versus pion energy. The red is NOvA's 2 GeV neutrino energy band.

4.3 The NOvA Detectors

Two detectors make up NOvA; an underground Near Detector (ND) at Fermilab, in a cavern adjacent to the MINOS hall, and a Far Detector (FD) at Ash River, Minnesota, 810 km north of Fermilab. Both detectors share a similar design, composed of

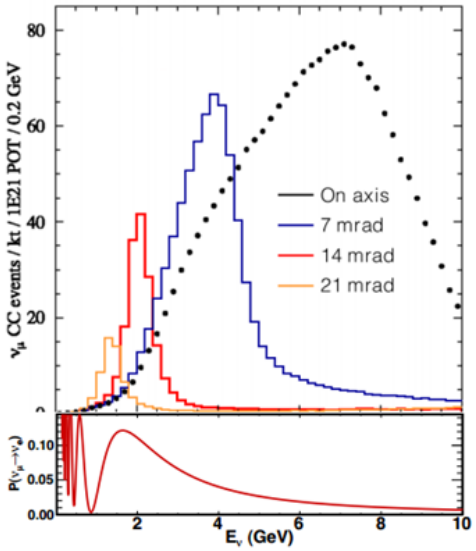

Figure 4.5. Oscillation probabilities for neutrinos up to 10 GeV. For NOvA, located 14 mrad off-axis, oscillation maximum is at 2.2 GeV.

the same parts. A prototype detector, Near Detector on the Surface (NDOS), was built in 2010 to test the performance of the detector design. It was built of the same materials and with the same overall design specifications.

Sixteen-cell PVC extrusions (15% TiO_2) filled with a liquid scintillator composed of mineral oil (Renoil 70-T) (94.91%), pseudocumene (4.98%), PPO (0.110%), bis-MSB (0.00153%), Stadis-425 (0.0010%), and tocepherol (0.0010%) constitute the detector volume. Pseudocumene is the primary scintillant, absorbing light of wavelength 115 nm to 270 nm (peak is approximately 190 nm), and emitting it in the range 275-345 nm (peak is approximately 285 nm). PPO and bis-MSB act as wavelength shifting agents, to shift the pseudocumene's emitted light to higher wavelengths that can be captured by the

wavelength shifting fibers. PPO absorbs light in the 220-345 nm range (peak is approximately 305 nm), emitting it over the range 310-450 nm (peak is approximately 355 nm). This light is further shifted by the bis-MSB, which absorbs light over the 300-390 nm range (peaks around 345 nm), and emits it over the 380-450 nm spectrum (peaking around 415 nm). This is within the range of light that will be captured by the fiber. See Chapter 5 for a detailed discussion of the liquid scintillator. Each cell in the extrusion is 3.9 cm x 6.0 cm x 15.6 m (FD) with up to 92% reflectivity on the inside, due to the titanium dioxide, at 430 nm, which is close to the peak of the scintillator's emission spectrum. There are about 8 reflections on average in each cell before the light is captured by wavelength-shifting fibers.

The FD is composed of approximately 360,000 of these PVC cells and the ND is composed of approximately 16,000 cells. Through each cell is looped a 0.7 mm thick wavelength-shifting (WLS) optical fiber that reads out onto one pixel of a 32-pixel avalanche photo-diode (APD). This fiber collects the light emitted by the scintillator and reflected by the cell walls when a particle passes through. The fiber absorbs light from 350-480 nm, with a peak at 433 nm. Total internal reflection prevents most of the light from 450-650 nm from escaping. Light below 520 nm is attenuated while traveling through the fiber.

When a charged particle travels through a cell of the detector it interacts with the scintillator, producing light, represented by the blue line in Figure 4.6. This light reflects off the inner walls of the cell until one of three things happens: it is absorbed by the WLS fiber, which sends light onto a pixel of a connected APD; it is absorbed by the PVC cell; it is reabsorbed by the scintillator. A MIP passing through a cell undergoes a $dE/dx \approx 12.9$ MeV across the cell.

Two sixteen-cell extrusions are connected into modules, and the modules are put into planes layered in orthogonal views to create horizontal and vertical planes of cells. This allows for the determination of x and y coordinates within the detector. In addition to the 32 cell extrusions, each module, as pictured in Figure 4.6, consists of an end plane, a manifold cover (housing fiber covers, seals, and raceways, through which fibers are

routed to an optical connector) a snout, on top of which is held an electronics box with the front end boards (FEB), and an optical connector, reading out into an APD.

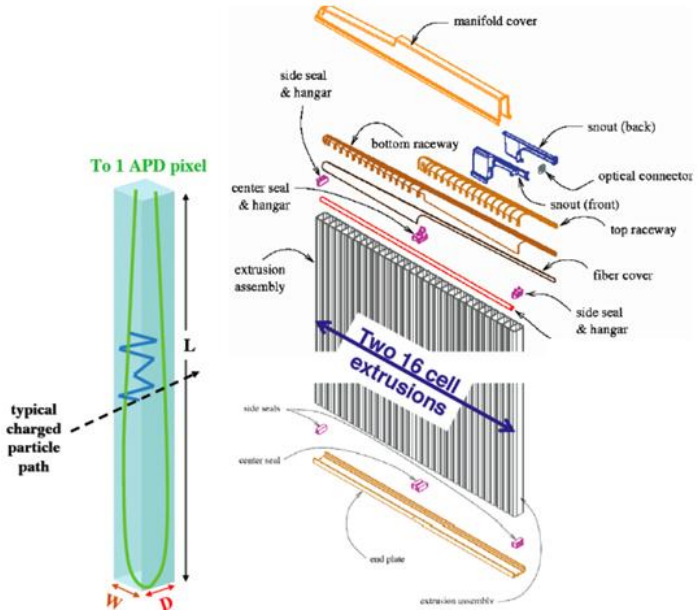

Figure 4.6. A PVC cell with WLS fiber looped through, showing the trajectory of a particle (right), and a 16-cell extrusion with manifold cover and other assembly pieces.

The Near Detector is composed of 196 planes of PVC extrusions, 2.9 m x 4.2 m in size. Ten steel scintillator planes are at the end of the detector as muon catchers. The detector's mass is 220 tons, and the cosmic ray muon rate is approximately 50 Hz, with a 105 m overburden. The neutrino rate is expected to be 30 events per spill, with a 10 μs spill every 1.33 seconds.

The Far Detector is built of 896 planes of PVC extrusions, 15.6 m x 15.6 m in size. Its mass is 14 kTon, with a 65% active volume. The cosmic ray muon rate in the Far Detector is around 200 kHz, with a 2-3 m overburden. The expected neutrino rate is about 1400 ν_e beam events per year. The Far Detector and Near Detector were completed in late 2014, from which point they have been taking data continuously.

The prototype detector, the NDOS, actively collected data starting in October 2010 from the NuMI beam, the Booster beam, and cosmic ray muons. It is a 210 ton detector with 20 tons of fiducial volume. It is 6 blocks of 31 alternating orthogonal planes, with a muon catcher at the end, filled with pseudocumene liquid scintillator. It gets 500 μs wide triggers from the NuMI and Booster beams, plus a 10 Hz pulser.

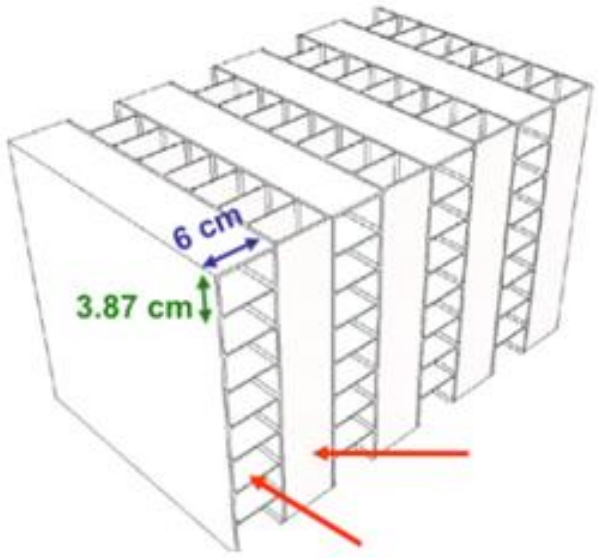

Figure 4.7. Horizontal and vertical planes of cells in the NOvA detector design. The left arrow identifies horizontal cells and the right arrow identifies vertical cells.

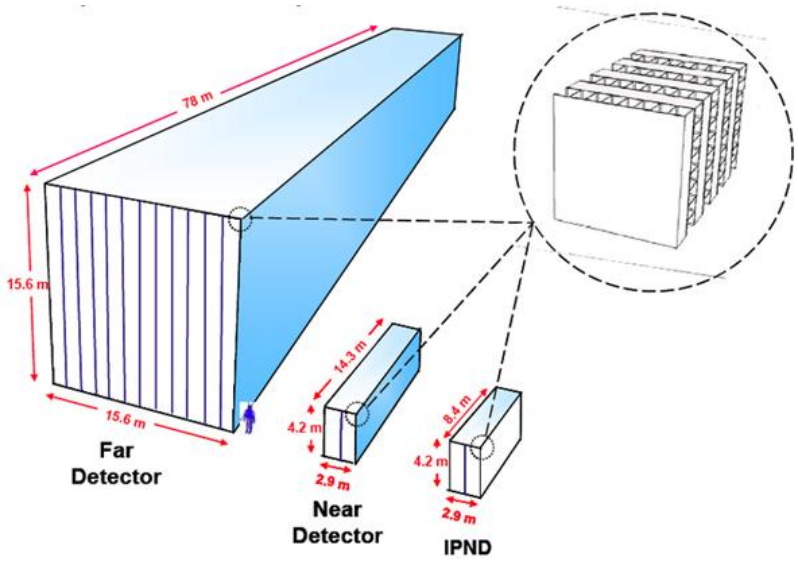

Figure 4.8. The NOvA detectors at scale, including the prototype detector.

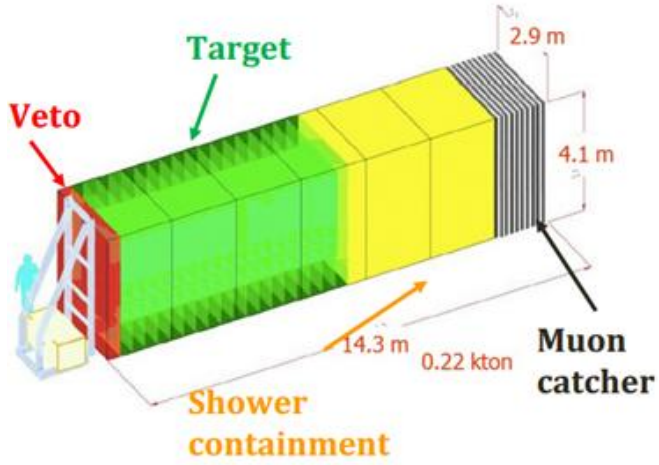

Figure 4.9. The Near Detector on the Surface (NDOS), its veto, target, and shower containment areas colored for identification.

4.4 NOvA Electronics and Data Acquisition

Both ends of the WLS fiber in the cell transmit light to a single pixel of a 32-pixel array avalanche photodiode. These 32 pixels are mapped to the 32 cells in the PVC extrusion module. Light from the fiber crosses an anti-reflection coating at the surface of

the APD and enters a collection region where it generates electron-hole pairs, which propagate to the p-n junction where avalanche multiplication of the electron occurs due to the applied electric field. The mean-free path of the electrons between ionizing collisions (dependent upon the electric field and the temperature) and the electric field provided at the junction determine the multiplication of the current. Because of the current's dependence on temperature, the APDs are operated at -15° C to reduce noise from current generated in the photo-converter region. The APDs have a quantum efficiency of 85% in the 500-550 nm wavelength region, the fiber's emission spectrum. The signal generated by the APD is processed through the front end board (FEB). Each FEB handles the readout of one APD.

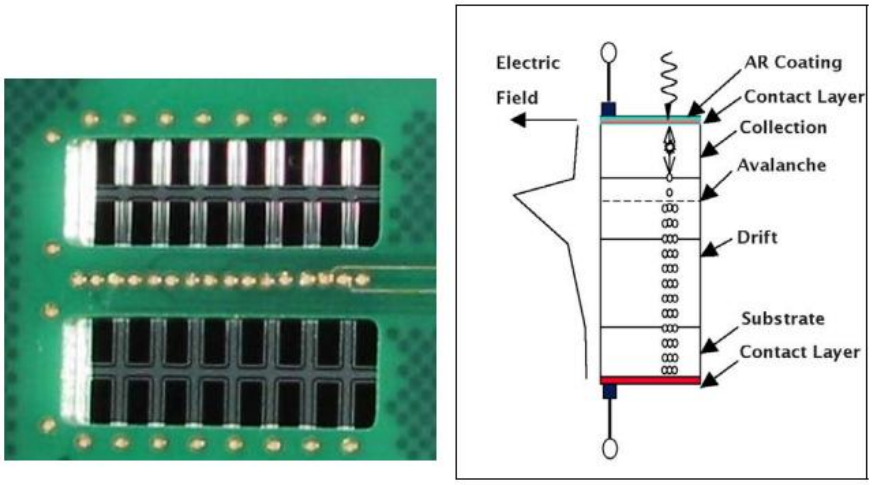

Figure 4.10. Left: The NOvA APD mounted on a carrier board. Right: The APD's structure, showing light passing through the antireflective coating and the contact layer to be absorbed in the collection region. Avalanche multiplication of photoelectrons the occurs in the drift region.

The field programmable gate array (FPGA) on the FEB extracts time and amplitude of the signals received by the APD, using a digital signal processing algorithm. A pulse height and timing edge is found for each signal above a programmable threshold for each channel. The FPGA also removes low frequency noise and increases time resolution. The FEB is equipped with a connector for interfacing with the data

acquisition (DAQ) system. The data concentrator module (DCM) consolidates and concatenates data from 64 FEBs. Data is time stamped and compared to a NuMI timing signal in the DAQ to determine if an event is in or out of spill. Events are sorted into 500 microsecond windows, called time slices, corresponding to a spill. The DCM also monitors the FEBs and provides synchronization of the system. Data is routed from the DCM to buffer nodes where it is stored for further processing.

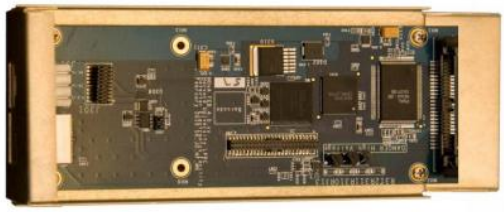

Figure 4.11. NOvA's front end board, the component that processes signals from the APD pixels and extracts time and amplitude data which it transmits to the data concentrator modules.

4.5 Near Detector on the Surface (NDOS)

The construction of the NDOS began in the summer of 2010, and data taking began in October of the same year. The NDOS is a prototype Near Detector at full scale, although the size of the Near Detector was later modified in order to contain all neutrino events. The purpose of the NDOS was to test the design and construction of the NOvA experiment, and to learn about any shortcomings or necessary modifications that would need to be made for the final detectors designed to run for six years, such as hardware issues, structural issues, or commissioning and preparation methods. It is a fully functional detector that allowed data analysis methods to be developed early on, in time for use with the ND and FD. It still collects data but is not of primary importance to NOvA's oscillation search, serving instead as a test detector.

Early on it was found that the manifold covers at the end of the PVC extrusions were cracking either in pressure testing or due to temperature variations in the NDOS

building, requiring repairs and a redesign [64]. Scintillator filling procedures were modified after experience filling the NDOS showed inefficiencies in the original design,, such as the interior of the manifolds requiring a slight vacuum to be pulled on the vent port before filling machines would work. This was changed for the Ash River detector. Some support beams on the outside of the detector prevented proper filling of some extrusions, which was also redesigned for the FD and ND [65].

Figure 4.12. The NDOS. Left: The top of the detector. The DCMs are visible, as well as the FEB and APD electronics boxes. Right: The full detector. [63]

The installation of the electronics boxes, where the FEBs and APDs are housed, was modified for the FD and ND after issues were discovered at the NDOS concerning the installation, function, sealing quality, and efficiency of the APD/TEC (thermoelectric cooler) volume, and the associated exclusion of moisture. It was also necessary to fix grounding issues with the electronics box covers to the FEB boards, and spacing issues for the fiber/APD interface. [66].

4.6 Monte Carlo in NOvA

Simulation of the NuMI beam and the NOvA detectors is important for understanding what the detectors see in order to develop methods for data reconstruction, calibration, and analysis. Monte Carlo algorithms allow us to produce simulated interactions that can be reconstructed and analyzed using code developed in the NOvA framework, then checked against truth information to evaluate the veracity of these analysis tools. In addition to simulating neutrino interactions within the detector, it is of interest to simulate interactions taking place within the rock around the Far and Near detectors to shed light on what effects these surroundings have on recorded data. Simulations are also created to represent differing detector configurations over the course of detector construction and commissioning, to reflect the changing conditions under which data is being gathered. The author held the temporary position in NOvA's Production group responsible for running all simulations mentioned above and detailed below.

The simulation chain is comprised of a few steps, each using a particular Monte Carlo generator or simulation module [67]. All steps of the particle creation and detection process that would occur in real data are simulated: the creation of neutrinos in the NuMI beam, the interaction of these neutrinos in the NOvA detector, the propagation of the products of these interactions within the detector, and the electronics readout. The following is a discussion of these steps.

FLUGG (FLUka with Geant4 Geometry) is a C++ interface between Fluka and Geant4 (GEometry ANd Tracking) which acts as a Fluka extension allowing for the implementation of Geant4's geometry and material assignments, and is used to create neutrino fluxes and kinematic values for each particle in the beam. Fluka performs the first step in the simulation chain, simulating 120 GeV protons scattering on NuMI's carbon target, to be transported through the horn and decay pipe by Geant4 where the pions and kaons decay into the neutrinos used by the GENIE (Generates Events for Neutrino Interaction Experiments) Monte Carlo generator. The geometry and material of these objects are simulated by Geant4. Beamline parameters relating to number of

protons on target, forward or reverse horn current corresponding to neutrino or antineutrino modes, and geometry can be configured in this stage. So too must the "flux window" be evaluated, which corresponds to the orientation of the detector with respect to the beam. This is different for each detector. The file produced in this simulation is a weighted ntuple representing pions and hadrons that decay into neutrinos [68][69].

GENIE handles the interactions of the neutrinos within the detector. It takes the flux files produced by FLUGG and transports the neutrinos through the detector geometry, deciding which particles will interact to produce daughter particles, and how, based on its knowledge of neutrino cross sections. This is the event generation stage, where a list of particles is produced with their 4-momenta and vertex positions to represent an event. GENIE simulates the neutrino interaction with a nucleus in the detector, then the resultant hadronization, and the transportation of these hadrons. The generator records additional information in this stage, such as the initial state of the neutrino and the nucleus upon which it is incident, the kinematic process that occurred in the interaction (quasi-elastic, resonance, deep inelastic scattering, etc.. See Chapter 2), and any inter-nuclear behavior, such as scattering or absorption. This produces a list of target or probe particles (neutrinos), intermediate particles, and final state particles [70].

In the interest of cosmic rays or single particles that are not neutrinos, different generators are used. CRY is the cosmic ray generator and SingleParticle is the Geant4-based particle generator for non-neutrino interactions. These operate similarly to GENIE. The cosmic ray simulation package CORSIKA has been used to simulate cosmic air showers.

Particles produced in the event generation step are then transported through the detector geometry where they undergo physics processes like multiple scattering, energy loss, decay, and annihilation. These processes are carried out by Geant4. A list is created of true energy losses in the sensitive volume of the detector—the liquid scintillator inside the cells. The true energy deposited in each cell is counted as a "hit". These are called FLSHits in NOvA, which stands for Fiber in Liquid Scintillator hits.

Light propagation in the cell and fiber is the next step. PhotonTransport processes the FLSHits, producing photons and propagating them through the cells to turn them into

collections of photoelectrons on the APDs. FLSHits represent a segment of track, each of which has energy depositions associated with it, recorded by PhotonTransport. For each amount of deposited energy along these track segments collected by the fiber, the fiber has half the total energy assigned to propagate in each direction, traveling a distance to the APD which is calculated for both, where attenuation and other scale factors are applied. The number of photons expected at each end of the fiber is the result, and this is labeled the PhotonSignal at the APD [71].

The final stage of the simulation chain is the simulation of the DAQ electronics, managed by the ReadoutSim package. The PhotonSignal produced in the last step of the PhotonTransport simulation is treated as light at the APD. For each PhotonSignal in the channel, there is a pulse seen by the ADC with an associated time, shared by the PhotonSignal. In Monte Carlo, RawDigits are the raw form of "fake data", i.e. the fundamental elements that simulations use to mimic the effects of data, that can then be used to test reconstruction and analysis. RawDigits also exist for raw data [72].

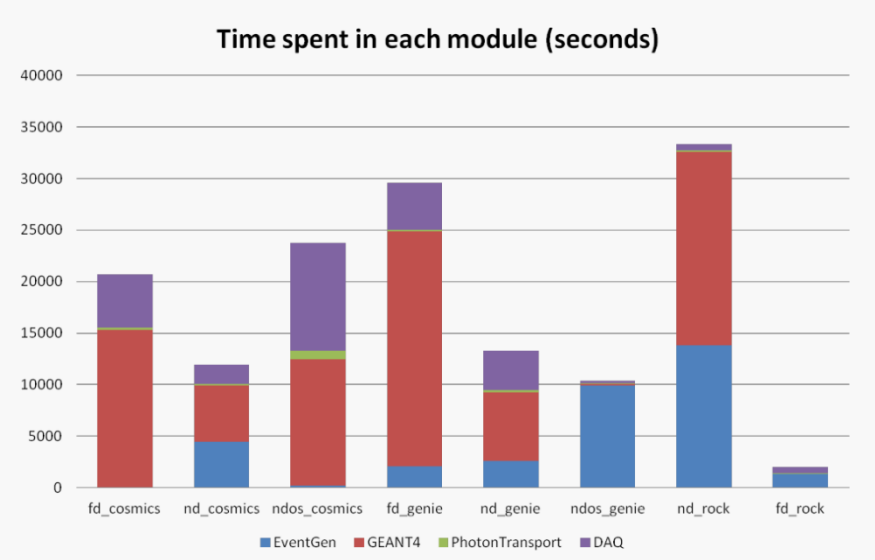

Figure 4.13. Monte Carlo simulation is a resource-expensive process that takes considerable time in each stage. There is a large variance depending on the detectors and particles being simulated, as seen here for a March, 2013 production [73].

4.7 NOvASoft Software

The software used for offline analysis is called NOvASoft, and is written in C++ and built on the ROOT analysis software. This is based in the Fermilab Art event processing framework, a computing framework for data analysis developed by the Fermilab Scientific Computing Division. Art is used to build physics programs using physics algorithms that are provided as plug-in modules, and can be used for high-level software triggers, online data monitoring, calibration, reconstruction, analysis, and simulation. The art framework is shared by all experiments at Fermilab [74].

Events in NOνA are defined as the information associated with a single trigger or spill. In NOνA, events are 500 μs long, and include all the raw data associated with that slice of time, including any information computed from the raw data. These are the smallest units of information art can process. Event IDs are assigned by the DAQ software. This ID is composed of three parts: run, subrun, and event. 64 subruns make up a run, and the number of events in a subrun will vary for each detector, as well as from subrun to subrun. For the Far Detector a typical subrun of cosmic trigger data will have around 2100 events.

Raw digits is the lowest data tier, the form immediately stored by the DAQ. Before raw data can be examined visually or otherwise it must be converted into the ART-ROOT format, allowing the further processing of data, including reconstruction and analysis. The production tool prod_artdaq_job.flc converts raw data into the ART-ROOT format, output as the data tier artdaq.

The artdaq data tier is the input for the calibration and reconstruction stage of processing. This stage consists of various track-finding algorithms, and are followed in the processing chain by particle identification (PID) and calibration. Reconstructed and PID files serve as input to create common analysis files (CAFs), a high level file set containing reconstructed objects. Data sets can be viewed in the event display (EVD), a graphic interface that shows all the hits in the detector associated with each event, for both XZ and YZ views. Reconstructed data will show which of these hits have been

associated with a track, by drawing 2D and 3D tracks from the cell hits. See Figures 6.5 and 6.6 for EVDs of cosmic muon events.

CHAPTER 5. UV CERENKOV REEMISSION IN NOVA'S SCINTILLATOR

5.1 Introduction

The energy scale obtained from NOvA's in situ muon calibration doesn't fix the energy spectrum of electromagnetic showers. NOvA's liquid scintillator (LS) is expected to have an up to 15% uncertainty in energy response at 2 GeV. It is characteristic of liquid scintillators to exhibit a non-linear energy emission caused by Birks' quenching and Cerenkov photon reemission. The effect is noticeable in the tail of an EM shower where dE/dx is high. In an effort to understand this non-linearity studies have been performed on the Cerenkov UV reemission with a UV monochromator and the Birks' quenching with a Compton spectrometer. This analysis details the study of the latter component, the UV Cerenkov reemission. Incorporating the measurements of the NOvA LS properties with NOvA's simulation and calibration will provide a connection between cosmic muon data and expected energy responses in the NOvA detectors. Without an accurate understanding of the scintillator's energy response it is impossible to reconstruct detector events with accurate energies.

One aim of this thesis is the determination of the Cerenkov component of NOvA's LS's non-linear energy response. The chamber used for these measurements is the NOvA cell, different from those in the detector only in length (much shorter to reduce attenuation, and for practicality), and has two fibers looped through it, instead of the single fiber used in NOvA's detectors. This is for increased light output. Instead of reading into an APD as the extrusions in NOvA do, ours feeds into a PMT with a low but serviceable quantum efficiency in the WLS fiber's emission spectrum.

A McPherson model 235 Spectrometer was used in this study. Before studying the scintillator, the photon flux from the lamp as a function of wavelength was studied with a silicon diode. UV light is absorbed and scattered by oxygen, so a turbomolecular pump is used to create a vacuum in the monochromater. The clear filter filters out all

light below approximately 400 nm, and the UV filter filters out higher wavelength light. Using different filters provides different fluxes at different wavelengths.

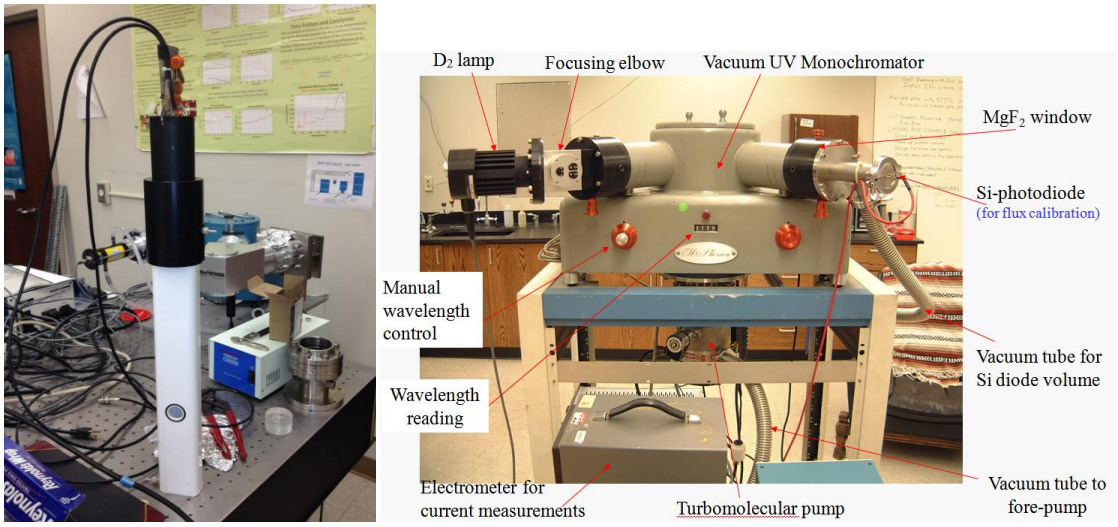

Figure 5.1. Left: The NOvA cell used in this study. It is identical to the NOvA cell in every way besides length, and the hole acting as an entrance for light from the deuterium lamp. Right: The monochromator used in the study. Light from the deuterium lamp enters the monochromator through a .35 mm wide slit, passes through either no filter, a clear light filter, or a UV filter, is reflected off a 150 nm or 300 nm blazed grating, and passes through another .35 mm slit, through a magnesium fluoride window, and enters the cell through the hole pictured on the left.

The silicon diode used to study flux has been calibrated up to approximately 400 nm. A second but similar silicon diode has been calibrated at higher wavelengths. A combination of the electron/photon efficiencies from the two diodes has been used in this study. The calibrated values for the first diode are used for wavelengths below 390 nm, and for higher wavelengths the calibration values for the second diode have been used. The angle at which the light from the deuterium lamp contacts the blazed grating inside the monochromator determines the wavelength of the light that enters the cell. This is

controlled by a knob on the monochromator that turns the plate on which the grating sits to the desired angle with respect to the incident deuterium lamp beam.

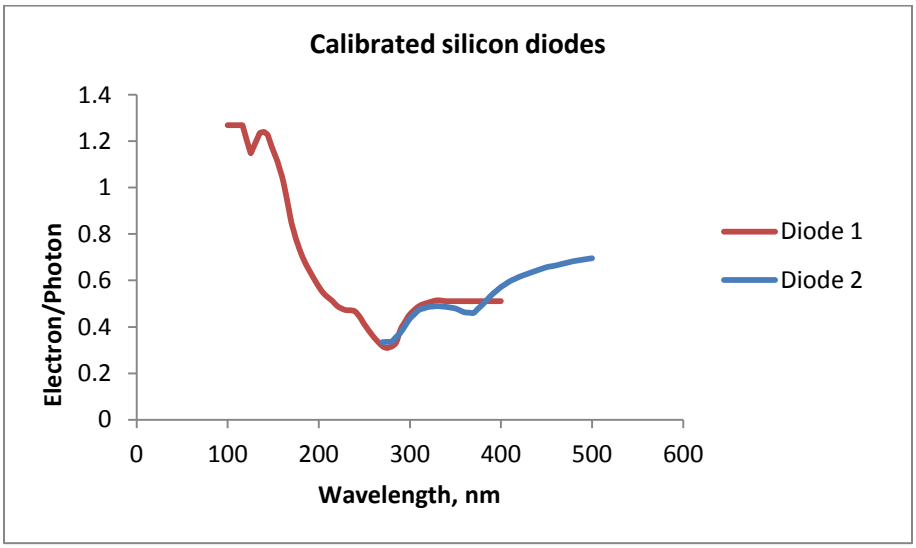

Figure 5.2. Efficiency of electron production per incident photon for calibrated SI diodes, as a function of wavelength.

Flux is measured with a calibrated silicon diode over the range 115 nm to 500 nm. The location of this diode is pictured in Fig 5.1, situated after a magnesium fluoride window that the light passes through on exiting the monochromator. After the flux is measured the diode is replaced with the NOvA cell, with a PMT (Hamamatsu R329-02) connected to its top where the fibers exit. A 1400 volt power supply at negative polarity powers the PMT.

For incident light over the range for which flux was measured, the current generated by the PMT is measured in the same fashion, through an open and closed slit process, finding the current difference between background and signal. When the measurements are finished, the signal current as produced by the PMT's interface with the WLS fibers is known, as is the flux, the QE of the PMT, and the PMT gain. Cerenkov photon emission efficiency and the total light collection/emission efficiency are all that remain to be investigated. These quantities are related in equation 5.1.

$$I^{PMT}_{measured}(\lambda) - I^{PMT}_{background}(\lambda) = n_{\gamma}(\lambda) \times C(\lambda) \times \varepsilon^{light}_{collection} \times QE_{PMT} \times G_{PMT} \times 1.6 \times 10^{-19} \quad (5.1)$$

where $I_{PMT\gamma}(\lambda)$ is the difference in current measured in the PMT, background and signal, $n_{\gamma}(\lambda)$ is the flux of photons exiting the monochromator, measured by the silicon diode, $C(\lambda')$ is the emission efficiency of the Cerenkov photon, and is the primary value of interest. QE_{PMT} is the average quantum efficiency of the PMT over the range 490 – 550 nm (the emission spectrum of the wavelength shifting optical fiber), and G_{PMT} is the PMT's gain. All unknown values are nested within $\varepsilon^{light}_{collection}$ and have to do with the behavior of, and interactions between, the liquid scintillator, the cell walls, and the WLS fibers. Before determining the emission of the Cerenkov photon, this behavior must be understood.

Three different wavelengths act as variables in equation 5.1. The dependence upon three wavelengths is due to the multiple stages of light capture and emission within the cell. The light entering the cell from the monochromator is not the same light the PMT sees to generate the measured current. The incident light from the monochromator interacts with the liquid scintillator, is absorbed over a low range of wavelengths by the primary scintillant, pseudocumene, which then emits light over a spectrum peaking right below 300 nm. This light is shifted by waveshifters in the scintillator, PPO and bis-MSB, which absorb light from 220 nm – 345 nm and 300 nm – 390 nm, respectively. These shifters then re-emit light from 310 nm – 450 nm, and 380 nm – 450 nm, respectively. For the most part, the complicated nature of the absorption and reemission of light within the scintillator by these three components will not be considered. However, the absorption spectra have been taken into consideration when noting that the PMT response corresponds to higher wavelength light from the monochromator. Incident light above 390 nm will not be absorbed by the scintillator, and that which is not absorbed by the cell walls is free to be absorbed by the WLS fibers, which are sensitive to this range. So most

of the signal generated in this range is due not to scintillation, but to the fibers interacting with the incident light directly.

For the purpose of this study, all the light generated in the scintillator, by each scintillant, is treated as one "stage" of emission, of which there are three. These correspond to the variables used in equation 5.1:

λ is the wavelength of incident light from the deuterium lamp exiting the monochromator, which is what the scintillator sees and absorbs, and from 390 nm – 480 nm it is most of what the fiber sees and absorbs. This is the wavelength corresponding to the Cerenkov emission within the scintillator.

λ' is the wavelength of scintillated light emitted by the scintillator, which is most of what the fiber sees and absorbs. Despite the scintillator emitting over a wide range of wavelengths, for this study, λ' was treated as a constant at 430 nm which is the wavelength of peak emission.

λ'' is the wavelength of light emitted by the fiber, and is what generates the current in the PMT. The WLS fiber, too, emits over a spectrum, but λ'' will be treated as a constant at 505 nm, which is the peak of emission from 0.5 m of WLS fiber.

The objective of this measurement is to relate the PMT signal and the flux of incident light of known energy to the behavior of the scintillator.

Total flux from the monochromator is found first by measuring the signal in a silicon diode that is exposed to light over a range of wavelengths (115 nm – 450 nm without a filter and using a 150 nm blazed grating, 200 nm-500 nm with UV and clear filters and using a 300 nm grating).

Gain (G_{PMT}) is 2.7 × 10^5 when operating at -1400 V, and PMT quantum efficiency ($QE_{PMT}(\lambda'')$) is known for the spectrum of light emitted by the fiber. A weighted average is used for the QE, since the PMT sees the entire emission spectrum of the fiber at once, not monochromatic light. There are three configurations for the scans. Three flux scans were conducted with a silicone diode, with no cell or scintillator, followed by three scans of the NOvA cell, filled with scintillator, reading out through

WLS fibers to a PMT, in the same filter-grating configurations. The first scan is with a 150 nm blazed grating with no filter, over the 115-450 nm range. The second is with a 300 nm blazed grating with a UV filter over the 200-500 nm range. The last is with the 300 nm blazed grating and a clear filter, over the 350-500 nm range. An exit slit in the monochromator is closed, and the PMT current is read, constituting background. The exit slit is opened, allowing light into the cell, or in the case of calibration, onto the silicon diode. The current created when the slit is opened is the signal. This is repeated for each wavelength. The difference between background and signal is the PMT response, $I^{PMT}(\lambda$). We find a combined efficiency after making these measurements.

$$C(\lambda) \times \varepsilon_{collection}^{light} = \frac{I^{PMT}(\lambda)}{n_{\gamma}(\lambda) \times G_{PMT} \times QE_{PMT}(\lambda') \times 1.6 \times 10^{-19}} \quad (5.2)$$

$C(\lambda)$ is the reemission efficiency of the UV Cerenkov photon to the scintillation photon as emitted by PPO in the liquid scintillator. This is the primary quantity of interest. This is found through analysis of the data, and the removal of all other light collection efficiencies in order to isolate the Cerenkov factor as the only unknown. There are a few unseen values nested within $\varepsilon_{collection}^{light}$. These include the scintillator's absolute light yield as a function of wavelength, cell reflectivity, the fiber's absorption spectrum and absorption efficiency, as well as the attenuation of the light in the cell and in the fiber. The quantities in equation 5.1 and 5.2 are discussed in the following section, including the methods used to determine these values within reasonable accuracy.

5.2 Quantities of Importance in Determining Cerenkov Reemission Efficiency

The following sections detail the factors contributing to the determination of the Cerenkov reemission efficiency, each of which appears in equations 5.1 and 5.2. How these factors affect this efficiency will be discussed toward the end of section 5.2.6.

5.2.1. Total photon flux from the deuterium lamp as a function of wavelength

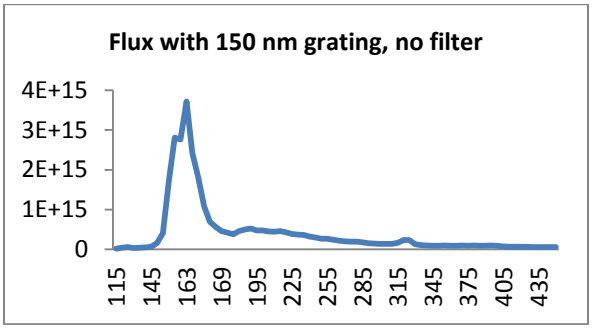

Figure 5.3. Photon flux of incident light from the monochromator, after reflecting off the blazed grating and passing through a filter and MgF_2 window, as measured by Si diode. Photon flux per second vs. wavelength of incident light in nm.

5.2.2. The current created by the PMT through the fiber interface at the top of the cell over the spectrum of incident light

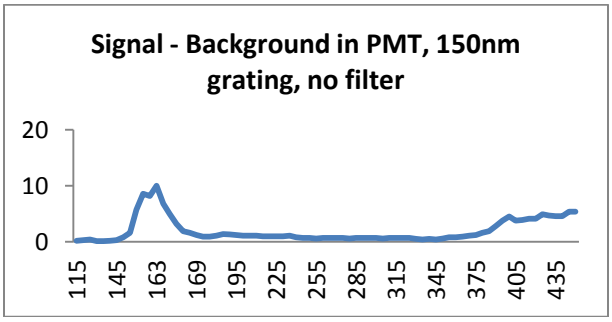

Figure 5.4. Current produced by the PMT (nA) versus the wavelength of incident light from the monochromator in nm.

From 390 nm – 480 nm the dominant contribution to the signal is light that passes straight through the scintillator to be absorbed by the fibers. The scintillator absorbs almost nothing in this region, and therefore can contribute very little to the light absorbed by the fiber. Cell wall reflectivity is also very high in this region, from 73 - 90%, meaning less light is absorbed by the cell walls.

5.2.3. Cell wall reflectivity

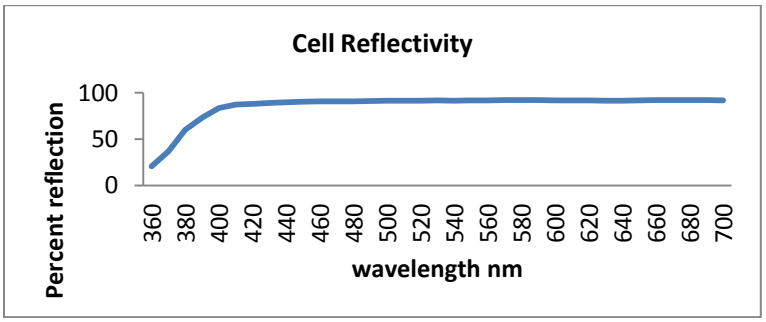

Figure 5.5. Reflectivity of the inner cell walls, as a function of wavelength.

The reflectivity of the cell walls was measured at Fermilab for 360 - 700 nm light. The above plot is an average of 37 extrusions measured in 2011. The reflectance as a function of wavelength of TiO_2 has been measured elsewhere, and suggests a very low reflectance at wavelengths below 350 nm. Because the scntillator's emission spectrum peaks at 430 nm, a weighted average of the emission spectrum with the cell wall reflectivity gives an effective reflectivity for this measurement of 88.05%.

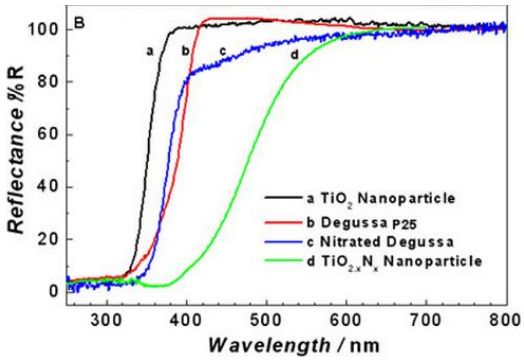

Figure 5.6. Reflectance of TiO_2 at lower wavelengths [75]. The reflectance of NOvA's cells is most similar to the nitrated Degussa, represented by the blue curve.

5.2.4. The PMT's quantum efficiency as a function of wavelength over the fiber's emission spectrum

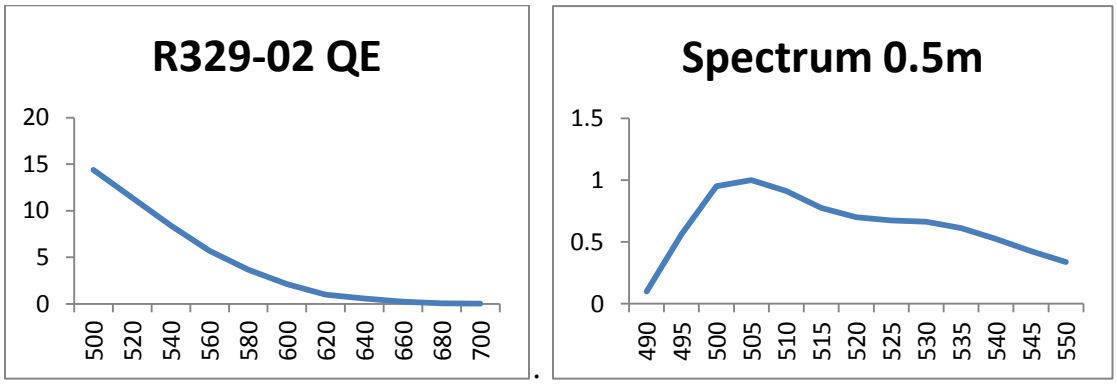

Figure 5.7. Left: PMT QE as a function of wavelength. Right: WLS fiber emission efficiency spectrum as a function of wavelength.

The fiber emission spectrum at 0.5 m (the approximate average distance light travels along the fiber in this measurement) combined with the PMT's wavelength dependent quantum efficiency is used to find an effective quantum efficiency for the PMT; a value of 11.66%. A weighted average is used because the PMT sees the full emission spectrum at once.

5.2.5. The fiber's absorption spectrum

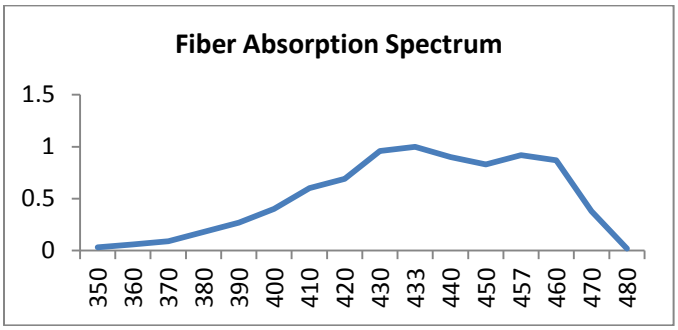

Figure 5.8. WLS fiber absorption spectrum as a function of wavelength in nanometers, normalized to 1.

The collection efficiency of the fibers with two fibers looped through is 19%, according to Monte Carlo simulations. For a single looped fiber the efficiency is 12%. This is a weighted average over the scintillator's emission spectrum and the fiber's absorption spectrum.

Our cell is 20 inches long, and the fiber looped through it is approximately 41 inches, or 1.04 meters in length. The attenuation length of the fiber for 505 nm light, according to studies by Carl Bromberg at Indiana University, is 2.54 meters. In our measurement, light from the monochromator enters the cell at a spot 31.27 cm from the top, where the fibers feed out to the PMT. Assuming the majority of the collected light is collected in this area, and split perfectly in half to travel to both ends of the fiber, 50% of the collected light travels approximately 31.27cm and 50% travels approximately 72.73 cm.

This light is attenuated:

$$P(x) = 0.5 \times e^{-x1/\lambda} + 0.5 \times e^{-x2/\lambda} = 0.81758. \quad (5.3)$$

Approximately 81.76% of the light collected by the fibers reaches the end of the fibers and the PMT. It is assumed light loss from the fibers into the PMT is negligible, considering the optical grease and small separation.

Additional measurements were conducted in which light was passed through the monochromator into the cell without scintillator, with only air and fiber present. These measurements allow for an estimation of a combined efficiency of fiber collection and cell reflection when paired with flux data. The PMT current is divided by $1.602*10^{-19}$ coulomb/electron, the flux for each wavelength as measured by the diode, the PMT's QE, the PMT gain, and the attenuation of the fiber.

Comparing the PMT signal measured with scintillator in the cell and measured again with only air and fiber in the cell (Figure 5.9) shows that this light is not due to scintillation. Since all generated light will be shifted to this spectrum, the combined collection efficiency will be an average of this spectrum weighted with the emission spectrum of the scintillator. And because the majority of light is absorbed directly by the fiber and not scintillated, incident light in this range will be excluded from study.

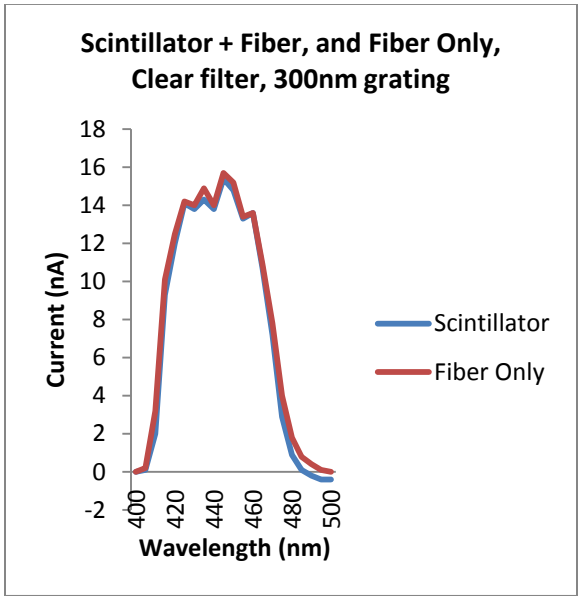

Figure 5.9. The light output from the fibers is almost unchanged with or without scintillator in the cell, for incident light above 400 nm. Scintillator in the cell even seems to diminish fiber absorption in this region.

5.2.6. The absorption and emission spectra of the scintillator's components

Weighing the collection efficiency spectrum of the WLS fiber with the relative emission spectrum of the scintillator gives a weighted average collection efficiency of $1.91*10^{-8}$. This is not significantly different than the estimated value used in the old PhotonTransport package. Because they are the same order of magnitude, the differences in using one or the other should not be too large. In fact, the two numbers represent slightly different quantities. 0.19 represents the fiber's collection efficiency alone. $1.91*10^{-8}$ represents the overall efficiency of light from the monochromator reaching the PMT, which takes into account cell reflectance, and the fiber's attenuation length.

This number relies on measurements in conditions that were not conducive to accuracy, so for the purposes of further calculations, the former value will be used. We can now account for these quantities in our overall efficiency:

$$\varepsilon_2^{light\ collection} = \frac{\varepsilon_{collection}^{light}}{0.8176 \times 0.19} \tag{5.4}$$

where 0.8176 is the approximate light yield at the end of the fibers after attenuation, and 0.19 is the average collection efficiency of the WLS fibers. The PMT's QE is .1166, an average weighted against the fiber's emission spectrum.

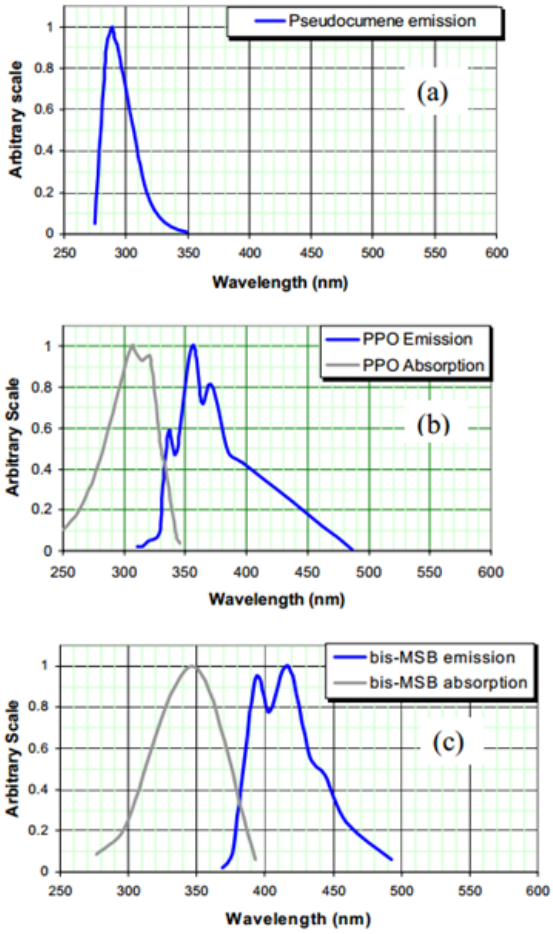

Figure 5.10. The components of the scintillator absorb from 115 nm to approximately 400 nm. Therefore, any incident light above 400 nm captured by the WLS fiber and detected by the PMT is unlikely to be due to scintillation, but is caused by direct absorption by the fibers [62].

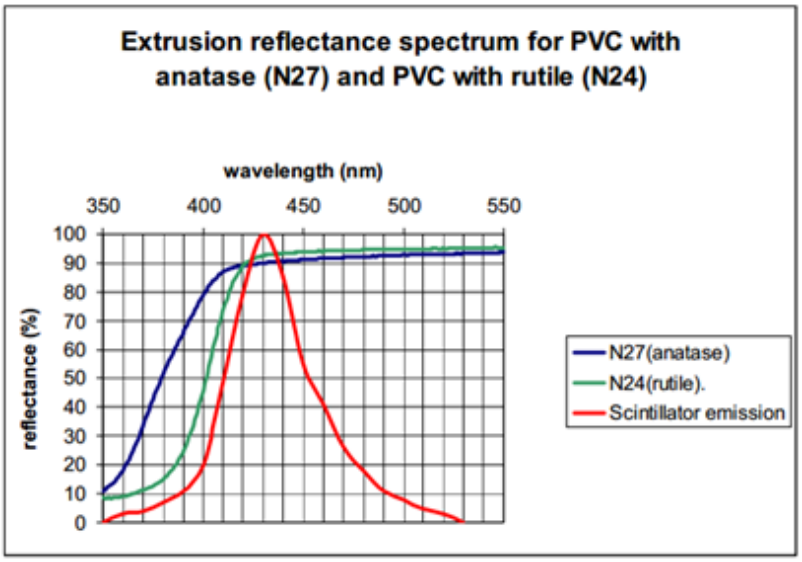

Figure 5.11. The emission spectrum of the scintillator, normalized to 100 [62].

We know the flux of incident photons over the spectrum 115 nm-500 nm, and we know the response seen in the PMT for each wavelength. This information combined with what is known, precisely or imprecisely, about the fibers and scintillator should allow us to reconstruct what is going on inside the cell in order to find the contribution of Cerenkov photon re-emission to the scintillator's energy response. Isolating the known quantities leaves us with a combined efficiency:

$$C(\lambda) \times \varepsilon'_{light\ collection} = \frac{\Delta I^{PMT}(\lambda)}{n_\gamma(\lambda) \times G_{PMT} \times 1.6 \times QE_{PMT} \times 1.6 \times 10^{-19} \times 0.8176 \times 0.19 \times 0.892 \times 0.3613} \quad (5.5)$$

This efficiency represents the product of the Cerenkov factor and the scintillator's absorption and emission efficiency. It is shown in Figure 5.13.

The three constituents of the liquid scintillator have their own absorption and emission spectra. Although we can treat the scintillator's overall emission spectrum as matching that in Figure 5.11, its absolute light yield is not known.

We can find the remaining efficiencies through simple calculations, which will ultimately leave us with only a single unknown quantity: the Cerenkov emission efficiency. Early Monte Carlo simulations indicate that, on average, light will travel 1 meter in the cell before being absorbed by the fibers, and will undergo 8 reflections from the cell walls. After 8 reflections, at 88.05% reflectance, this leaves 36.13% of light to be absorbed by the fibers. Because we are using two fibers instead of one, we double this number to 72.26%. NOvA's scintillator's attenuation length for light around 430 nm is 8.75 nm.

$$P(x) = e^{-1/8.75} = 0.892. \tag{5.6}$$

After traveling one meter, 89.20% of the light will remain. Accounting for reflections, we are left with

$$72.26\% \times 89.20\% = 64.46\% \tag{5.7}$$

of the initial scintillated light available for absorption by the fibers. The absorption efficiency of the WLS fibers is known only within an order of magnitude, but for consistency we will use the value calculated from Monte Carlo, 0.19. The absorption efficiency multiplied by the amount of scintillant light remaining gives 0.122 as the overall efficiency of scintillated light absorbed by the WLS fibers.

After attenuation in the fiber, which leaves 81.76% of the light to be seen by the PMT, the light collection efficiency of the cell + scintillator + fiber apparatus is 0.0997. The combined efficiency in Figure 5.13 becomes the benchmark for the Cerenkov reemission coefficient. The absorption spectrum of PPO determines the amount of light emitted as Cerenkov radiation that is reabsorbed by the scintillator and reemitted at higher wavelengths. The absorption and reemission efficiency of PPO is 1 at ~305 nm [76], so the curve for combined efficiency is set equal to 1 at 305 nm. This curve, when scaled to this value, represents the Cerenkov reemission coefficient. This value can be thought of as the likelihood that a photon at the given wavelength will be absorbed by the scintillator, and the absorption will result in scintillation.

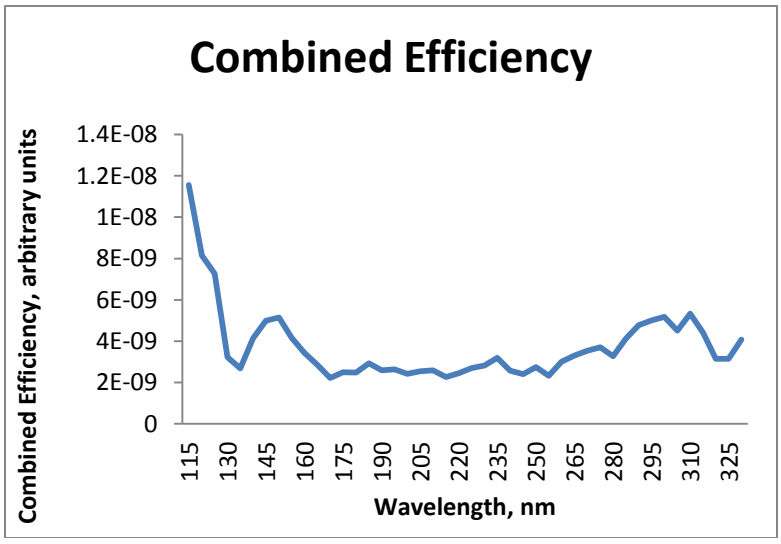

Figure 5.12. The combined emission efficiency, cut off before fiber absorption effects become dominant, around 350 nm.

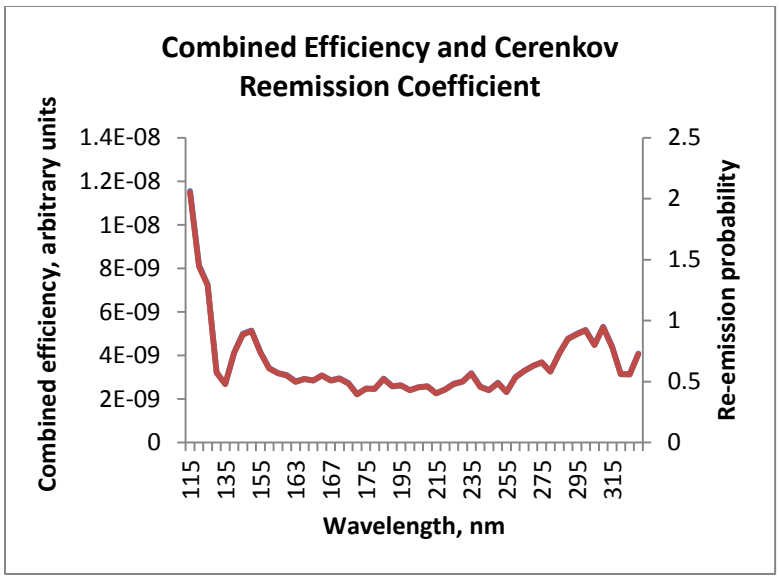

Figure 5.13. The combined efficiency (left axis) and reemission probability (right axis) of the NOvA scintillator.

5.3 Cerenkov Re-emission Analysis

Cerenkov radiation is emitted when a charged particle passes through a medium faster than the phase velocity of light for the medium. It is analogous to a sonic boom, which is caused by an object moving through air faster than the speed of sound in air. A sonic boom results in a cone of shockwaves emanating from the path of the object, and Cerenkov light behaves the same way, radiating outward from the particle's path, creating a cone, the angle of which is determined by the particle's speed and the index of refraction of the medium.

$$\cos\theta_C = \frac{1}{n(\lambda)\,\beta} \tag{5.8}$$

This radiation is emitted over a small frequency range, where $\beta > \frac{1}{n}$. There are two components to the non-linearity of the energy response of NOvA's scintillator, Birks' quenching coefficient and the Cerenkov reemission coefficient. The study of Birks' quenching coefficient is detailed in [77]. The total energy response is a function of both effects,

$$E_{visible} = E_{ionization}(k_B) + E_{Cerenkov} \times C(\lambda) \tag{5.9}$$

Determining the Cerenkov reemission coefficient $C(\lambda)$ requires knowledge of the quantities already discussed, as well as the number of Cerenkov photons emitted as a function of wavelength and particle velocity, given by the relation:

$$\frac{d^2N}{dxd\lambda} = \frac{2\pi\alpha z^2}{\lambda^2}\left(1 - \frac{1}{\beta^2 n^2(\lambda)}\right) \tag{5.10}$$

To understand the Cerenkov reemission measured in NOvA's LS, particularly the relationship between the number of Cerenkov photons produced at each wavelength, it is necessary to know the index of refraction of the LS. Measuring the index of refraction is

difficult, so an estimation has been produced via calculation, as was done for the KamLAND LS based on the mixing of dodecane and benzene.

The refractive index of a mixture of different materials can be approximated with the Lorentz-Lorenz mixing formula, given by equation 5.11. NOvA's scintillator's components are mineral oil (Renoil 70-T) (94.63%), pseudocumene (5.23%), PPO (0.14%), bis-MSB (0.0016%), Stadis-425 (0.0010%), and tocepherol (0.0010%) [78].

The mineral oil is a composite of alkanes, all of which have slightly different refractive indices, scaled by density. The mineral oil's alkane composition is given in Table 5.1. Pseudocumene's index of refraction was estimated using the index of refraction for benzene. Because the indices of refraction were tabulated for photon energy and not wavelength, plotting them against wavelength results in unequal intervals between points. Missing points were filled in using inverse distance weighting interpolation from the known data points for both substances. The reference values for the refractive index of benzene and the alkanes composing the mineral oil were taken from [79] and [80]. The indices of refraction for PPO and bis-MSB were not used due to their very small contribution to the scintillator makeup. The mineral oil was treated as comprising 95% of the scintillator and pseudocumene as comprising 5%.

Lorentz-Lorenz mixing for indices of refraction n_1 and n_2:

$$\frac{n_{12}^2 - 1}{n_{12}^2 + 2} = \varphi_1 \frac{n_1^2 - 1}{n_1^2 + 2} + \varphi_2 \frac{n_2^2 - 1}{n_2^2 + 2} \tag{5.11}$$

where φ_n is the volume fraction [81]. This method was used for the alkanes in the mineral oil, and then for the scintillator as a whole, with both mineral oil and benzene. Lorentz-Lorenz mixing gives an approximation for the scintillator's index of refraction over the spectrum of interest. The number of Cerenkov photons produced in the scintillator can be calculated using equation 5.10.

Equation 5.9 can't be integrated directly due the wavelength dependence of the index of refraction, so numerical integration is performed using Simpson's rule.

$$\int_a^b f(x)dx \approx \frac{b-a}{6}\left[f(a) + 4f\left(\frac{a+b}{2}\right) + f(b)\right]$$

(5.12)

The interval between each measured point on the spectrum is integrated over to give an approximation for the expected number of Cerenkov photons emitted at those wavelengths, in 5 nm intervals. Approximating equation 5.12 with numerical integration takes the form given in equation 5.13,

$$\frac{dN}{dx} = \int_{\lambda 1}^{\lambda 2} \frac{2\pi\alpha z^2}{\lambda^2}\left(1 - \frac{1}{\beta^2 n^2(\lambda)}\right)d\lambda$$

$$= \frac{\lambda_2 - \lambda_1}{6} 2\pi\alpha z^2 \left[\frac{1}{{\lambda_1}^2}\left(1 - \frac{1}{\beta^2 n^2(\lambda_1)}\right)\right.$$

$$\left. + \frac{4}{\left(\frac{\lambda_1 + \lambda_2}{2}\right)^2}\left(1 - \frac{1}{\beta^2 n^2\left(\frac{\lambda_1 + \lambda_2}{2}\right)}\right) + \frac{1}{{\lambda_2}^2}\left(1 - \frac{1}{\beta^2 n^2(\lambda_2)}\right)\right]$$

(5.13)

Integrating this over x, in the range $x_2 - x_1 = N$ cm, gives the number of Cerenkov photons produced as a particle traverses some given length of scintillater, as a function of wavelength. In equation 5.10, β is in fact a function of x, but the x dependence cannot be explicitly expressed mathematically. The Bethe-Bloch equation describes the energy lost by a charged particle during its passage through matter.

$$\frac{-dE}{dx} = Kz^2 \frac{Z}{A}\frac{1}{\beta^2}\left[\frac{1}{2}\ln\frac{2m_e c^2\beta^2\gamma^2 T_{max}}{I^2} - \beta^2 - \frac{\delta}{2}\right]$$

(5.14)

The maximum kinetic energy available to be imparted to a free electron in a collision is given by T_{max}, A is the atomic mass of the medium, K is $4\pi N_A {r_e}^2 m_e c^2$, Z is the atomic number of the medium, I is the mean excitation energy, m_e is the electron mass, and δ is the density effect correction to ionization energy loss. Using the modified form of the Bethe equation for an electron, the energy loss for relativistic electrons allows the change

in β as the electron travels one centimeter to be evaluated, which, it turns out is small enough to treat as a negligible quantity that won't affect the integration of equation 5.13.

Table 5.1. NOvA's mineral oil composition by percentage of alkane present.

Carbon number	% of mineral oil mixture
10	0
11	0.1
12	0.1
13	0.1
14	0.1
15	0.5
16	3.9
17	13.2
18	24.7
19	27.8
20	19.0
21	7.2
22	2.3
23	0.5
24	0.1
25	0.1
26	0.1
27	0.1
28	0.1
29	0.1
30	0

The values of β before and after the traversal of one centimeter are compared, and the percent change is calculated by $(\beta_i - \beta_f)/\beta_i$. For kinetic energy above 0.5 MeV this effect is much less than 10%, and above 1.25 MeV the effect is less than 1%.

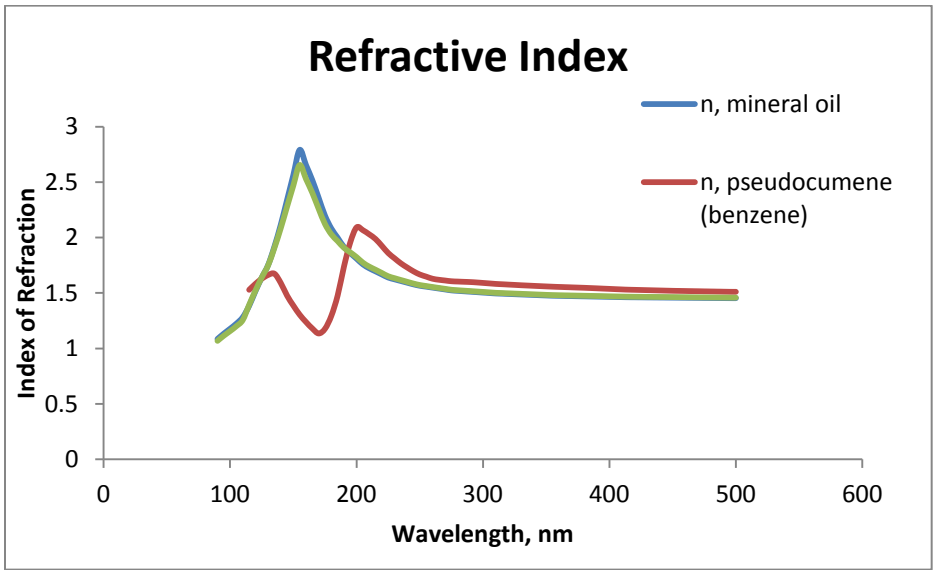

Figure 5.14. The mineral oil's index of refraction dominates the total index of refraction of the scintillator.

5.4 Results

This section presents the results of the Cerenkov reemission analysis after all efficiencies have been approximated. Figure 5.15 shows the results of integrating Equation 5.10 to find the number of Cerenkov photons produced in the scintillator by electrons of given energies, until the electron is stopped. This plot shows the relative numbers of photons produced at each wavelength, where UV dominates the overall contribution to the light produced.

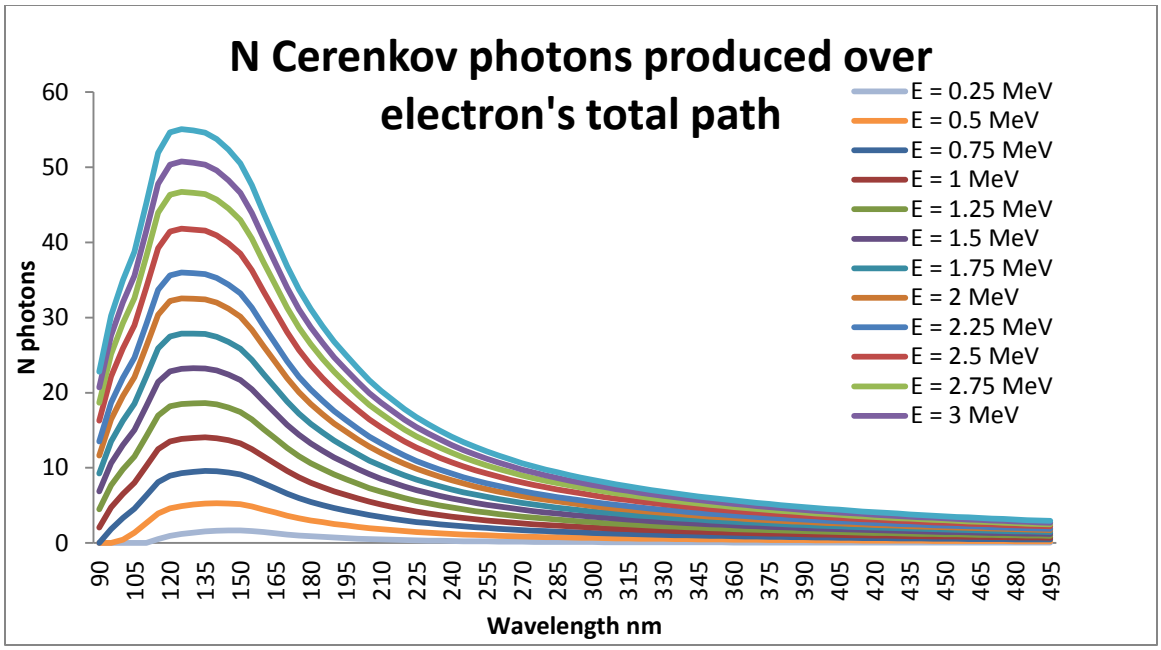

Figure 5.15. A plot of the number of Cerenkov photons produced at each wavelength by the traversal of a relativistic electron through NOvA's scintillator. Values were obtained by numerically integrating equation 5.10 via the method in 5.13.

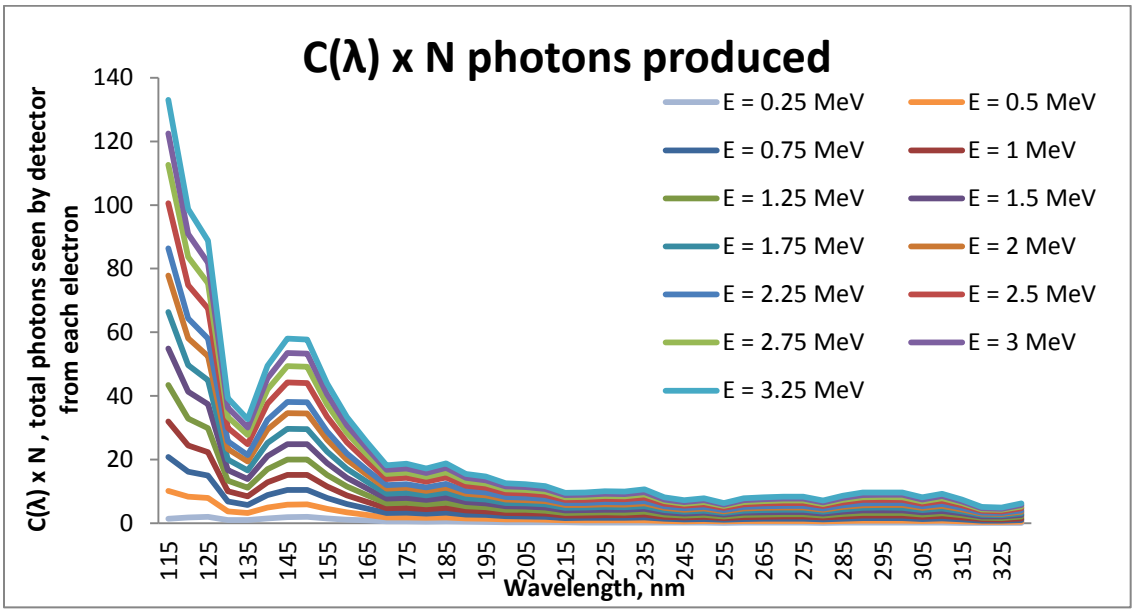

Figure 5.16. This curve is the product of the number of Cerenkov photons initially produced by the traversal of a relativistic particle through NOvA's scintillator

multiplied by the reemission coefficient. Therefore it represents the total Cerenkov photons of a given wavelength emitted by the NOvA scintillator.

Multiplying the values in Figure 5.15 by the Cerenkov reemission coefficient from Figure 5.13 gives the total number of Cerenkov photons at each wavelength that will be produced in the NOvA scintillator by an electron traversing the scintillator. This curve is given in Figure 5.16. Integrating the area under the curves corresponding to each energy gives the total number of detectable Cerenkov photons produced by an electron passing through NOvA's scintillator, as a function of energy. These values ($N_{produced}$) are plotted in Figure 5.17. Multiplying this value by the total efficiency of the NOvA setup gives the number of Cerenkov photons seen. The total number of these Cerenkov photons observed is given by

$$N_{observed} = N_{produced} \times \varepsilon_{attenuation} \times \varepsilon_{APD\ efficiency} \times \varepsilon_{fiber\ absorption\ efficiency} \quad (5.15)$$

where $N_{produced}$ is the number of Cerenkov photons produced by the charged particle per centimeter, $\varepsilon_{attenuation}$ is the amount of light left after attenuation in the WLS fiber (through 7.75 meters, one half the length of a cell, = 4.7%), $\varepsilon_{APDefficiency}$ is the percentage of photons seen by the APD (85%), and $\varepsilon_{fiberabsorption}$ is the percentage of incident light the WLS fiber will absorb (12%). This value makes up the Cerenkov portion of equation 5.9, and represents the contribution of Cerenkov photon reemission to the non-linear energy response of NOvA's liquid scintillator. When the Compton spectrometer experiment is finished the results from both experiments will be used in a model to determine the Cerenkov reemission contribution and the Birks' quenching coefficient, which are necessary for NOvA's proper energy calibration. At the time of writing this thesis the Compton spectrometer experiment is unfinished.

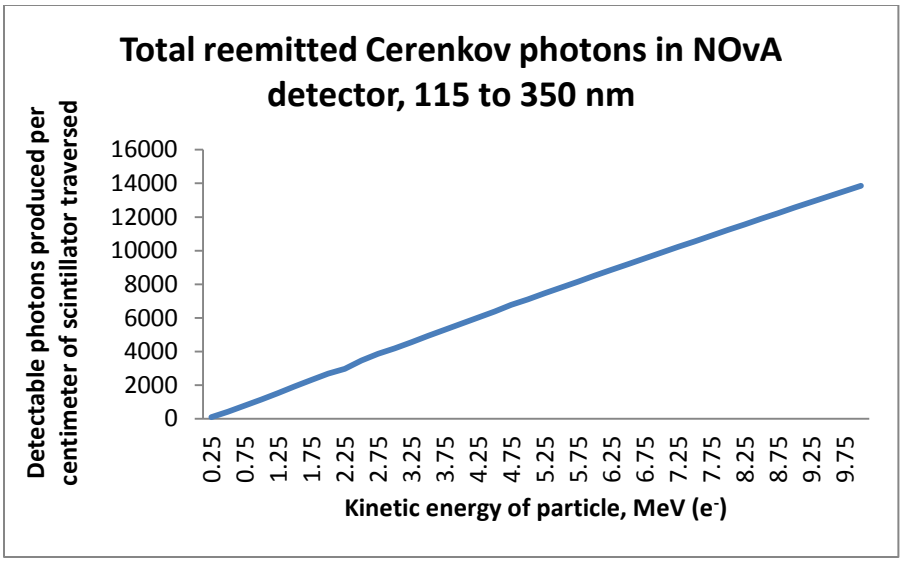

Figure 5.17. The total number of Cerenkov photons produced in NOvA's scintillator by an incident electron of the given kinetic energy.

The number of Cerenkov photons produced by an electron of energy E will follow the relationship shown in Figure 5.17. Equation 5.9 will give the final correction to be used in the Monte Carlo,

$$E_{visible} = E_{ionization}(k_B) + E_{Cerenkov} \times C(\lambda)$$

with C(λ), the reemission probability, taking on the values plotted in Figure 5.13 as a function of wavelength. Figure 5.16 shows the Cerenkov photons produced at each wavelength multiplied by the reemission probability. NOvA's scintillator's light yield is currently unknown, but it is reasonable to estimate it is approximately that of KamLAND's scintillator, which has 70% the efficiency of anthracene. Anthracene produces 1 photon for every 64 eV. If we estimate that NOvA's LS produces 1 photon per 91 eV, we will see approximately 10,989 photons for 1 MeV. The Cerenkov reemission produces 1155 photons for a 1 MeV electron, creating a 10.5% additional energy output. The ratio of photons produced by Cerenkov reemission to initial scintillation photons is a nonlinear relationship at lower energies, as shown in Figure 5.18. This represents the non-linear energy response contribution of Cerenkov

reemission, and it will be combined with the results from the Compton spectrometer for Birks' quenching to determine the full energy correction required in NOvA's scintillator.

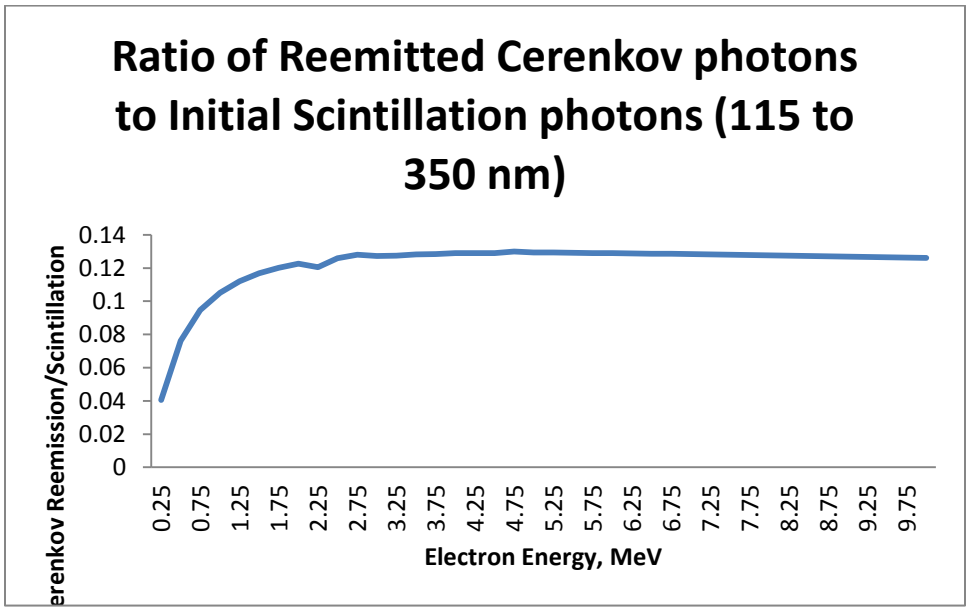

Figure 5.18. The curve represents the ratio of Cerenkov photons reemitted by the scintillator to the photons emitted in initial scintillation. For low energies (< 3 MeV) the relationship is non-linear.

The reemission of Cerenkov photons in the visible spectrum cannot be examined with this study, as no information can be obtained about the scintillator's response to Cerenkov photons in the range above 350 nm due to the WLS fiber's absorption spectrum beginning at 350 nm. This means the signal in the PMT seen for incident light at 350 nm and above, from the monochromator, is due to the emission of the fibers and not the scintillator, which is mostly transparent in this range.

If it is assumed that the refractive index of the scintillator remains constant above 350 nm and the Cerenkov reemission coefficient is approximately constant, the number of total Cerenkov photons reemitted over the spectrum frorm 115 nm to 480 nm is given in Figure 5.19.

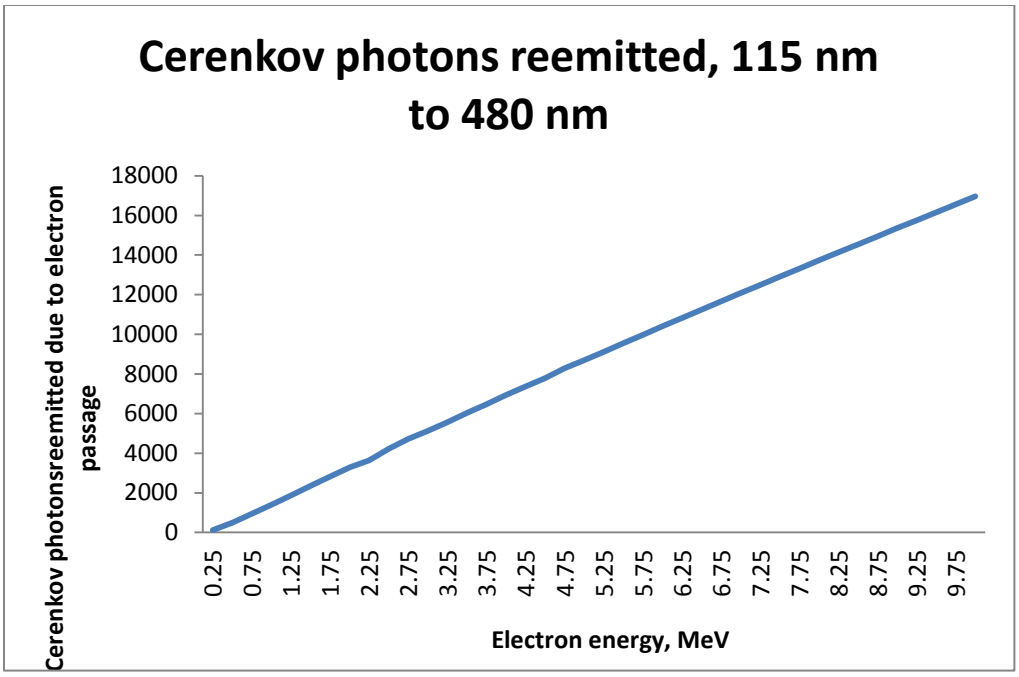

Figure 5.19. The total number of Cerenkov photons reemitted in NOvA's scintillator over the spectrum from 115 nm to 480 nm.

The ratio presented in Figure 5.18 can also be extended to higher wavelengths, up to 480 nm, resulting in an increase in the total Cerenkov reemission effect. Now the correction to light yield is approximately 15% at higher energies, but still nonlinear at lower energies.

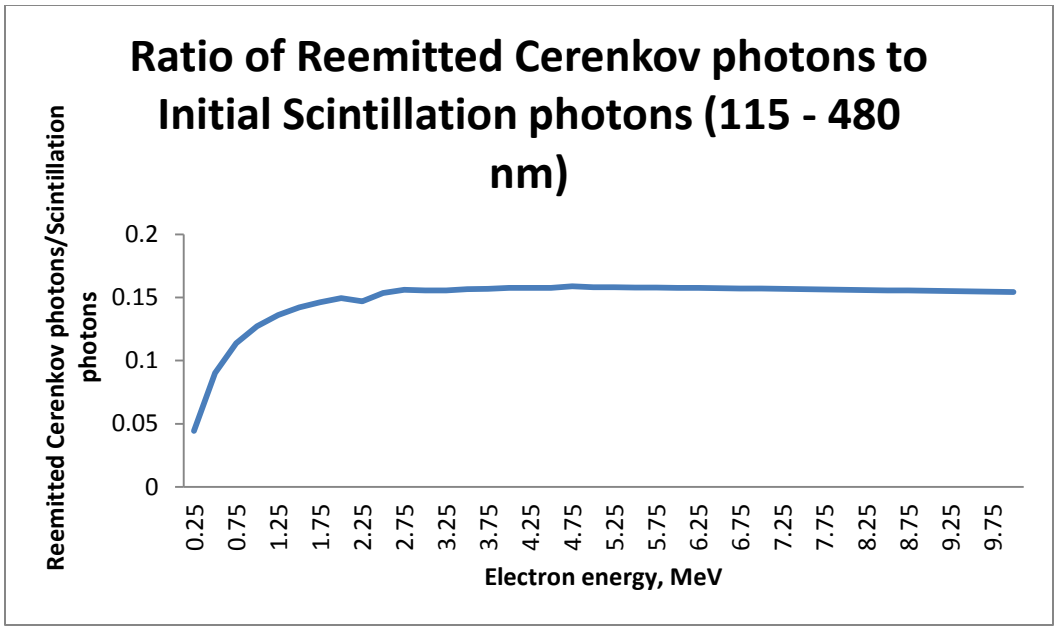

Figure 5.20. The curve represents the ratio of Cerenkov photons reemitted by the scintillator to the photons emitted in initial scintillation. This curve is for considerations extending to higher wavelengths, covering the absorption spectrum of the WLS fibers. For low energies (< 3 MeV) the relationship is non-linear.

CHAPTER 6. FORBUSH EFFECT ANALYSIS

6.1 Introduction

In addition to the determination of the Cerenkov component of the NOνA liquid scintillator's non-linear energy response detailed in the previous chapter, an aim of this thesis is to provide a measurement of the Forbush decrease from data taken at NOνA's Far Detector, in Ash River, MN. Unlike the Near Detector which lies 350 feet underground, the Far Detector is on the surface and detects cosmic ray muons, covering an area of 900 square meters, or 9700 square feet, making it one of the Earth's largest continuous muon detectors. See Chapter 4 for more information on the detectors. Data for this analysis was taken by the cosmic pulser, with approximately two thousand one hundred 500 microsecond events per subrun. There are 64 subruns per run, although some subruns (4-10 per run, on average) fail reconstruction and analysis and are rejected.

6.2 Data Selection

The hypothesis of this thesis is that a full halo event CME from the sun will cause a significant and observable decrease in cosmic muon flux when it hits Earth. This is the Forbush Effect, which was discussed in Chapter 3. Exact predictions as to which solar events will modulate cosmic ray intensity are impossible. In the interest of having a large and complete dataset corresponding to a fully instrumented and active detector, only data taken after the NOνA Far Detector's completion has been considered. This includes data from October 2014 forward. The fully instrumented Far Detector is one of the largest single, continuous muon detectors on Earth, making it highly capable of measuring consistent cosmic ray flux in a specific area with no assumptions or interpolations required to fill in gaps, and still small enough that cosmic flux at ground level can be

treated as unvarying across its surface area. With data-taking running non-stop except for maintenance or tests, the NOνA data spans a continuous period, with very little interruption. This feature is important for studying fluxes that may change dramatically over brief intervals.

A Forbush decrease is detected two to three days after a CME occurs, depending on solar wind speed, providing a clear window of opportunity to investigate associated effects.

NASA and NOAA archives provide extensive CME and solar flare data, including data on full-halo or partial-halo events in which Earth could have been hit by ejections from the sun. This data was studied over a period spanning from October 2014 to May 2015. Long-wave and short-wave imaging from the Solar Dynamics Observatory (SDO) is available for the viewing of solar activity, as well as X-ray, proton, and electron flux data from the Geostationary Operational Environmental Satellite (GOES) spacecrafts, and various forms of data and imaging from the Solar and Heliospheric Observatory (SOHO). Much of the data and images collected by these observatories were available through NASA and NOAA, and enabled the study of a link between solar activity and cosmic ray flux at Earth.

The current solar cycle is solar cycle 24, an 11 year cycle of increasing and then decreasing solar flare activity. The activity of a solar cycle is determined by a count of sunspot number, since sunspots indicate regions of flare activity. Cycle 24 is a low-activity cycle compared to those that came before (30% lower than cycle 23), but the solar flare activity of this cycle peaked in 2014 and 2015, making 2015 a good period in which to study cosmic rates. NASA and NOAA solar data from March showed relatively high solar activity in flares and CMEs, indicating a sensible starting point to study cosmic rate variations. The cuts implemented for this study are detailed in section 6.3, the measurement of cosmic ray flux in March is discussed in section 6.4, and the results of the measurements and analysis are discussed in section 6.5.

6.3 Cuts

To insure consistency and a high quality of data used for the analysis the following selection criteria were implemented for the reconstructed cosmic muons. Every run and subrun used in the analysis passed the 'good runs' criteria established by NOvA, indicating the data was taken during a stable period in which no known problems occurred within the detector or DAQ that would result in inaccurate or incomplete data.

The minimum signal allowed is 22 photo electrons per cell. If a cell hit is below this threshold it is added to a noise cluster and not considered part of the track. If it meets or surpasses this threshold the hit is considered part of a track. A track length cut was implemented to limit the minimum acceptable track length to 50 cm. However, the following two criteria removed many tracks that were shorter than 1500 cm, by virtue of the detector geometry:

1. The maximum track vertex distance from the edge of the detector was limited to 10 cm, and the same limit was used for the track endpoint. So all tracks begin and end within 10 cm of the edge of the detector, leaving mostly very long tracks, except for those that entered and exited near corners of the detector.
2. The angle of incidence was strictly limited to $\cos\theta_y \leq -0.95$ to include mostly vertical tracks.

With these two criteria, the majority of reconstructed tracks that passed the cuts were at least 1500 cm in length, perhaps making the minimum track length cut irrelevant. But that cut was left in, to insure no short tracks were accepted, which could still be possible with the above two cuts.

To remove events that have an electromagnetic shower-like nature the maximum number of cells per plane that are allowed to be associated with a track are 6. More than 6 cells per plane associated with one track are rejected.

Between the two views of the Event Display (Figures 6.5 and 6.6) in which particle events are pictured (ZX, ZY) the maximum plane asymmetry allowed between the number of planes in each view is 0.1. This value is implemented in the following

way. A track is rejected if the difference in the total number of X planes and Y planes is greater than 0.1 multiplied by the total number of X planes plus Y planes. So, if

$$\left|N_{x\ planes} - N_{y\ planes}\right| > 0.1 \times \left(N_{x\ planes} + N_{y\ planes}\right) \quad (6.1)$$

the track is rejected. This is necessary because with hit planes in one view that are not visible in the other you lack information on the exact length of the track, so it is impossible to know if length and containment are correct. The largest allowed difference in the plane numbers of the endpoints of the track is 3 planes, requiring the XZ and YZ views to match sufficiently well for a track to be accepted.

Step size indicates the step distance between cell hits counted in a reconstructed track. For each reconstructed track a median of the step size distribution for the track is calculated. If the largest step is three times the median or larger then it is far outside the distribution and the track is considered poorly reconstructed. Large changes in step size within a track indicate bad reconstruction, and these tracks are removed. These selection criteria are not implemented until after the reconstruction phase of data processing, which is detailed in the next section. All tracks that pass these cuts are used for analysis.

6.4 Track Reconstruction and Analysis

The NOνA Production group is largely responsible for the processing of data and Monte Carlo for use by the collaboration's experimentalists. This entails converting raw data in the form of RawDigits into the artdaq data format, which is the .root form of data that is then calibrated and reconstructed by the same group to later be analyzed or, in the case of Monte Carlo, generated for use by the simulation, calibration, alignment, and analysis groups. The data hierarchy is detailed in section 4.7. The Production group's efforts are prioritized by the urgency of the data they process, which means most of their production is focused on neutrino data for the oscillation analyses. Therefore, the cosmic muon data needed for this study had not been processed beyond the raw digit stage. I processed the data from artdaq through the reconstruction and analysis stages

independently, using production and reconstruction tools from the NOvASoft architecture and art framework modified for my own purposes.

I modified the cosmic reconstruction tool used by the Production group, a .fcl file that chains together the calibration and reconstruction algorithms for cosmic tracks. I added an analysis stage to the end of the output path to perform calibration, reconstruction, as well as a basic analysis together in a single executable. 187 runs were used in the analysis, spanning the period from March 1st to March 31st, 2015. Each run is comprised of 64 subruns, and each subrun is comprised of approximately 2100 events. There is one raw data file corresponding to each subrun. This is over 11 TB of data and almost 12,000 individual data files, meaning over 24,000,000 events were processed, which requires thousands of hours of CPU time. Data was processed on Fermilab's scientific computing grid, which is described in NOvA's Offline computing wiki as:

"a large cluster of worker nodes controlled by a submission (or head) node. Each worker node is a CPU, each with a local disk for temporary file storage. The submission node maintains a queue of jobs which need to be run and distributes those jobs to worker nodes based on a user priority system. Submitting jobs to the grid means adding jobs to the queue. Jobs must be configured to run a specific executable along with any required arguments." [82]

Jobs, which are the running of some type of software on some type of data or Monte Carlo file for analysis or other purposes, are submitted to the grid through the SAM system, a means of handling data by their metadata. SAM is also succinctly described in the wiki:

"Sequential Access Metadata (SAM) is a data handling solution developed by Fermilab's Scientific Computing Division (SCD) to efficiently deliver tape-archived files. The tape archive is supplemented by the large dCache disk array which stores recently used files. Technically, SAM is just a database of file names, locations and metadata; in practice, it's the bit of machinery that ties everything together. One of the key features of SAM is that it obfuscates users from nitty gritty file details like names and locations in favor of higher level information cataloged by the file metadata. Metadata classifies files

based on their key features, like processing tier, run number, trigger stream, generator type, etc."[82]

Using job submission tools developed in part by Fermilab's Scientific Computing Division and in part by NOνA physicists, customizable projects can be submitted to the grid for processing, allowing multiple jobs to be handled automatically without any further user input. Due to the large CPU time required for calibration, reconstruction, and analysis, grid computing is the only viable means of handling large amounts of data. All computing for the reconstruction and analysis in this thesis was done on Fermilab's computing grid.

The first step in processing data is calibration with the CalHit module, which takes as input hit-level data in the form of raw digits produced by the DAQ. Raw hits are converted to a list of calibrated cell hits after they are looped over with NOνA's Calibrator, applying fitted ADC values and time to each hit. The cosmic muon data, upon being submitted to the grid for processing, first undergoes calibration.

Calibrated cell hits, or simply CellHits, as they're designated in the software, are the input for the Cosmic Slicer, the initial stage of track reconstruction. The Slicer groups neighboring hits together in 4 dimensions, according to their proximity in time and location within the detector. These hits are collected into "clusters" or "slices", of which every event may have many. Each slice or cluster then, ideally, corresponds to an individual interaction with a minimal number of noise hits. Noise slices are produced, containing hits that do not appear to correspond to any particle activity in the detector. Clusters produced by Slicer serve as the inputs to the rest of the reconstruction tools.

Reconstructing cosmic muon tracks is simpler than reconstructing tracks associated with neutrino interactions, because of their straightness, length, lack of shower behavior, and predictable energy deposition. The CosmicTrack module in the TrackFit package of track-finding algorithms takes the 3D clusters from Slicer and applies a straight-line fit to hits within a slice, using both XZ and YZ views. This line is made by minimizing the squared perpendicular distance between the hits in the slice and the straight line passing through them. Hits that are more than 10 cm from the line are dropped as noise hits. The output from this algorithm is 2D and 3D tracks, with start and

end points in each 2D view matched to create 3D tracks. Points downstream in Z are assumed to be endpoints. These points are swapped if timing indicates the track instead goes upstream, by comparing the times at each end of the track. Following this procedure, the cuts discussed in section 6.3 are implemented.

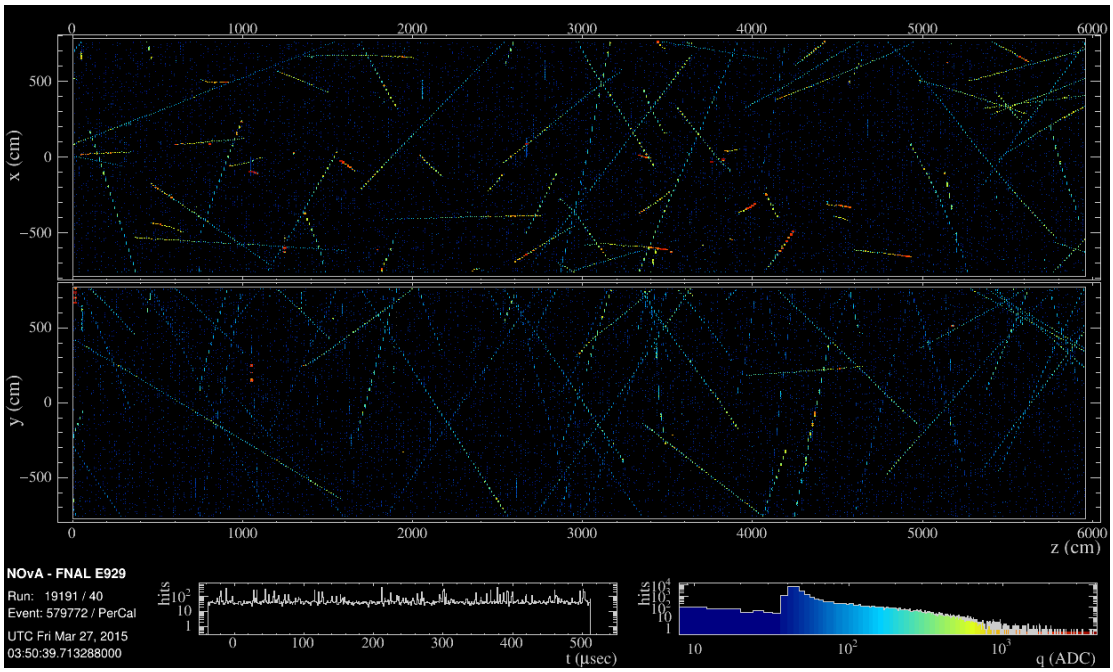

Figure 6.1. A NOvA event display showing a single cosmic ray event from March 27th, 2015. The event is 500 microseconds, and includes dozens of muon tracks. Cell hit views are shown for XZ (top) and YZ (bottom). The charge produced in each cell is shown by color.

Cosmic rates were calculated for each subrun by counting the total number of reconstructed cosmic tracks that passed the cut criteria per subrun and dividing by the total number of events within that subrun. Because the flux is dependent upon surface area, the Tracks/Events quotient is multiplied by a correction factor, $14/N_{diblocks}$, to correct for detector configurations in which not all 14 diblocks are active. Detector configurations are changed only from run to run, so all subruns within a run will have the same number of active diblocks. Because a run with fewer than 14 active diblocks will have less active detector volume, this correction factor accounts for missing volume by

assuming the cosmic muon density in the missing volume will be equal to the muon density in the rest of the detector, an assumption that is valid for the uniform cosmic flux at ground level.

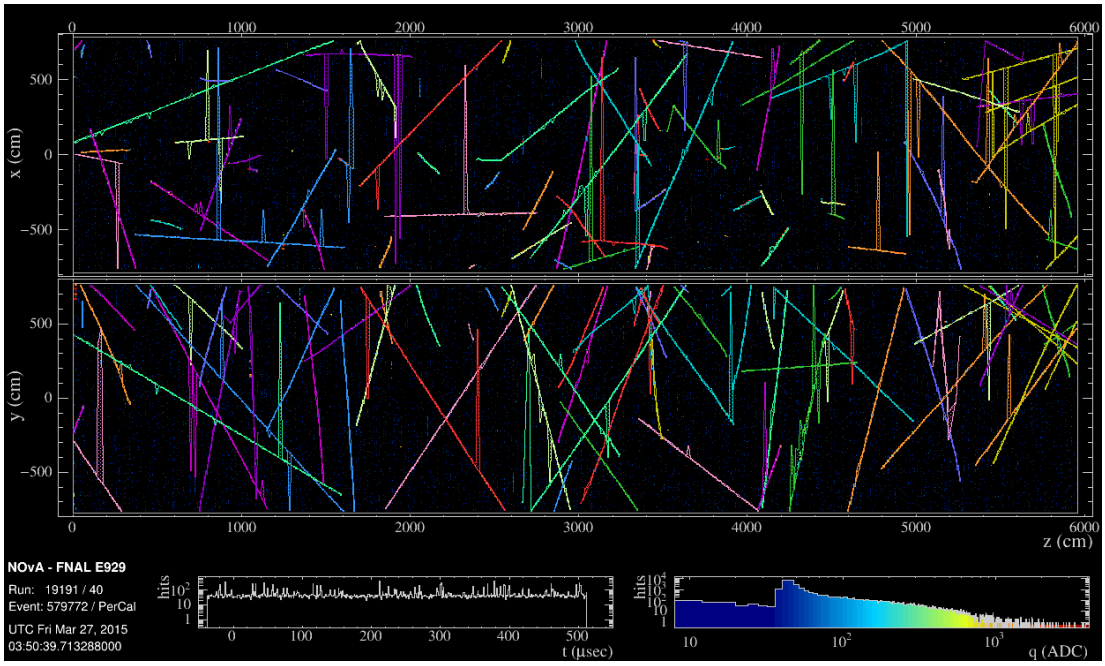

Figure 6.2. The event display of the same event shown in Figure 6.1, with hits traced by the Slicer, grouped together by time and space. The cosmic tracker uses these slices as input and separates any hits that do not fit close enough to a straight line drawn through beginning and endpoints.

$$CosmicRate_{subrun} = \frac{N_{tracks\ in\ subrun}}{N_{events\ in\ subrun}} \times \frac{14}{N_{active\ diblocks}} \quad (6.2)$$

The cosmic rate is given as Tracks / Events / FD Surface area, or Tracks/500 microseconds/900m^2. The surface area of the fully active, 14 diblock detector is 900 m^2. Subruns are not uniform in length (sometimes as short as 3 minutes, sometimes as long as 11 minutes), nor do they always contain the same number of events. But events *are* uniform in length, 500 microseconds in duration, so dividing the number of tracks by the

number of events is the most robust way of finding the average cosmic rate over a long period. The quotient gives the average number of muon tracks seen per event, a quantity easy to compare from subrun to subrun, and is unaffected by cutting a subrun short, or by runs in which not all subruns were processed.

The latter characteristic is important because a typical run of 64 subruns will always see a few failed processes once the files are processed by the grid. Of the 64 subruns in a run, it is normal for only about 50-60 subruns to finish processing without ambiguous errors that cause them to fail and become unusable for analysis. This many missing subruns can create a gap of up to over 2 hours where it would wrongly appear that no cosmic activity has occurred. If instead the calculation were of the number of tracks per minute or hour, or some unit of time independent of subrun, incongruities would arise in cases where a subrun fails reconstruction or another stage of processing, or a subrun is cut short by some user action, and a segment of time may appear to have no cosmic activity when in reality it has plenty. Averaging the tracks per event within the subrun removes any miscalculation risk associated with short or missing subruns. The weakness in this approach, however, is that a histogram binned by subrun may appear to give an inaccurate picture of the cosmic activity over a long duration, due to length non-uniformity, and situations in which entire runs were skipped during data-taking may create gaps in the data that appear to be longer or shorter than they are, or where in fact no gap exists in time.

A histogram of cosmic rates plotted as Tracks / Events / FD surface area vs. subrun are given in Figure 6.3. Gaps indicate subruns that failed reconstruction and analysis, or runs that were skipped in data taking. Missing runs do not necessarily indicate as much missing time as the scale would suggest, since the bins represent subruns and not times, which are not uniform in length. Other than failed subruns and nonexistent runs, no data was left out of the analysis. In Figure 6.3 the rate drops of interest are numbered in red. The total cosmic flux profile for March includes 9370 subruns, and 19.3 million events.

There was a quick drop in cosmic rates early in the month (1), lasting approximately a day before returning to a somewhat steady rate. This short duration made

it a bad FE candidate, as FEs are characterized in part by a recovery rate of 3 – 10 days [58], far more gradual than the recovery of this decrease. The quick return to previous rates suggests other causes. The cosmic rates remained steady for approximately 6 days with small variations before a large decrease appeared (2), on March 10^{th}-11^{th}. This decrease seemed to exhibit the same shape and behavior as a Forbush decrease, with the slow return to a steady rate over a period of days. A week later, before rates returned to normal, a second large decrease appeared (3), also with characteristic Forbush decrease behavior, with slowly increasing flux over the following days. The fourth decrease could be a remnant of a previous CME encounter, or a separate CME encounter in which only the CME's shock was incident upon Earth, (see Figure 3.6).

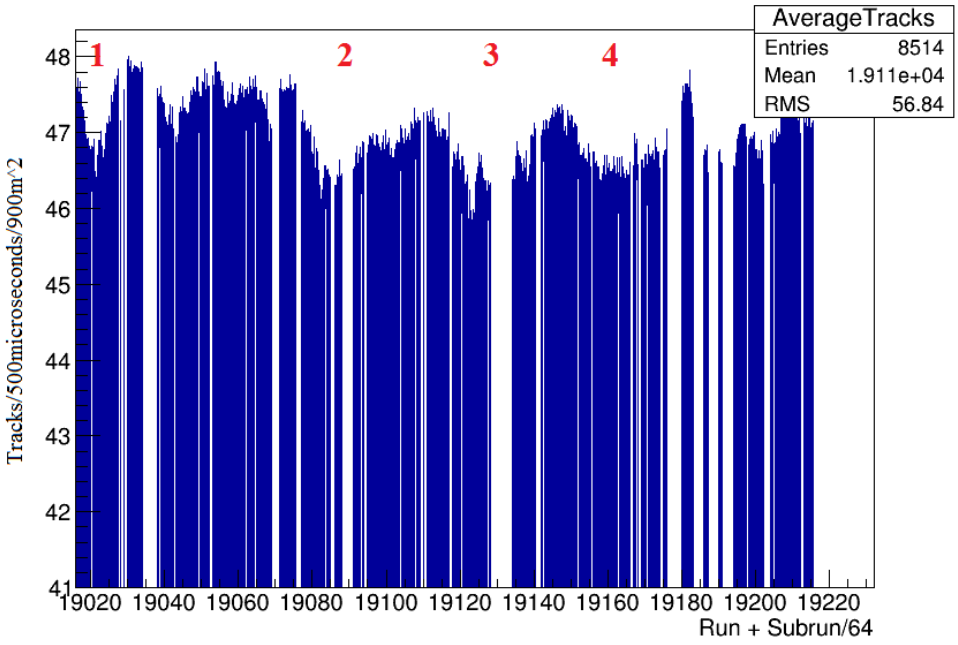

Figure 6.3. Cosmic muon flux in the Far Detector, reconstructed Tracks per Event per FD surface area, or tracks/500μs/900m^2. Activity is binned by subrun instead of time. Red numbers indicate areas of cosmic rate drops to be investigated in connection with solar activity. Data is not normalized or corrected for any other known effects.

Each observed decrease could be due to factors that are not necessarily extraterrestrial activity. These factors need to be evaluated first so corrections may be applied. Air pressure and air temperature are known to affect cosmic ray flux at Earth, and the degree to which these factors play a role varies from location to location, and from detector to detector. Latitude, altitude, and depth of the detectors will cause each to see different changes depending on temperature and air pressure, so the coefficients determining the magnitude of these effects need to be evaluated on a case by case basis. Increases in temperature cause an expansion of the atmosphere so that muons are produced at higher altitudes and have a larger probability of decaying before being detected. There is also a possible increase in muon flux that can be caused by increased temperature, since raised temperatures lead to air density decreases, in which meson interaction probabilities are lowered. This means more mesons decay, leading to more muons. However, the latter effect is more pronounced for underground detectors, while the former is dominant in surface detectors, like the Far Detector, which is expected to lead to a negative correlation between air temperature and muon rates.

The relationship between air pressure and cosmic ray intensity is

$$\left(\frac{\Delta I}{I}\right)_P = \beta\, \Delta P \tag{6.3}$$

where ΔI is the change in cosmic ray intensity, β is the barometric coefficient, and ΔP is the change in atmospheric pressure [83]. The barometric coefficient is determined by the relationship between detector counting rates N and air pressure P, given by

$$-\beta = \frac{lnN - lnN_o}{(P - P_0)} \tag{6.4}$$

where N is the detector counting rate at pressure P, and N_0 is the detector counting rate at pressure P_0.

The temperature variation has the same relation, given by

$$\left(\frac{\Delta I}{I}\right)_T = K\, \Delta T \tag{6.5}$$

with K the ground temperature coefficient, and ΔT the change in temperature. The value K is determined similarly to the barometric coefficient,

$$-K = \frac{lnN - lnN_o}{(T - T_0)}$$

(6.6)

The total effect of air pressure and temperature on cosmic flux is

$$\left(\frac{\Delta I}{I}\right) = \left(\frac{\Delta I}{I}\right)_P + \left(\frac{\Delta I}{I}\right)_T$$

(6.7)

The coefficients K and β were evaluated by analyzing segments of the data in which no significant decreases (<1%) were observed, to insure data unaffected by other factors, and comparing air temperature and air pressure to measure the contributions of each. If the cosmic rates fluctuate without a discernible dependence upon P or T, the decreases may instead be attributed to other sources.

Data spanning March 4^{th} – 8^{th} showed relatively steady cosmic rates, with less than 1% variation. This steadiness implied an absence of measurable extraterrestrial effects on cosmic intensity, which was confirmed against solar activity data [84]. These dates were used to study temperature and pressure effects on cosmic rates at the Far Detector, as well as the variation in daytime and nighttime cosmic rates. Cosmic rates were examined periodically through each day with corresponding air pressure and temperature fluctuations. Periods of identical temperature and fluctuating air pressure were compared to determine the barometric coefficient (when the second term in Equation 6.7 is 0), and periods of identical air pressure and fluctuating temperature were compared to determine the temperature coefficient (when the first term in Equation 6.7 is 0).

The barometric coefficient was found to be β = 0.00035 ± 0.00025. The temperature coefficient was found to be K = 0.00029 ± 0.00011. To establish whether or not temperature and pressure effects could explain the decreases numbered in Figure 6.3, the expected cosmic flux variation was calculated for each decrease, using data from March 7^{th} as a reference point, with a temperature of -4°C, an air pressure of 1016.93 mb,

and a cosmic muon rate of 47.38 tracks per event per 900 m^2. Air pressure and temperature modulation of the cosmic flux are tabulated in Table 6.1.

Air pressure and temperature effects were found not to account for the observed decreases. In three of the four cases, temperature and air pressure effects would instead have resulted in slight increases in cosmic rates, not decreases. For the decrease in which temperature and air pressure contributed to decreased cosmic rates, less than 1% of the decrease is explained by temperature and pressure. The cosmic rate fluctuation from day to night was also studied during this calm period, with data from 10 am – 2 pm compared with data from 10 pm – 2 am over four days. 163 subruns were used to establish the daytime rate, 285 subruns were used to establish the nighttime rate. The difference between day rates and night rates shows only a 0.48% decrease from day to night, indicating a steady cosmic flux when conditions are normal. See Figures 6.4 and 6.5. Stratospheric temperatures can also affect muon rates at Earth, but most studies for these effects show a relationship for high energy muons, in the TeV range. The effects are gradual, causing rate changes noticeable over a period of days and weeks. The Forbush effect is immediate, occurring over a period of hours, with rapid changes, and so stratospheric effects are considered negligible for this analysis.

Although a quantitative relationship between most characteristics of Forbush decreases is incomplete, the recovery rate of a Forbush effect can be described approximately by

$$I_0 - I = I_0 \times M \times exp((-t_0 - t)/\tau) \tag{6.8}$$

where I_0 is the cosmic ray intensity at the point of greatest decrease, directly before recovery begins at time t_0, I is the measured cosmic ray intensity at time t, M is the magnitude of the rate decrease, and τ is the recovery coefficient. According to this relationship and the estimated recovery periods for a number of Forbush decreases with similar magnitudes, the three observed periods of significant decrease should have the following recovery periods.

Decrease 1 should have a recovery period of approximately 113 hours, but its observed recovery rate is approximately 20 hours, exhibiting a symmetric onset and

recovery time, making it a bad candidate for a Forbush decrease. Decrease 2 should have a recovery period of approximately 154 hours, and has an observed recovery of greater than 120 hours. Its full recovery is not observed, as the third decrease begins before it can be completed. Decrease 3 should have a recovery period of approximately 180 hours, and its observed recovery is about 200 hours. The second and third decreases therefore appear to be good candidates for Forbush decreases.

The decrease on March 2nd does not exhibit the characteristics of a Forbush decrease or any other known interplanetary effect. The decreases later in the month have the characteristics of a Forbush decrease, and are unexplained by normal variations or any known Earth-sourced effects. The fourth observed decrease is unlikely to be the onset of a new Forbush decrease, instead explained as a continuation of the previous decreases. These results are discussed in the next section.

Table 6.1. The expected change in cosmic flux due to temperature and air pressure in Ash River, MN was calculated for the data corresponding to the 4 decreases. Temperature and pressure effects were compared to the observed change in flux. Three of the four decreases occurred during periods in which temperature and pressure effects alone would have instead caused an increase in flux (column 6). None of the observed decreases can be explained by air pressure and air temperature fluctuations.

Date	Cosmic Rate (tracks/event/FD area)	Temperature (C)	Air Pressure (mb)	Total observed % rate change	% rate change due to T,P
3/2	46.54	-5	1024.04	-1.77	$+0.25 \pm 0.18$
3/10	46.11	7	1007.11	-2.68	-0.025 ± 0.27
3/17	45.62	2	1027.09	-3.71	$+0.53 \pm 0.26$
3/22	46.22	-4	1028.10	-2.45	$+0.39 \pm 0.28$

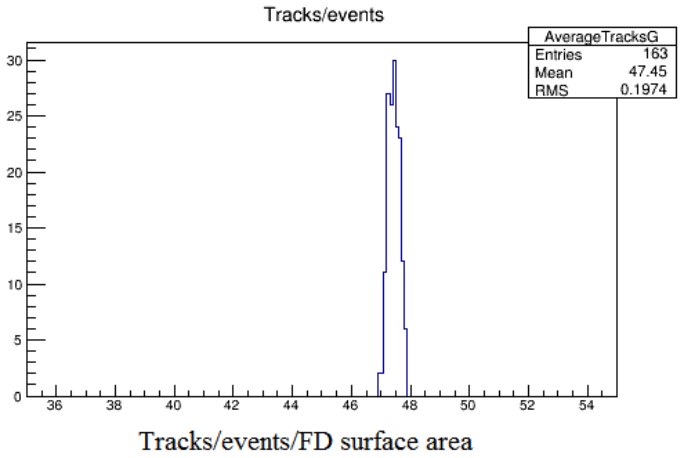

Figure 6.4. Cosmic rates during the 10 am - 2 pm period for 4 days, with an average rate of 47.45 tracks/event/detector area, and σ = 0.1974.

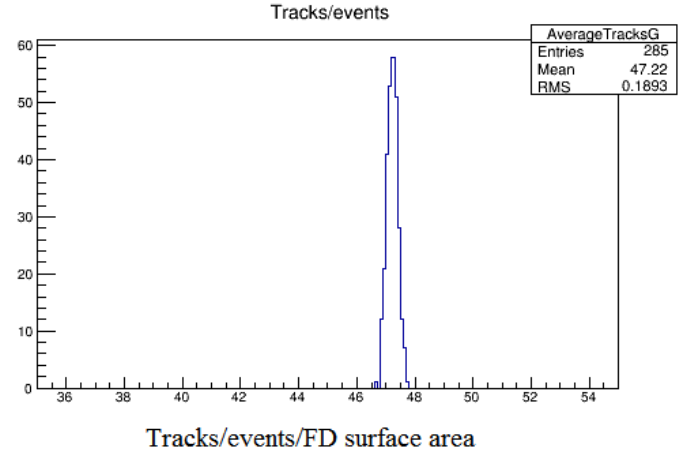

Figure 6.5. Cosmic rates during the 10 pm - 2 am period for 4 days, with an average rate of 47.22 tracks/event/detector areaa, and σ = 0.1893.

6.5 Results

The data in this analysis spans March 1st – March 31st, 2015. The runs included are 19016 – 19232 from the Far Detector. Not including missing runs and subruns that failed reconstruction, we are left with 187 runs, 9370 subruns, and about 19.3 million

events for analysis, for a total of 2.7 hours of total detector livetime spread over March. Rates from March 3rd – March 10th constitute the regular cosmic rates unaffected by solar activity or other terrestrial and extraterrestrial sources, so this data was used to establish a "Pre-Decrease" average rate, with which the decrease rates were compared. The pre-decrease rate is shown in Figure 6.6. It was calculated from 2107 subruns, and 4,405,809 events.

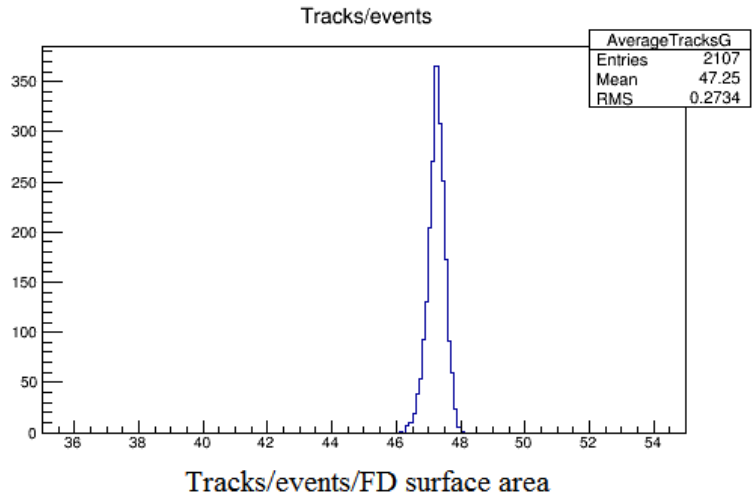

Figure 6.6. The pre-decrease distribution of the number of reconstructed tracks/500μs/900m^2. The average rate is 47.25 tracks, with σ = 0.2734.

The point of lowest intensity during the decrease compared with the pre-decrease average gives the magnitude of a Forbush effect. The cosmic rates for the first Forbush candidate are given in Figure 6.7, determined from 105,667 events. The decrease has a magnitude of 2.98%, with a standard deviation of 0.1565. The error associated with this measurement is 4.814×10^{-5}. This decrease occurred on March 11th, and recovered over the next six days until the second decrease appeared. The rates for this decrease are given in Figure 6.8, determined from 120,749 events. The decrease has a magnitude of 3.43%, with a standard deviation of 0.1678. The error associated with this measurement is 4.829×10^{-5}. The decrease occurred on March 17th, and its recovery time took the rest of

March. Solar data has been used to confirm that the identified decreases are due to solar activity.

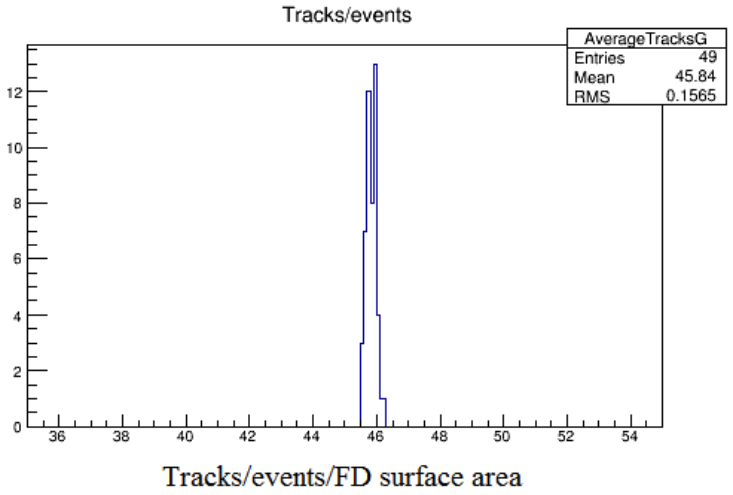

Figure 6.7. The distribution of cosmic rates at the point of maximum decrease for the first Forbush effect candidate, on March 11th. The rate was an average of 45.84 reconstructed tracks/event/detector area, and σ = 0.1565. The change in cosmic flux is a 2.98% decrease from the average cosmic flux, peaking at 16:50 on March 11th.

As discussed in Chapter 3, a Forbush decrease is caused by a full halo CME, i.e., a coronal ejection facing Earth. The solar wind speed at the time of the CME determines when the CME will arrive at Earth. The average solar wind speed is approximately 400km/s. Forbush decreases usually occur 2-3 days after the appearance of a CME. Solar data for this thesis was retrieved from SolarMonitor.org, managed by the Solar Physics Group at Trinity College, Dublin, provided by the NOAA Space Weather Prediction Center and the SDO/HMI and SDO/AIA consortia, and from the solen.info Solar Terrestrial Activity Report, which accumulates data from LASCO (the Large Angle and Spectrometric Coronagraph Experiment) and SOHO (the Solar and Heliospheric Observatory). Early March was devoid of solar activity until late March 7th and early March 8th. LASCO observed a fast partial halo associated with an M9 solar flare event in the AR12297 region on the sun. Figure 6.9 shows the X-ray flux profile, with a sharp,

fast burst during the night of the 7th – 8th. Solar wind speed at this time was ~550km/s, giving the CME an arrival time of early March 11th, coinciding perfectly with the decrease in NOvA's cosmic data.

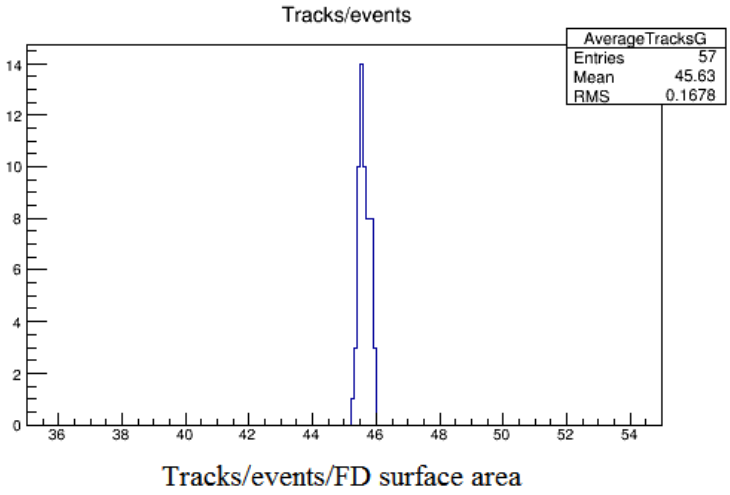

Figure 6.8. The distribution of cosmic rates at the point of maximum decrease for the first Forbush effect candidate, on March 17th. The rates were an average of 45.63 reconstructed tracks/event/detector area, and σ = 0.1678. The change in cosmic flux is a 3.43% decrease from the average cosmic flux.

A full-halo CME occurred on March 15th, associated with a C9.1 solar flare from the AR12297 region on the sun (Figure 6.10). The CME arrived at Earth in the early morning of March 17th, again coinciding with NOvA cosmic data. The x-ray flux and proton flux profiles are shown in Figures 6.11 and 6.12, respectively, showing extended bursts of x-ray activity and a large increase in proton flux.

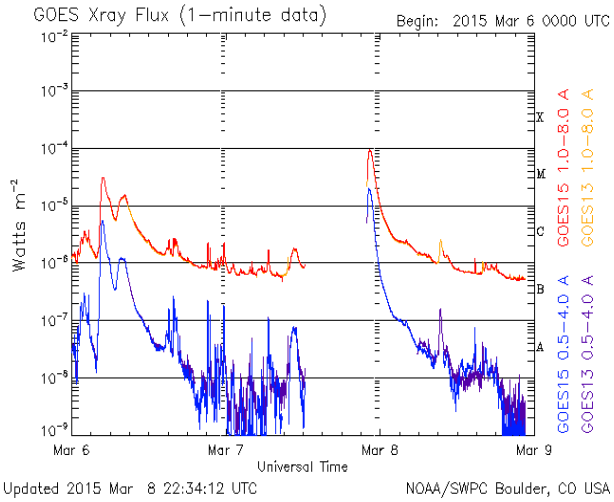

Figure 6.9. X-ray flux profile for the March 7th-8th partial-halo CME. Much of the data is missing, but the peak at the end of March 7th is visible, as well as its trail into March 8th. [85]

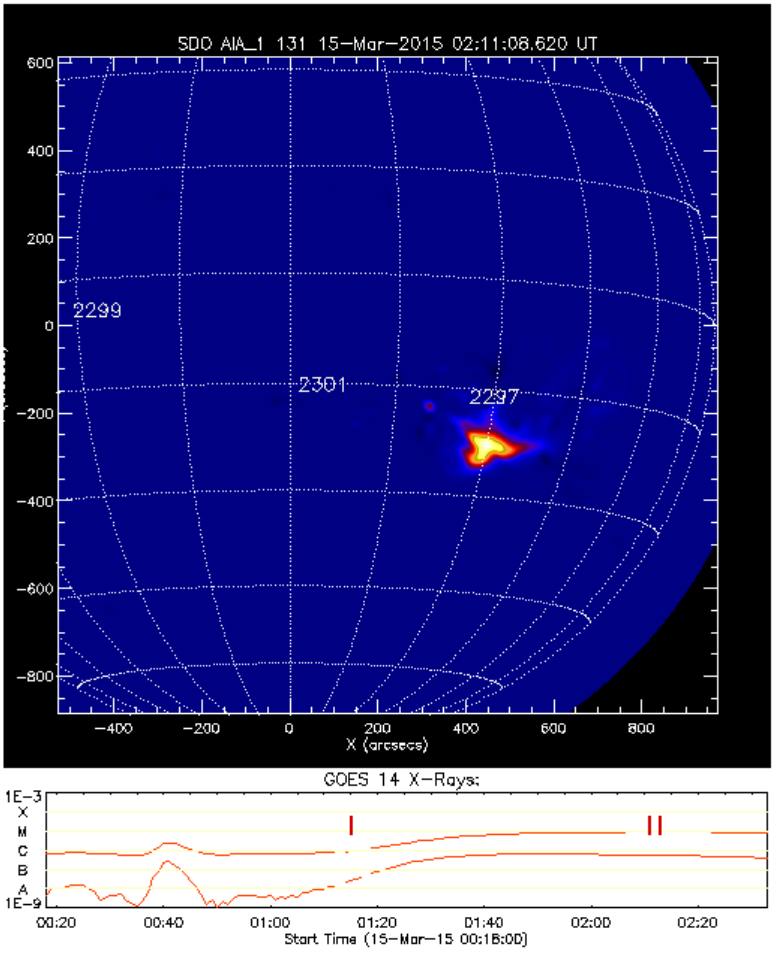

Figure 6.10. A C9.1 magnitude solar flare erupts from the sun in region 2297, the source of the CME associated with the March 17th geomagnetic storm on Earth. This image was taken from NASA's Solar Dynamics Observatory. The plot on the bottom shows the magnitude of X-ray flux, designated by flare class. Flare class is a measure of watts/square meter, with A < 10^{-7}, B = 10^{-7} – 10^{-6}, C = 10^{-6} – 10^{-5}, M = 10^{-5} – 10^{-4}, and X = 10^{-4} – 10^{-3}. [84]

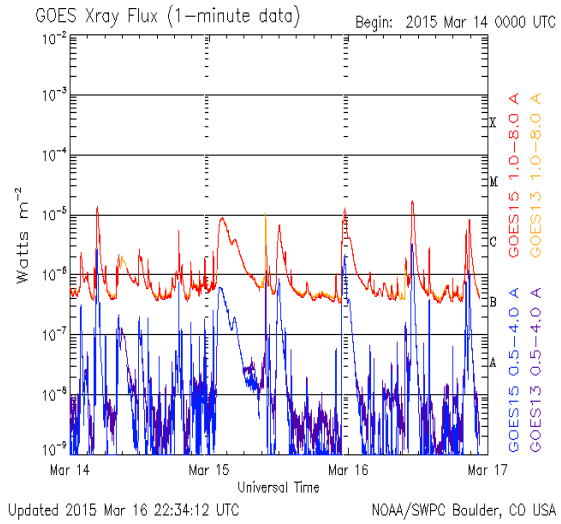

Figure 6.11. X-ray flux profile as measured by the GOES spacecraft. The March 15th CME can be seen as the wide curve, peaking early in the morning. [85]

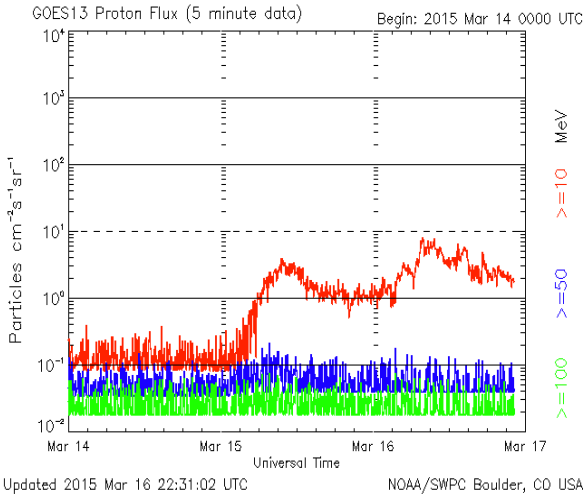

Figure 6.12. Proton flux associated with the March 15th CME, taken from the GOES spacecraft. [85]

The observed decreases of 2.98% on March 11th and 3.43% on March 17th are consistent with the arrival of CMEs generated on March 8th and March 15th. The second CME's arrival at Earth was notable for causing a G2 geomagnetic storm (visible at 54.2° latitude and higher), the strongest geomagnetic storm of the year to date. In Chapter 3 the differences between Forbush decreases observed in neutron and muon data were mentioned. Neutron monitors are the most common detectors used for observing the Forbush decrease, and due to the lower energy of their parent cosmic particles, will exhibit a larger decrease than what is seen in muon detectors, typically three times the magnitude. NOνA's data was compared to that of two neutron monitors, the Oulu Neutron Monitor in Finland, and the Moscow Neutron Monitor in Russia, to check the veracity of these findings. Both monitors detected the March 17th decrease, with a magnitude of ~4.5%. This is greater than the magnitude observed in NOνA, but the NOνA data shows a larger decrease than 1/3 that in 0the neutron data. The decrease observed on March 11th does not appear clearly in the neutron data, though there is a small magnitude decrease in cosmic flux from March 11th – 12th of about 1-2%, but not to the extent that NOνA sees it. Many characteristics in the cosmic ray profiles shared between both neutron monitors are also found in the NOνA data, as shown in Figure 6.13.

The tight distribution of cosmic events in both decreases and the large sample sizes put both CME-influenced cosmic intensity decreases within a confidence interval of ± 0 at the 99.9% confidence level. The measurement of the March 17th Forbush decrease is confirmed by data from two neutron monitors. Most data on Forbush effects exist in the form of neutron data. The analysis of this thesis provides additional data on solar modulation of muon cosmic ray intensity at Earth, which is comparatively lacking in the overall study of Forbush decreases. Theoretical modeling of the Forbush effect is still incomplete, and detailed data is important for furthering this work. The long term study of Forbush decreases enables a stronger understanding of the effects of solar activity on Earth's magnetic field, with data on muon cosmic rays complementing that of neutron cosmic rays for a more complete picture.

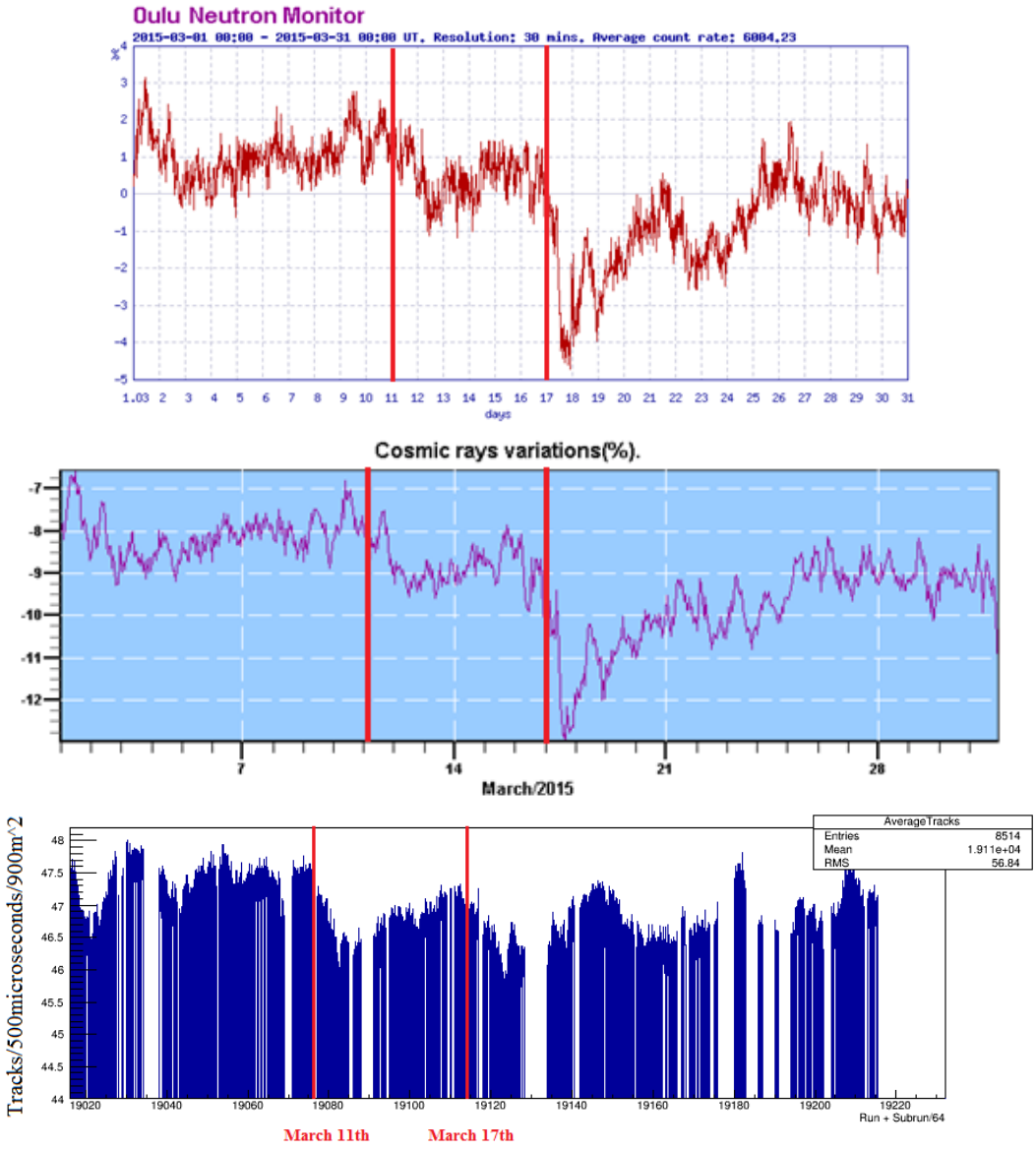

Figure 6.13. Data from the Oulu (top) and Moscow (middle) neutron monitors, plotted as percentage deviation from the average cosmic rate vs. time. NOvA's cosmic data is plotted on the bottom. Red bars show the time of impact of CMEs on March 11th and March 17th. Both Forbush decreases are observed in the neutron and muon data. Oulu and Moscow neutron data taken from [86] and [87].

CHAPTER 7. CONCLUSIONS

The measurement of Cerenkov reemission in NOνA's liquid scintillator is found to cause up to a 15% excess of photon production over the UV spectrum that will contribute to a signal in NOνA's cells, with a non-linear ratio of the number of reemitted Cerenkov photons to the number of photons produced by scintillation alone. This value is close to the value estimated for Cerenkov reemission in KamLAND's liquid scintillator after fitting to the measured value of Birks' quenching coefficient, suggesting approximately a 15% contribution.

Birks' quenching constant has not been measured for NOνA's liquid scintillator, because the experiment intended to do so has not been finished. This value is required for a full correction to the energy calibration of NOνA's liquid scintillator. Once Birks' constant is determined, the reemission and quenching results will be implemented into a simulation to evaluate the total effect on the scintillator's energy response. However, even without a simulation the effects of these quantities can be calculated.

Measuring the solar modulation of cosmic flux at Earth revealed two Forbush decrease events in excess of 2% with greater than 10 sigma confidence, with recovery periods longer than 5 days. If, in fact, muons tend to exhibit only one third the decrease magnitude exhibited by neutrons, the data from the Far Detector shows a larger effect than expected from comparison to neutron data taken at the Moscow and Oulu neutron monitors. A possible explanation for the difference in magnitude is the directional cuts made for this analysis, because neutron monitors do not account for direction. Were one to look at muons from all angles, it is possible the overall decrease magnitude would be lesser than when cutting at 18 degrees, since a wider energy spectrum would be observed.

This study demonstrates NOνA's capability as a cosmic muon detector to be used for physics outside of neutrino oscillations, and provides useful data that serves as a comparison against neutron data. The quantitative modeling of FEs is incomplete, and more data sets, particularly from muon detectors, are necessary for progress toward this end.

LIST OF REFERENCES

[1] Fukuda, Y. et al. (1998). "Measurements of the Solar Neutrino Flux from Super-Kamiokande's First 300 Days". Physical Review Letters 81 (6): 1158–1162

[2] Scott, F.A. “Energy Spectrum of the Beta-Rays of Radium E” Phys. Rev. 48, 391. 1935

[3] Cowan, C. L., Jr.; Reines, F.; Harrison, F. B.; Kruse, H. W.; McGuire, A. D. “Detection of the Free Neutrino: A Confirmation” Science, 124, 3212, pp. 103-104. 1956

[4] Danby, G., Gaillard, J.M., Konstantin A. Goulianos, L.M. Lederman, Nari B. Mistry, M. Schwartz, J. Steinberger “Observation of High-Energy Neutrino Reactions and the Existence of Two Kinds of Neutrinos” Phys.Rev.Lett. 9 (1962) 36-44

[5] Perl, M.L. et al. DONUT collaboration "Evidence for Anomalous Lepton Production in e+e− Annihilation". Physical Review Letters 35 (22): 1489. 1975

[6] Davis, Raymond Jr., Harmer, Don S., Hoffman, Kenneth C. "Search for Neutrinos from the Sun". Physical Review Letters 20: 1205. 1968

[7] Nakamura, K., Petcov, S.T. “Particle Data Group – The Review of Particle Physics” Physics Letters B592. Chapter 13. “Neutrino Mass, Mixing, and Oscillations.” 2013 http://pdg.lbl.gov/2013/reviews/rpp2013-rev-neutrino-mixing.pdf

[8] The SNO Collaboration "Measurement of Charged Current Interactions Produced by 8B Solar Neutrinos at the Sudbury Neutrino Observatory" Phys. Rev. Lett. volume 87, 071301 (2001)

[9] KamLAND Collaboration “First Results from KamLAND: Evidence for Reactor Anti-Neutrino Disappearance” Phys.Rev.Lett.90:021802,2003

[10] Pontecorvo, B., "Mesonium and anti-mesonium". Zh. Eksp. Teor. Fiz. 33: 549–551. reproduced and translated in Sov. Phys. JETP 6: 429. 1957.

[11] Maki, Z. M. Nakagawa, and S. Sakata. "Remarks on the Unified Model of Elementary Particles". Progress of Theoretical Physics 28: 870 1962

[12] Pontecorvo, B. "Neutrino Experiments and the Problem of Conservation of Leptonic Charge". Zh. Eksp. Teor. Fiz. 53: 1717. reproduced and translated in Sov. Phys. JETP 26: 984. 1968.

[13] Schechter, J., and Valle, J.W.F., "Neutrino masses in SU(2) ⊗ U(1) theories" Phys. Rev. D 22, 2227. 1980

[14] S. Eidelman et al. (2004). "Particle Data Group - The Review of Particle Physics". Physics Letters B 592 . Chapter 15: Neutrino mass, mixing, and flavor change. Revised September 2005.

[15] Glashow, S.L. "Partial-symmetries of weak interactions". Nuclear Physics22 (4): 579–588. 1961

[16] Yang, Tingjiun. *A Study of Muon Neutrino to Electron Neutrino Oscillations in the MINOS Experiment* MINOS thesis 2009

[17] Xin, Xianhao. "Glashow-Weinberg-Salam Model: An Example of Electroweak Symmetry Breaking" 2007

[18] Mandl, F., and Shaw, G. *Quantum Field Theory* 2nd Edition. Wiley. 2010

[19] Kumar, K. et al; Jefferson Lab. "An Ultra-precise Measurement of the Weak Mixing Angle using Møller Scattering" PAC 34 Presentation. 2009

[20] Bega, Klejda. *Measurement of the Weak Mixing Angle in Møller Scattering.* SLAC thesis. 2004

[21] Forston, E.N., Lewis, L.L.. "Atomic Parity Nonconservation Experiments" Physics Reports (Review Section of Physics Letters) 113, No. 5 (1984) 289-344.

[22] Aseev, V.N. et al. "An upper limit on electron antineutrino mass from Troitsk experiment" Phys. Rev. D 84 (2011) 112003

[23] Betancourt, M. *Study of Quasi-Elastic Scattering in the NOvA Detector Prototype* NOvA thesis. 2013

[24] Griffiths, David. *Introduction to Elementary Particles*. 2nd Edition Wiley-VHC. 2008

[25] Formaggio, J.A., and Zeller, G.P. "From eV to EeV: Neutrino cross sections across energy scales" Reviews of Modern Physics 84. 2012

[26] Llewellyn Smith, C.H. "Neutrino Reactions at Accelerator Energies" Phys.Rept. 3 261-379. 1972

[27] V. Bernard, L. Elouadrhiri, and U. G. Meissner, Axial structure of the nucleon: Topical review, J. Phys. G 28, R1 (2002). http://iopscience.iop.org/0954-3899/28/1/201/pdf/0954-3899_28_1_201.pdf
[28] Zeller, G.P. "Particle Data Group – The Review of Particle Physics" Physics Letters B 592. Chapter 45 "Neutrino Cross Section Measurements". 2012
[29] Rein, D., Z. Phys. C 35 43 (1987). Rein, D.,
[30] Sehgal, L.M. Ann. Phys. (N.Y.) 133,79 (1981).
[31] Pleijel, H. Award Ceremony Speech, The Royal Swedish Academy of Sciences, Dec. 10th 1936.
http://www.nobelprize.org/nobel_prizes/physics/laureates/1936/press.html
[32] Beaty, J.J. "Particle Data Group – The Review of Particle Physics" Physics Letters B 592. Chapter 24 "Cosmic Rays". 2012 http://pdg.lbl.gov/2011/reviews/rpp2011-rev-cosmic-rays.pdf
[33] Mewaldt, R.A. "Cosmic Rays". Macmillan Encyclopedia of Physics. New York: Simon & Schuster Macmillan, 1996.
http://www.srl.caltech.edu/personnel/rmewaldt/cos_encyc.html
[34] Sekido, Y., Masuda, T., Yoshida, S., and Wada, M. "The Crab Nebula as an Observed Point Source of Cosmic Rays" Phys. Rev. 83, 658 – 1 August 1951
http://journals.aps.org/pr/abstract/10.1103/PhysRev.83.658.2
[35] Aharonian, F., et al., "Discovery of very-high-energy rays from the Galactic Centre ridge," Nature. 439: 695-698. 2006.
[36] Ackermann, M. et al. "Detection of the Characteristic Pion-Decay Signature in Supernova Remnants" Science 339, 6121. 807-811. 15 Feb 2013
http://www.sciencemag.org/content/339/6121/807.full
[37] Bustamante, M. et al. "High-Energy Cosmic-Ray Acceleration"
https://cdsweb.cern.ch/record/1249755/files/p533.pdf
[38] Fermi, E. "On the Origin of the Cosmic Radiation" Physical Review 75, Volume 8. 1169-1174. 15 April 1949. http://journals.aps.org/pr/pdf/10.1103/PhysRev.75.1169
[39] Zentrum für Astronomie und Astrophysik. "Origin and Propagation of Cosmic Rays" http://www-astro.physik.tu-berlin.de/node/274

[40] Boezio, M. et al., Astropart. Phys. 19, 583 (2003).
[41] AMS Collaboration, Phys. Lett. B490, 27 (2000); Phys. Lett. B494, 193 (2000).
[42] Svensmark, H. "Influence of Cosmic Rays on Earth's Climate". *Physical Review Letters* 81 (22):5027–5030. Bibcode:1998 PhRvL..81.5027S.doi:10.1103/PhysRevLett.81.5027 http://journals.aps.org/prl/pdf/10.1103/PhysRevLett.81.5027
[43] Bellotti, R., et al., Phys. Rev. D53, 35 (1996).
[44] Bellotti, R., et al., Phys. Rev. D60, 052002 (1999).
[45] Boezio, M., et al., Phys. Rev. D62, 032007 (2000);
[46] Boezio, M., et al., Phys. Rev. D67, 072003 (2003). February 16, 2012 14:07 24.
[47] Coutu, S., et al., Phys. Rev. D62, 032001 (2000). 36. S. Haino et al.. Phys. Lett. B594, 35 (2004).
[48] De Pascale, M.P. et al., J. Geophys. Res. 98, 3501 (1993)
[49] Grieder, P.K.F. Cosmic Rays at Earth, Elsevier Science (2001)
[50] Rastin, B.C. J. Phys. G10, 1609 (1984)
[51] Ayre, C.A. et al., J. Phys. G1, 584 (1975)
[52] Kremer J. et al., Phys. Rev. Lett. 83, 4241 (1999)
[53] Haino S. et al. (BESS Collaboration), Phys. Lett. B594, 35 (2004)
[54] Jokisch, H. et al., Phys. Rev. D19, 1368 (1979)
[55] Greisen, K. Ann. Rev. Nucl. Sci. 10, 63 (1960)
[56] Lockwood, J. "Forbush Decreases in the Cosmic Radiation" Space Science Reviews 12, 658-715 (1971)
[57] Belov, A.V. "Forbush Effects and their Connection with Solar, interplanetary, and geomagnetic phenomena". Universal Heliophysical Processes Proceedings IAU Symposium No. 257, 2008 N. Gopalswamy & D.F. Webb, eds.
[58] Cane, H. "Coronal Mass Ejections and Forbush Decreases" Space Science Reviews 93, 55-77 (2000)
[59] Lee, S., Oh, S., Yi, Y. "Simultaneity of Forbush decrease events observed at middle-latitude neutron monitors" Journal of Geophysical Research. Space Physics. 118, 2. 608-614. Feb 2013.

[60] Barbashina, N.S. “Study of Forbush Effects by Means of Muon Hodoscopes.” Proceeding of 20th ECRS, Lisbon, 2006. arXiv:astro-ph/0701288

[61] Messier, M. “The NOvA Experiment” NOvA-Doc-6226 2011

[62] *NUmI Off Axis nu—e Experiment – Technical Design Report*

[63] Reider, H. Photographer

[64] Kephart, K.M. “NOvA Near Detector Liquid Scintillator Filling Experience” NOvA-Doc-5882. 2011

[65] Slotman, M. and Chase, T. “Documentation of Cracks on the Inside of NOvA Manifold Covers”NOvA-Doc-5164. 2010

[66] Mualem, L. “NOvA APD mounting and Electronic Box Proposed Changes per Installation Meeting Fermilab 7-26&27, 2011” NOvA-doc-6346. 2011

[67] Hatcher, Robert. “NOvA Simulation Chain” NOvA-doc-6941. 2012

[68] Sala. P.R., Vanini, S. “FLUGG: FLUKA + Geant4 Geometry for Simulation in HEP“ 2003, Aug 2014. < http://www.fluka.org/content/tools/flugg/>

[69] Ferrari, A., Sala, P.R., Fasso`, A., and Ranft, J. "FLUKA: a multi-particle transport code" CERN-2005-10 (2005), INFN/TC_05/11, SLAC-R-773

[70] GENIE Group “The GENIE Neutrino Monte Carlo Generator” Nucl.Instrum.Meth. A614 (2010) 87-104

[71] “pkgs/PhotonTransport (NOvA Offline)” https://cdcvs.fnal.gov/redmine/projects/novaart/wiki/PkgsPhotonTransport Aug. 2014

[72] “pkgs/ReadoutSim (NOvA Offline)” https://cdcvs.fnal.gov/redmine/projects/novaart/wiki/PkgsReadoutSim Aug. 2014

[73] Mason, Philip. NOvA-doc-8569. 2013

[74] Kutsche, R., Paterno, M. Wang, M. “Intensity Frontier Common Offline Documentation: art Workbook and Users Guide”. Alpha-release 0.90 2 August 2015. https://web.fnal.gov/project/ArtDoc/Shared%20Documents/art-documentation.pdf

[75] Gole, J. https://www.physics.gatech.edu/user/james-gole

[76] Berlman, I. Handbook of Fluorescence Spectra of Aromatic Molecules, 2nd edition. 1971

[77] Flumerfelt, E. “DAQ Software Contributions, Absolute Scale Energy Calibration and Background Evaluation for the NOvA Experiment at Fermilab”. Thesis. 2015. UT_HEP-doc-103-v10
[78] S. Mufson et al., Liquid scintillator production for the NOvA experiment. Nuclear Instruments and Methods in Physics Research A 799 (2015) 1–9 2015
[79] Heller, J.M. et.al., The Journal of Chemical Physics, vol 62, no 10, May 1975, page 4121-4124
[79] Ch. Wohlfarth, B. Wohlfarth; M. D. Lechner; SpringerMaterials; sm_lbs_978-3-540-48434-9_7 (Springer-Verlag GmbH, Heidelberg, 1996), http://materials.springer.com/lb/docs/sm_lbs_978-3-540-48434-9_7; accessed: 11-05-2015, 12:58:00 GMT-0400
[80] Subvolume B ‘Refractive Indices of Organic Liquids’ of Volume 38 ‘Optical Constants’ of Landolt-Börnstein - Group III Condensed Matter.
[81] Lide, D. Handbook of Chemistry and Physics 82nd Edition. 2001
[82] Submitting NOvA ART Jobs, from the NOvA Wiki. https://cdcvs.fnal.gov/redmine/projects/novaart/wiki/Submitting_NOvA_ART_Jobs
[83] De Mendonca, R.R.S, et al. “Analysis of atmospheric pressure and temperature effects on cosmic ray measurements”. Journal of Geophysical Research, Space Physics Volume 118 (2013) 1403-1409
[84] Data found at SolarMonitor.org, by the Solar Physics Group at Trinity College Dublin. SDO data provided courtesy of the SDO/HMI and SDO/AIA consortia.
[85] Data found at SolarMonitor.org, by the Solar Physics Group at Trinity College Dublin. GOES data provided by the NOAA Space Weather Prediction Center.
[86] Data taken from the Cosmic Ray Station of the University of Oulu, at the Sodankyla Geophysical Observatory. Cosmicrays.oulu.fi. 2015
[87] Data taken from the Moscow Neutron Monitor. http://cr0.izmiran.rssi.ru/mosc/main.htm. 2015.

VITA

Philip Mason was born in Evansville, Indiana in 1984. He received his B.S. in Physics from Middle Tennessee State University, with a thesis entitled “The Effects of the Galilean Moons on the Jovian Radio Emissions”, detailing an analysis of data from the Cassini spacecraft’s Radio and Plasma Wave Science Instrument to look for radio wave enhancement at Jupiter caused by interactions between its moons and magnetic field. As a graduate student, he worked on the NOνA experiment at Fermilab for five and a half years, contributing to the construction of the prototype detector and various other commissioning, production, monitoring, and analysis tasks. He received his Ph.D in Physics from the University of Tennessee, Knoxville in 2015.